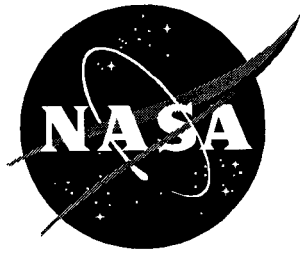


Bistatic k -Space Imaging for Electromagnetic Prediction Codes for Scattering and Antennas

John F. Shaeffer, Kam W. Hom, R. Craig Baucke, Brett A. Cooper, and Noel A. Talcott, Jr.



Bistatic k -Space Imaging for Electromagnetic Prediction Codes for Scattering and Antennas

John F. Shaeffer

Marietta Scientific, Inc. • Marietta, Georgia

Kam W. Hom

Langley Research Center • Hampton, Virginia

R. Craig Baucke

General Electric Aircraft Engine Business Group • Cincinnati, Ohio

Brett A. Cooper

Marietta Scientific, Inc. • Marietta, Georgia

Noel A. Talcott, Jr.

Langley Research Center • Hampton, Virginia

Available electronically at the following URL address: <http://techreports.larc.nasa.gov/ltrs/ltrs.html>

Printed copies available from the following:

NASA Center for AeroSpace Information
800 Elkridge Landing Road
Linthicum Heights, MD 21090-2934
(301) 621-0390

National Technical Information Service (NTIS)
5285 Port Royal Road
Springfield, VA 22161-2171
(703) 487-4650

Contents

Summary.....	1
Introduction	1
Symbols	3
Theory.....	4
Excitation	4
Computing Images in k Space.....	4
Generalized Radiation Integral	5
Image Resolution.....	5
Selection of Image Resolution	6
k -Space Computational Points	7
Fourier Transform Issues	7
Image Center of Rotation	7
Discussion	7
Implementation and Example Results	8
Method-of-Moments Computer Code Implementation.....	8
Patch Method-of-Moments Computer Code Example Results.....	8
Square plate	8
NASA almond	9
Airplane configuration.....	10
Body-of-Revolution MOM Computer Code Implementation.....	10
Body-of-Revolution Image Examples.....	11
Sphere	11
Airplane configuration BOR-PATCH model	11
Physical Optics Computer Code Implementation.....	11
Physical Optics Image Examples	12
NASA almond	12
Airplane configuration.....	12
Finite Element Frequency Domain Computer Code Implementation.....	13
Finite Element Frequency Domain Image Examples	13
MOM Computer Code Implementation of 5λ -Long End-Fed Antenna	13
Three-Dimensional Image Implementation Examples	14
Three-dimensional image for point targets	14
Three-dimensional image for parallel square plates	14
Three-dimensional image for sphere	15
Three-dimensional image for an airplane	15
Comparison of Analytical and Experimental Images.....	15
Experimental Theory.....	15
Bandwidth and Resolution	16
Experimental and Bistatic k -Space Images.....	17

Experimental parameters	17
Computational parameters	17
Image comparisons	17
Summary Remarks	18
Appendix—Image Issues	20
References	24
Table	25
Figures	26

Summary

A bistatic k -space image concept for frequency domain (FD) electromagnetic (EM) computer codes is presented. The concept enables images to be computed without the frequency sweep required for experimental images, which results in a significant reduction in computational effort. This analytical image technique uses bistatic radiation computed from a generalized radiation integral.

Images permit physical insight and understanding into how a radiation or scattering pattern is produced by decomposition of the resultant radiation into contributions from localized scattering centers or *hot spots*. Knowledge of these hot spots permits a user to understand and modify the structure to obtain desired features.

The costs associated with computation of bistatic images are usually small compared with the effort required to obtain the current distribution. Bistatic k -space fields are computed from the currents by the generalized radiation integral. This is similar to the effort required to compute a bistatic radiation pattern. The computed k -space $E(\mathbf{k})$ fields are then Fourier transformed to obtain the spatial image.

The bistatic k -space technique can be applied to both antenna and scattering problems. It can be used with any frequency domain computer algorithm that produces a current distribution on the geometric structure. Images can be computed in one, two, or three dimensions, which typically correspond to downrange, downrange–cross-range, and volumetric images, respectively.

Bistatic scattering images are shown for a variety of target geometries computed by FD EM prediction algorithms that include method-of-moments–patch (MOM-patch), body-of-revolution (BOR), and BOR-patch computer codes; physical optics (PO) computer codes; and finite element frequency domain (FEFD) computer codes. High-level details are presented showing how to incorporate this image technique into each of these computer codes. Implementation is not difficult because most computer codes already have subroutines utilizing the normal radiation integral. The radiation subroutines need only be generalized to compute arbitrary points in k space rather than with $\mathbf{k}^{\text{radial}}$ as a function of angle.

The k -space scattered fields are computed on an orthogonal grid in k space corresponding to $(\mathbf{k}_{\text{down}}, \mathbf{k}_{\text{cross}}, \mathbf{k}_{\text{vol}})$. These are independent and, thus, eliminate image-smearing problems commonly associated with frequency-angle circular arc k -space inverse synthetic aperture radar (ISAR) experimental images.

Bistatic k -space images are not the same as those produced by the swept frequency experimental approach; however, they have many similarities. Comparisons between the two image approaches are discussed with specific examples shown.

Introduction

Electromagnetic diagnostic imaging at microwave frequencies for scattering bodies has been a great help in the physical understanding and design of these bodies. Imaging permits physical understanding of fundamental scattering mechanisms responsible for the overall scattered energy. Images provide this understanding by decomposition of the resultant scattered radiation into contributions from localized scattering centers or hot spots. With this information the user can modify the structure to obtain desired features such as a lower or higher radar cross section (RCS) or to synthesize a desired antenna pattern.

Experimental imaging is accomplished by illumination of the target with a bandwidth of frequencies, which emulates the frequency content of a short pulse. This same process could also be used analytically; however, in computer intensive solutions such as the method of moments where a new matrix would be required at each frequency, this image approach is seldom used. This report describes a bistatic k -space analytical imaging technique that uses a single frequency to obtain an image and results in efficient image computation in terms of computer resource time. This analytical bistatic-imaging technique can be applied to both antenna and scattering geometries in contrast to experimental imaging, which has principally been used for scattering applications.

Electromagnetic microwave imaging was first done experimentally for scattering applications. The work of Mensa in 1980 (ref. 1) popularized the technique. Within a decade, many other experimental ranges appeared with imaging capabilities; these included the far-field outdoor ranges and the indoor compact ranges, which utilized a reflector dish to illuminate targets with planar waves. The experimental image approach typically produces one-dimensional downrange and two-dimensional downrange–cross-range images.

Experimental downrange images are obtained by illumination of the target with nanosecond short pulses whose spatial extent is much less than the target dimensions. The reflected return is then naturally a function of downrange time delay (distance). Typically, short pulses are seldom used but are emulated by illumination of the target with an equivalent bandwidth of frequencies synthesizing a short pulse. Because time and frequency are a Fourier transform pair, the two approaches are

equivalent. By measurement of the reflected amplitude and phase over a bandwidth of frequencies, a Fourier transform can be used to obtain the time-delayed downrange image. The time-delayed amplitude data are then readily converted into downrange distance by a knowledge of the velocity of propagation. Typically the fast Fourier transform (FFT) is used to transform between the time domain (TD) and frequency domain (FD).

Experimental cross-range image information is obtained by rotation of the target over a small angular interval centered on the viewing angle by use of inverse synthetic aperture radar (ISAR) techniques. Because angle and cross-range are related to wave number k and spatial position r , which make the Fourier transform pair kr , the scattered radiation can then be Fourier transformed to obtain cross-range image information.

Images may also be computed from numerical solutions of Maxwell's equations. Two types of solution formulations exist: time domain and frequency domain.

Time domain solutions naturally produce a time-delayed scattered field because the illumination source is a short pulse. From this time solution, the frequency domain solution is obtained by a Fourier transform. Such computer codes have existed but, until recently, have never been accepted and used; most users are interested in the frequency domain solutions directly, e.g., a plot of scattered radiation versus angle.

Frequency domain computational solutions at single frequencies are more common because they produce an RCS or antenna scattering pattern directly without the need to perform a Fourier transform. These FD solutions can also be used to compute images similar to experimental images by recomputation of the solution for each frequency in a desired bandwidth, i.e., 16, 32, ..., 512, ... solutions. Usually this is such a time-consuming task that the approach is not considered because such algorithms that are based on the method of moments require a matrix fill, a lower and upper triangular matrix decomposition (LU), and a back solution for each frequency. Thus, while an image could in principle be obtained from FD algorithms, they seldom if ever are pursued, particularly for electrically large bodies where matrix sizes can easily exceed 10000 unknowns.

Analytically, bistatic images from FD algorithms that use only a single frequency of excitation have not been available until just recently. The bistatic k -space image technique permits an FD algorithm to produce an image in one, two, or three dimensions for one excitation frequency and at one excitation angle.

The utility of this technique is obvious. The bistatic imaging approach is computationally more efficient than the experimental imaging approach, which requires mul-

multiple frequencies and multiple angles in the imaging computations.

A bistatic image obtained with a single-current solution from a MOM computer code was first accomplished by Cooper in unpublished efforts (circa 1987). This approach involved the use of a far-field radiation integral to produce a downrange image. Latter efforts by Shaeffer to extend Cooper's image method to two dimensions without image focus-smear problems led to a theoretical bistatic k -space formulation for the approach. This theory was the foundation and rationale for the application of Cooper's approach. (See refs. 2 and 3.)

The bistatic k -space image approach uses a single computed current distribution with a generalized far-field radiation integral. The usual \mathbf{k}^{scat} vector in the radiation integral is generalized to \mathbf{k}_{down} , $\mathbf{k}_{\text{cross}}$, and \mathbf{k}_{vol} . The Fourier transform of this computed scattered field in k space is then transformed into an image from the transform pair $\mathbf{k} \cdot \mathbf{r}$ where \mathbf{k} is the wave vector and \mathbf{r} is the spatial position.

The images derived by the bistatic computational approach are not the same as those by the experimental approach. However, great similarities exist between the two imaging approaches. Given that a bistatic image can be easily computed, significant diagnostic information can be obtained from computational algorithms for an insignificant incremental cost increase.

The bistatic k -space image algorithm has the following features:

- Applicable to any frequency domain EM computer code that computes a current distribution located on the target geometry, e.g., MOM, PO, and FEFD
- Images computed with the generalized bistatic radiation from the fixed current source
- Easily obtained resolution approaching 0.5λ
- One-, two-, or three-dimensional computed images
- Antenna images
- Scattering images
- Linear or circular polarization
- Backscatter or bistatic image directions
- Copolarized or cross-polarized images
- Single frequency and illumination angle
- No image smearing because \mathbf{k}_{down} , $\mathbf{k}_{\text{cross}}$, and \mathbf{k}_{vol} are independent

A similar bistatic technique not involving a current distribution has also been used by Bhalla and Ling (ref. 4) for a shooting bouncing ray trace computer code that is applicable to high-frequency scattering where only

specular scattering is computed. In their implementation, the bistatic scattered field is computed directly from the ray trace procedure after the ray bundles have been specularly reflected by one or more bounces from the target.

This report presents the development of the bistatic k -space image theory and shows its implementation and results for several EM computer code algorithms for a variety of geometric targets. Results are monostatic scattering oriented; however, one antenna application is illustrated. Three-dimensional images are also shown for several scattering geometries. Lastly, the theory for the swept frequency experimental image approach is reviewed and examples of measured images are presented for direct comparison with the analytical bistatic image approach.

Symbols

$A(\mathbf{k}), A(\mathbf{r})$	arbitrary function in k and position spaces
a	radial dimension, m
B	bandwidth, Hz
c	speed of light, m/sec
E	electric field, V/m
\mathbf{E}	electric field vector
$\hat{\mathbf{e}}_r$	receiver unit polarization vector
f	frequency, MHz or GHz
G	Green's function
H	magnetic field intensity, A/m
\mathbf{H}	magnetic field vector
$\hat{\mathbf{h}}$	magnetic field unit vector
\mathbf{J}	current distribution, A/m
j	$= \sqrt{-1}$
k	wave-number scalar, m^{-1}
\mathbf{k}	wave-number vector
$\hat{\mathbf{k}}$	unit wave-number vector
l	length
N	number of image computational points
$\hat{\mathbf{n}}$	surface normal vector
n	index; mode number
R	spatial position distance, m
\mathbf{R}	radiation transfer (row) matrix
\mathbf{r}	spatial position vector, m
r	spatial position, m
S	surface area, m^2
$W(k), W(\mathbf{k})$	window weight function, $0 < W(\mathbf{k}) < 1$
X, Y, Z	orthogonal coordinate axis

$\hat{\mathbf{z}}$	unit vector in Z direction
Δk	bandwidth in k space
Δr	image resolution
Δt	time delay
ϵ_r	relative dielectric constant
θ	polar (elevation) angle from Z -axis, deg
λ	wavelength, m
μ	permeability, H/m
ρ	electric charge density, C/m^3
σ	radar cross section, m^2
ϕ	azimuth angle, deg
ω	radian frequency ($2\pi f$), rad/sec
∂a	elemental area, m^2

Subscripts:

cross	cross-range direction
down	downrange direction
g , gain	gain
i, j, k	index
max	maximum
min	minimum
new	translated position
old	original position
r	radial direction
rot	rotated position
vol	volumetric direction
0	excitation condition

Superscripts:

e	excitation direction
i , inc	incident direction
p	port
radial	radial direction
s , scat	scattered direction
t	time
α	polarization variable

Abbreviations:

BOR	body of revolution
CW	creeping wave
DFT	discrete Fourier transform
EM	electromagnetic
EMCC	Electromagnetic Code Consortium
FD	frequency domain

FEFD	finite element frequency domain
FEM	finite element method
FFT	fast Fourier transform
GO	geometric optics
ISAR	inverse synthetic aperture radar
LU	lower and upper triangular matrix decomposition
MOM	method of moments
PEC	perfect electric conductor
PO	physical optics
RCS	radar cross section
SAR	synthetic aperture radar
TD	time domain
TW	traveling wave

Special notation:

dBi	decibel power level relative to isotropic for antenna gain patterns
dBsm	decibel power relative to 1.0 m ² for scattering cross section
dBλ	decibel power relative to wavelength for scattering cross section (2-D)
dBλ ²	decibel power relative to wavelength squared for scattering cross section (3-D)

Theory

This section outlines the bistatic k -space image theory and the generalization of the standard radiation integral. A later section will compare this bistatic computational image approach with the experimental image approach.

The bistatic k -space image technique is developed starting with the general Fourier transform.

A natural Fourier transform pair, a dimensionless number, is the vector dot product $\mathbf{k} \cdot \mathbf{r}$ of wave number \mathbf{k} and spatial location \mathbf{r} . These may be scalar quantities or may be vectors

$$\mathbf{k} \cdot \mathbf{r} = k_x r_x + k_y r_y + k_z r_z \quad (1)$$

where \mathbf{k} has magnitude $|\mathbf{k}| = 2\pi/\lambda$ and λ is the wavelength.

Given a source distribution $A(\mathbf{k})$ that is a function of the wave vector \mathbf{k} , its Fourier transform $A(\mathbf{r})$ is a function of spatial location (Brigham, ref. 5):

$$A(r_x r_y r_z) = \iiint W(\mathbf{k}) A(k_x, k_y, k_z) \times e^{j(k_x r_x + k_y r_y + k_z r_z)} dk_x dk_y dk_z \quad (2)$$

where $W(\mathbf{k})$ is a window weight function. This integral is the spatial image of the source function $A(\mathbf{k})$. Given $A(\mathbf{k})$ at a suitable number of points k_i , a standard Fourier transform such as a fast Fourier transform (FFT) or a discrete Fourier transform (DFT) is applied to obtain the image, i.e., the complex square amplitude $|A(\mathbf{r})|^2$. The previous integrations were written in terms of a standard rectangular coordinate system; however, image rectilinear coordinates will be downrange, cross-range, and volumetric.

Let the transform quantity A be identified as the scattered electric field E^s caused by a current distribution \mathbf{J} . If $E(\mathbf{k})$ can be computed, then an image $|E(\mathbf{r})|^2$ can be computed from equation (2).

Excitation

The scattered field E is defined in a bistatic sense, i.e., as a function of excitation \mathbf{k}^e and direction of scattered radiation \mathbf{k}^s ,

$$E^s = E^s(\mathbf{k}^e, \mathbf{k}^s) \quad (3)$$

The excitation which produced the current distribution on the body could be from a localized region or port on the body, as in the case of an antenna, or could be from an incident plane wave of given polarization and incident direction. If the excitation is from an incident plane wave, then \mathbf{k}^e is set equal to \mathbf{k}^i where \mathbf{k}^i is the wave vector of the incident radiation. For antenna problems where only a localized port or region has a voltage excitation, \mathbf{k}^e is set equal to \mathbf{k}^p where \mathbf{k}^p represents the local port and direction of the applied voltage.

Computing Images in k Space

The essential problem of computing an image is to compute the scattered field E as a function of k -space image coordinates. Orthogonal rectangular coordinates with uniform increments on each axis must be used for input to the FFT algorithm so that image smear and defocus do not occur. The natural orthogonal k -space vector coordinates for images are in the downrange, cross-range, and volumetric directions,

$$\mathbf{k} = (\mathbf{k}_{\text{down}}, \mathbf{k}_{\text{cross}}, \mathbf{k}_{\text{vol}}) \quad (4)$$

shown vectorially in figure 1.

An azimuth and elevation (θ, φ) angular direction in space is selected relative to the target to specify where the radiation image is to be obtained, i.e., the direction in space where the scattered (radiated) field from the target current distribution is to be evaluated. For scattering problems the angular location does not have to be in the same direction as the plane-wave illumination. The downrange direction is defined by the radial vector \mathbf{k}_r pointing toward the origin and the angular coordinates of the desired image (θ, φ) . (See fig. 1.)

The cross-range direction can be either \mathbf{k}_θ or \mathbf{k}_φ . This choice dictates the sense of rotation of the target for cross-range. In geometries such as airplanes where the X-axis is along the body (station line), the Y-axis is across the body (butt line), and the Z-axis is vertical (water line), the usual choice for cross-range is a rotation about the Z-axis, i.e., $\mathbf{k}_{\text{cross}} = \mathbf{k}_\varphi$. For bodies of revolution, the cross-range direction is in the polar direction, $\mathbf{k}_{\text{cross}} = \mathbf{k}_\theta$. Once the cross-range direction is chosen, the volumetric direction is then orthogonal to $(\mathbf{k}_r, \mathbf{k}_{\text{cross}})$, i.e., either \mathbf{k}_θ or \mathbf{k}_φ . Note that, while the natural vector directions for an image correspond to the spherical coordinate vectors, the image coordinates are rectangular, not curvilinear. The spherical unit vector directions are set by the image angular location choice (θ, φ) ,

$$\left. \begin{aligned} \hat{\mathbf{k}}_r &= (\sin\theta \cos\varphi, \sin\theta \sin\varphi, \cos\theta) \\ \hat{\mathbf{k}}_\theta &= (\cos\theta \cos\varphi, \cos\theta \sin\varphi, -\sin\theta) \\ \hat{\mathbf{k}}_\varphi &= (-\sin\varphi, \cos\varphi, 0) \end{aligned} \right\} \quad (5)$$

Thus, to compute an image, the scattered field in k space must be computed as a function of

$$E(\mathbf{k}_{\text{down}}, \mathbf{k}_{\text{cross}}, \mathbf{k}_{\text{vol}}) \quad (6)$$

for input to the Fourier transform.

Generalized Radiation Integral

The scattered k -space radiation field from the current distribution \mathbf{J} is calculated from a generalization of the standard radiation integral. Given a current distribution \mathbf{J} , the far-field radiation is

$$E^{\alpha, \text{scat}}(\mathbf{k}^{\text{scat}}, \mathbf{k}_r^e) = \int [\hat{\mathbf{n}}^\alpha \cdot \mathbf{J}(\mathbf{k}^e)] e^{j(\mathbf{k}^{\text{scat}} \cdot \mathbf{r}')} dS' \quad (7)$$

where the integration is over the source currents \mathbf{J} on the body and $\alpha = \theta$ or φ for the desired polarization of the scattered field.

If \mathbf{k}^{scat} was in the outward radial direction, $\mathbf{k}^{\text{scat}} = (2\pi/\lambda)\hat{\mathbf{k}}_r(\theta, \varphi)$, then equation (7) would be the usual radiation integral. In fact, the standard radiation

integral is the Fourier transform in the outward radial direction of the body current distribution.

For computed images, \mathbf{k}^{scat} is generalized to be a volume in k space,

$$\mathbf{k}^{\text{scat}} = (\mathbf{k}_{\text{down}}, \mathbf{k}_{\text{cross}}, \mathbf{k}_{\text{vol}}) \quad (8)$$

so that the Fourier transform of $E(\mathbf{k}^{\text{scat}})$ is the image:

$$\begin{aligned} E^\alpha(\mathbf{r}_{\text{down}}, \mathbf{r}_{\text{cross}}, \mathbf{r}_{\text{vol}}) \\ = \iiint W(\mathbf{k}) E(\mathbf{k}_{\text{down}}, \mathbf{k}_{\text{cross}}, \mathbf{k}_{\text{vol}}) \\ \times e^{j(\mathbf{k}_{\text{down}} \cdot \mathbf{r} + \mathbf{k}_{\text{cross}} \cdot \mathbf{r} + \mathbf{k}_{\text{vol}} \cdot \mathbf{r})} dk_{\text{down}} dk_{\text{cross}} dk_{\text{vol}} \end{aligned} \quad (9)$$

The square amplitude is then proportional to power, i.e., either radar cross section, σ , or antenna gain:

$$\sigma \propto |E^\alpha(\mathbf{r}_{\text{down}}, \mathbf{r}_{\text{cross}}, \mathbf{r}_{\text{vol}})|^2 \quad (10)$$

The radiation integral is used to compute the scattered field in k space; thus, the technique is given the name *bistatic k -space imaging*.

Focus and image smearing is not an issue with the bistatic k -space approach as it is with the experimental image approach. The $E(\mathbf{k})$ array can be computed at any arbitrary set of k_i points. Thus, if an evenly spaced orthogonal grid of points is chosen, focus and image smear can be prevented.

Image Resolution

The resolution of the image is the size of each down-range and cross-range cell. Scattering centers cannot be discriminated from each other when separated by less than the resolution dimension. With a decrease in the cell size, the position of the scattering centers can be determined more precisely. The resolution is set by the extent of the k -space region used to compute the bistatic fields. Downrange and cross-range resolutions can be set to different values but are considered to be equal herein to simplify the discussion. Given a desired image resolution Δr , the related k -space bandwidth Δk is

$$\Delta k = \frac{2\pi}{\Delta r} \quad (11)$$

The downrange \mathbf{k}_{down} vector sweep is centered about the free-space wave number for the excitation wavelength (fig. 2):

$$|\mathbf{k}_{\text{down}}| = k_0 \pm \frac{\Delta k}{2} \quad (12)$$

where $k_0 = 2\pi/\lambda_0$ and λ_0 corresponds to the excitation wavelength. The downrange image scattered field is thus swept about the excitation wavelength.

At 0.5λ resolution, $\Delta r = \lambda/2$, and the k -space bandwidth from equation (11) is $2k_0$. From equation (12), the corresponding minimum and maximum downrange k_r values are

$$\left. \begin{aligned} k_{r,\min} &= 0 \\ k_{r,\max} &= 2k_0 \end{aligned} \right\} \quad (13)$$

where the maximum downrange k is twice the incident k_0 value.

If the resolution is greater than $\lambda/2$, the downrange k_r direction changes sign, i.e., the bistatic field is being computed from the opposite side of the target. When this occurs, forward-scatter bistatic data are being included in the image computation.

The extent of the image in each direction sets the number of points N computed along each image axis,

$$N = \frac{\text{Spatial extent}}{\Delta r} \quad (14)$$

where N is the order of the Fourier transform. If N is not a power of 2, the data can be zero padded up to the next power of 2 for input to a FFT. The spatial extent can be different for each direction but is chosen equal in this discussion.

Note in equation (11) that the image resolution depends solely upon the bandwidth extent of the k -space data and is not theoretically constrained to any particular value. However, practical guidelines must be considered to compute images with properly located scattering centers. Experimental imaging issues are discussed in the appendix.

Selection of Image Resolution

One constraint on the image resolution is the discrete nature of the underlying electromagnetic analysis. Typically, EM computer codes break the problem into meshes whose elements have sizes that are a fraction of a wavelength; a size of 0.1λ is common. If the resolution and the dimension of individual elements of the mesh are approximately the same, each mesh becomes a *false scattering center* in the image. The use of 0.5λ or greater resolution avoids this problem.

A second consideration is to determine what physical size is associated with the concept of a scattering center because resolution cells larger than scattering center dimensions are usually desirable. While the scattering center concept is well founded, it is not well defined in

terms of wavelength. The minimum size that constitutes a scattering center needs to be estimated. Certainly 0.5λ is a lower bound, and 1.0λ to 2.0λ is probably more realistic. Targets which are less than several λ in size could use the lower resolution bound, while targets many λ in size could use resolution sizes much greater.

Another guideline for the resolution size is related to the bandwidth of k -space data used in the image computation. The objective of the image process is to identify scattering centers for a single incident and scattered field angle (herein called the “image angle”). Note in equation (12) and figure 2 that the image data are centered around the scattered field free- k -space vector. As the resolution is decreased, a wider bandwidth of bistatic angular data are required to compute the image. Because scattering centers are a function of incident and scattered field directions, scattering centers may change drastically when a wide bandwidth of k space is imaged. The image will then include scattering centers not associated with the desired image angles. For an extreme example, a 0.5λ resolution for a 3-D volumetric image samples the bistatic radiation in the half-space 2π sr of the target.

The bistatic angular bandwidth requirements for various resolutions are shown in figure 3. These bandwidths are computed with the downrange \mathbf{k}_r set to \mathbf{k}_0 and represent the bistatic view angle range when $\mathbf{k}_{\text{down}} = \mathbf{k}_0$. Figure 3 shows that with an increase in resolution cell size, the bandwidth of k -space data can be reduced, and the image can reflect scattering centers at the image angle more accurately because less bistatic angle data are utilized.

To demonstrate the changes that occur in the image as the resolution is increased, the Electromagnetic Code Consortium (EMCC) 2-D Benchmark 1 (ref. 6) is imaged by a 2-D finite element frequency domain computer code at 300 MHz with resolutions from 0.5λ to 2.0λ . The geometry and images are shown in figure 4. Figure 4(b) shows images for horizontal polarization; figure 4(c) shows images for vertical polarization. The radar is located at the bottom and propagates from bottom to top along the downrange axis. The bistatic data are centered around the incidence angle to create a backscatter image. Image contours are separated by 5 dB of echo width, from a minimum contour of -30 dB λ .

For 0.5λ resolution in figure 4(b), the leading- and trailing-edge diffraction scattering centers are apparent, and a separate diffraction from the dielectric tip as well as the top of the perfect electrical conductor (PEC) is observed. However, this image indicates a -25 -dB scattering center along the ogival shape from leading edge to trailing edge. This is most likely a *surface wave* scattering center, where energy in the dielectric coating is escaping along the length of the ogive and is being

reradiated in the directions being sampled for wide angle bistatic image. As the image resolution cell size is increased from 0.5λ to 1.5λ in figure 4(b), the surface wave scattering center disappears because of the reduced k -space bandwidth, indicating that it is not a strong scatterer in the backscatter direction.

Images of the same geometry at vertical polarization are shown in figure 4(c). In these images, the minimum contour represents $-5 \text{ dB}\lambda$ and each contour is separated by 5 dB. The 0.5λ and 2.0λ resolution images are shown.

At vertical polarization, a propagating trapped wave is not expected and is not observed in figure 4(c). The primary scattering for this polarization is the diffraction from the leading edge of the metallic ogive.

In summary, different resolution cell sizes provide different insights into scattering mechanisms of bodies. However, the user must be aware of the problems associated with choosing a small resolution, e.g., the finite element method (FEM) discretization and the wide bandwidth requirement.

k -Space Computational Points

The downrange \mathbf{k} vector is centered on the free-space wave number $2\pi/\lambda$, and $E(\mathbf{k}^{\text{scat}})$ is computed from equation (7) at the \mathbf{k}^{scat} locations:

$$\mathbf{k}_{i,j,k}^{\text{scat}} = \left[\frac{2\pi}{\lambda} + \frac{(i-0.5)}{N} \Delta k \right] \hat{\mathbf{k}}_{\text{down}} + \left[\frac{(j-0.5)}{N} \Delta k \right] \hat{\mathbf{k}}_{\text{cross}} + \left[\frac{(k-0.5)}{N} \Delta k \right] \hat{\mathbf{k}}_{\text{vol}} \quad (15)$$

where the range over $(i, j, k) = ((-N/2) + 1, N/2)$. This forms a cubic volume in k space centered at $k_{\text{down}}(\theta, \varphi) = 2\pi/\lambda$ over which $E(\mathbf{k})$ is computed from equation (7) on a uniformly spaced rectangular grid.

Fourier Transform Issues

The $E(\mathbf{k})$ -computed array is one-, two-, or three-dimensional depending on the type of image desired, i.e., downrange, downrange-cross-range, or volumetric, respectively. The next step is to window the respective data array with a weight function to reduce the signal-processing side lobes in the resulting Fourier transform where $0 \leq W(\mathbf{k}) \leq 1$. Many choices are possible such as rectangular (no weights), Hamming, and Hanning. For square or volumetric $E(\mathbf{k})$ arrays, the usual approach has been to multiply each row and column separately by

$W(\mathbf{k}_i)$. An alternate method (ref. 5) is to use a radially symmetric weight function $W(k_{i,j,k}) = \sqrt{k_i^2 + k_j^2 + k_k^2}$.

After the $E(\mathbf{k})$ data array has been multiplied by the desired weight function, the next step is to pad the array from N up to the next power of 2 to utilize an FFT algorithm. Additionally, smoother image data, albeit without improved resolution, can be obtained by padding the $E(\mathbf{k})$ array with additional zeros beyond the first required 2^n .

As determined by the particular FFT algorithm, the resulting $E(\mathbf{r})$ data have to be re-sorted by quadrants to put the $\mathbf{r} = 0$ point at the center of the array. An additional task is to form the scalar square amplitude because power rather than electric field is the usual image quantity of interest. Phase information is not used. Scaling of the image data may also be required depending again on the particular FFT algorithm utilized. Finally the image data are usually expressed in decibel form: typically dBsm is used for scattering, while dBi, the power gain relative to isotropic, could be used for antenna cases.

Image Center of Rotation

The rotation image center is at the coordinate center of the EM geometry model describing the current distribution. Often this origin is at one end of the body, such as at the nose of an airplane. A simple phase shift of the $E(\mathbf{k})$ data can be used to move the center of rotation to any desired location.

The image is computed with various downrange and cross-range values of \mathbf{k}^{scat} . Downrange direction implies that the corresponding radial direction points toward the origin of the coordinate system. This origin is then the center of the image window extent for the resulting image. Often, however, the coordinate system for the body geometry has an origin that is not located at the center of the window extent. For example, most airplane coordinate systems define an origin at or near the airplane nose. For imaging, one would like to place the origin midway down the body so that the resulting image fills the window extent. To accomplish this translational shift of coordinates, a user could change all the airplane coordinates in the geometry model files. A simpler approach is to introduce a phase shift that corresponds to the desired coordinate translation.

The k -space scattered field for the original or *old* bistatic scattered field radiation integral is

$$E_{\text{old}}^{\text{scat}}(\mathbf{k}^s) = \iiint \mathbf{J}(\mathbf{k}^i, \mathbf{r}) e^{-j\mathbf{k}^s \cdot \mathbf{r}} dS \quad (16)$$

When a new reference origin \mathbf{r}_{new} is defined relative to the old body origin, the new image transform becomes

$$\left. \begin{aligned} E_{\text{new}}^{\text{scat}}(\mathbf{k}^s) &= \iiint \mathbf{J}(\mathbf{k}^i, \mathbf{r}) e^{-j\mathbf{k}^s \cdot (\mathbf{r} - \mathbf{r}_{\text{new}})} dS \\ E_{\text{new}}^{\text{scat}}(\mathbf{k}^s) &= e^{j\mathbf{k} \cdot \mathbf{r}_{\text{new}}} \iiint \mathbf{J}(\mathbf{k}^i, \mathbf{r}) e^{-j\mathbf{k}^s \cdot \mathbf{r}} dS \\ E(\mathbf{k}^s) &= e^{j\mathbf{k} \cdot \mathbf{r}_{\text{new}}} E_{\text{old}}^{\text{scat}} \end{aligned} \right\} \quad (17)$$

Therefore, a coordinate shift is implemented as a phase shift at each k -space scattered field value prior to calculation of the Fourier transform of the data. Remember that the coordinate rotation matrix then applies for each given viewing angle:

$$\begin{bmatrix} x_{\text{rot}} \\ y_{\text{rot}} \end{bmatrix} = \begin{bmatrix} \cos \theta & -\sin \theta \\ \sin \theta & \cos \theta \end{bmatrix} \begin{bmatrix} x \\ y \end{bmatrix} \quad (18)$$

Discussion

The bistatic k -space image technique offers several advantages when compared with the experimental sweep frequency angle rotation images. The source current distribution $\mathbf{J}(\mathbf{k}^i, \mathbf{r})$ is fixed, i.e., does not vary with \mathbf{k}^{scat} . This means that the resulting image is from a current distribution that does not vary with incident frequency or with rotation angle as is the case with experimental images. No questions are posed as to what frequency and angle the resulting image represents as is often the case with the experimental approach. Experimental images utilize monostatic (backscatter) radiation as a function of frequency and rotation angle to form an image, while the bistatic k -space approach uses bistatic fields from a fixed current distribution.

The most important advantage of this technique is that only one current distribution $\mathbf{J}(\mathbf{k}^i, \mathbf{r})$ is required. For computer codes such as MOM, the matrix needs to be computed at only the frequency of interest, and only one voltage vector excitation is required to obtain the desired current distribution. The computation of the $E^{\text{scat}}(\mathbf{k}^s)$ array is equivalent to the computation of a bistatic scattered field, which typically requires a very small percentage of the overall MOM computational effort.

Another advantage is that traveling-wave current sources are imaged over the regions of their existence. This occurs because the source excitation frequency is fixed, whereas for the experimental case, the source excitation frequency varies. In the latter case, radiations from traveling-wave currents image at the reflection points which have stationary phase. Thus the bistatic-imaging

technique produces images that have a truer representation of the radiation from the current distribution \mathbf{J} .

Implementation and Example Results

Method-of-Moments Computer Code Implementation

The implementation of the bistatic k -space images into a MOM computer code involves development of subroutines to compute $E^{\text{scat}}(\mathbf{k}^s)$ at the required points in k space as well as routines to perform the FFT and to scale and present the image data. Actual computation of $E^{\text{scat}}(\mathbf{k}^s)$ can be accomplished with the standard MOM row measurement vector subroutines with only slight modifications. Scattered fields in MOM are computed from the inner product of the current vector \mathbf{J} and the row measurement vector \mathbf{R}^α evaluated for the radiation at the desired azimuth and elevation angle,

$$E^{\alpha, s}(\theta, \varphi) = \mathbf{R}^\alpha(\theta, \varphi) \mathbf{J}(\mathbf{k}^i) \quad (19)$$

where $\alpha = \theta$ or φ polarization of the scattered field. The row measurement vector is defined (ref. 7) as

$$\mathbf{R}_i^\alpha(\theta, \varphi) = \langle \hat{\mathbf{n}}^\alpha \cdot \mathbf{J}_i, e^{-j\mathbf{k}_r(\theta, \varphi) \cdot \mathbf{r}} \rangle \quad (20)$$

where $\mathbf{k}_r(\theta, \varphi)$ is the radial wave-number vector with amplitude $2\pi/\lambda$, pointing to the desired polar and azimuth angle, \mathbf{J}_i is the current basis function, and $\langle \rangle$ represents a generalized inner product.

For computation of bistatic fields, the row measurement vector is redefined by replacement of the radial \mathbf{k}_r , which is a function of θ and φ , with the nonradial \mathbf{k}^s defined by equation (15),

$$\mathbf{R}_i^\alpha(\mathbf{k}^s) = \langle \hat{\mathbf{n}}^\alpha \cdot \mathbf{J}_i, e^{-j\mathbf{k}^s \cdot \mathbf{r}} \rangle \quad (21)$$

so that $E(\mathbf{k}^s)$ is computed as

$$E^{\alpha, s}(\mathbf{k}^s) = \mathbf{R}^\alpha(\mathbf{k}^s) \mathbf{J}(\mathbf{k}^i) \quad (22)$$

The row measurement computational subroutine, often the voltage vector routine, can usually be modified to compute equation (21) rather than equation (20). To compute equation (20), a Cartesian vector \mathbf{k}_r as a function of (θ, φ) is formed in the subroutine. A simple change to input a Cartesian vector \mathbf{k}^s as input to the row measurement computational subroutine can be made. Then equation (21) is computed with the same routine as equation (20).

The vector frame of reference used to compute equation (20) or (21) is typically that of the target body

coordinate system. Hence, the \mathbf{k}^s vector, composed of the components \mathbf{k}_{down} , $\mathbf{k}_{\text{cross}}$, and \mathbf{k}_{vol} , is

$$\mathbf{k}^s = \mathbf{k}_{\text{down}} + \mathbf{k}_{\text{cross}} + \mathbf{k}_{\text{vol}} \quad (23)$$

This must be expressed in the target reference Cartesian form for input to the row measurement vector subroutine. For a given elevation and azimuth angle of the image, the Cartesian representation for \mathbf{k} becomes (eq. (5) and fig. 1)

$$\left. \begin{aligned} k_x &= k_{\text{down}} \sin \theta \cos \varphi - k_{\text{cross}} \sin \varphi \\ k_y &= k_{\text{down}} \sin \theta \sin \varphi - k_{\text{cross}} \cos \varphi \\ k_z &= k_{\text{down}} \cos \theta \end{aligned} \right\} \quad (24)$$

This vector is input to the modified row measurement routine used to compute bistatic radiation.

Patch Method-of-Moments Computer Code Example Results

The results presented are for several examples that use the three-dimensional method-of-moments patch computer code MOM3D. (See ref. 2.)

Square plate. Results for the first example of a 3.0λ -square plate show 1-D downrange and 2-D downrange-cross-range for three view directions: (1) perpendicular to the plate, which illustrates specular scattering, (2) perpendicular to the edges at an elevation angle of 10° , which illustrates leading and trailing-edge scattering, and (3) along the plate diagonal at an elevation angle of 10° , which illustrates edge- and traveling-wave scattering. The wavelength was 1 m; thus, the scattering amplitudes, while presented in units of dBsm, may also be interpreted in units of $\text{dB}\lambda^2$.

The plate computational triangle mesh, shown in figure 5(a), was composed of 512 triangles and resulted in 736 couples for an average sample density of 82 unknowns per square wavelength. The horizontal and vertical polarization backscatter from this plate for a principal plane cut and a cut through the plate diagonal is shown in figure 5(a). The images were computed at a resolution of 0.5λ and were processed with a Hanning weighting function.

The bistatic images are centered on the backscatter direction. The 1-D coordinate system is reversed from normal presentation, i.e., the downrange direction axis is vertical and the radar cross section amplitude scale is horizontal. This orientation allows the 1-D and 2-D images to be placed side by side for comparative purposes. The 2-D downrange-cross-range contour images are presented in the usual way with the horizontal axis being cross-range and the vertical axis being downrange.

The radar illumination source is centered beneath each image. Each contour line represents a 10-dB increment with the minimum contour set to -30 dBsm.

View 1 in figure 5(b) shows the 1-D downrange and 2-D downrange-cross-range images perpendicular to the plate. For this plate, the physical optics cross section is $\sigma = 4\pi A^2/\lambda^2 = 30$ dBsm. This is the peak value for the downrange image and for the polar plot in figure 5(a). When one scattering mechanism dominates a given illumination angle, as is the case here, the 1-D downrange peak scattering amplitude matches the polar plot coherent RCS level. If two or more scattering mechanisms of nearly equal amplitude are present, then the polar coherent level does not usually match the downrange image peak values and depends on how two or more scattering centers add (or subtract) in phase.

The 2-D contour image shows equal scattering across the breadth of the plate. The scattering lobes in front and behind the plate are the FFT signal-processing side lobes (different windowing functions can reduce the side lobes). The 2-D amplitudes are not the same levels as the coherent peak RCS or the downrange peak. The 2-D amplitudes include the highly coupled effects of target cross-range dimension, resolution, and extent. (See appendix for discussion of 2-D amplitudes.) Therefore, the chief value of the 2-D images is to illustrate locations of scattering centers and their relative amplitudes.

View 2 in figure 5(c) shows images at a 10° elevation perpendicular to the plate edges; scattering from the leading and trailing edges of the plate is indicated. For parallel (horizontal) polarization, the leading edge is brighter and has a magnitude close to the edge value of $\sigma = l^2/\pi = 4.5$ dBsm. The 1-D and 2-D images clearly show the leading edge as the dominant scatterer. Because this is horizontal polarization, two edge waves are also reflecting from the rear plate vertices. For perpendicular (vertical) polarization, the trailing edge is the dominant scatterer as shown in the 1-D and 2-D images. Because this plate is in the resonant region, this trailing-edge return is interpreted as a surface traveling wave (TW) reflected from the trailing edge. The view angle, at a 10° elevation, is well below the peak amplitude for this scattering mechanism, which occurs near $\sigma_{\text{TW}} = 49(\lambda/l)^{1/2} \approx 28^\circ$ elevation as shown in the coherent RCS plot. The trailing-edge-reflected traveling-wave images with a peak at the back edge and decreases in amplitude as the reflected wave decays because of radiation energy loss.

View 3 in figure 5(d) shows images at a 10° elevation along the plate diagonal (45° azimuth); the edge- and traveling-wave scattering are dominant. For parallel (horizontal) polarization, diffraction from the front vertex and edge traveling-wave reflection from the two side

vertices are evident. Not much energy is reflected from the rear vertex. The 1-D downrange image shows that the returns of the two vertices are at the same downrange location and have the same phase; hence, they add and are superimposed on each other. The left-right asymmetry in the 2-D image is due to the computational triangle mesh-couple asymmetry. For perpendicular (vertical) polarization, note that the only scattering mechanism is a surface traveling wave being reflected from the rear vertex tip.

NASA almond. In the second example, 2-D images are presented from the results of the MOM3D computer code applied to the NASA almond shown in figure 6. The NASA almond (ref. 8) is a doubly curved surface with a pointed tip. It has low RCS when viewed in the tip angular sector. Elsewhere, a surface normal is always pointing back toward the radar creating a bright high-level specular RCS return. In addition to specular mechanisms, surface traveling waves (TW) and creeping waves (CW) contribute to the scattering. The almond is $9.936 \times 3.84 \times 1.26$ in. in length, width, and thickness, respectively.

The 2-D images of the 9.936-in. NASA almond were meshed and computed with a numerical solution to Maxwell's equations. Hence, all scattering physics are included in the computational model: specular, edges, surface wave, and shadowing. Results for horizontal and vertical polarization are presented in figures 6 and 7, respectively. The frequency is 9.92 GHz, which makes the almond 8.34λ in length so that the scattering regime is just inside the optics region.

The RCS and 2-D images were computed by the MOM3D computer code. (See ref. 2.) The pointed tip is oriented at 180° azimuth angle with the blunt end at 0° azimuth. The azimuth plane monostatic RCS computations are shown in figures 6 and 7 for horizontal and vertical polarizations, respectively. The lower RCS tip region is the aft sector from $\pm 120^\circ$ where the signature is dominated by surface traveling waves reflected from the aft vertex. In this sector no specular scattering occurs. Outside of the aft tip sector the scattering is due mostly to specular returns with some surface wave scattering adding in and out of phase. Downrange-cross-range 2-D images are shown in figures 6 and 7 for horizontal and vertical polarizations, respectively, at increments of 15° from 0° to 180° in azimuth angle.

The specular nature of the scattering is clearly evident on this target from 0° to 120° where there is always a surface normal pointing back toward the transmitter-receiver. This doubly curved geometric optics specular return is $\sigma_{GO} = \pi R_1 R_2$ where R_1 and R_2 are the surface radii of curvature at the specular point (where the surface

normal points back toward the source). Hence, those regions on the almond where R_1 and R_2 are large will have a high RCS as shown in the 90° broadside image. When viewed in the region of 135° to 180° , a tip return due to the tip current discontinuity and a surface creeping wave which spins around the target are evident.

Airplane configuration. The next example from MOM patch computer code results is a 3.7λ commercial transport configuration shown in figure 8(a). The excitation frequency was 6 GHz at horizontal polarization, which corresponds to approximately 24 to 30 MHz for a full-scale airplane. The MOM3D computer code was utilized for this example with the left-right symmetry option. The mesh model was composed of 4575 triangles, which resulted in 6733 unknown current couples for 813 unknowns per square wavelength. The images were computed at a 0.5λ resolution. The azimuth cut RCS for 0° elevation is shown in figure 8(b). The nose of the airplane corresponds to 0° azimuth. The scattering regime for this case is in the resonant regions because this configuration is less than 10λ in length. Therefore, in addition to specular scattering mechanisms, nonspecular surface-, edge-, and creeping-wave returns contribute to the signature.

Two-dimensional downrange-cross-range images are presented at increments of 15° from nose to tail on aspect angles for horizontal polarization. Characteristics observed in the images are summarized as follows:

- At 0° , the dominant scattering centers are the engine pods and traveling-wave reflection from the wing roots.
- At 15° , the leading edge of the left wing becomes dominant because of edge diffraction.
- At 30° , the left wingtip and wing root dominate.
- At 45° , note a specular return from the forward fuselage, an edge return from the rear stabilizer, returns from the left wingtip and wing root, and a return from the rear engine pod.
- At 60° , the returns are similar to those at 45° .
- At 75° , specular mechanisms (surface normal pointing back toward the illumination source) are apparent from the forward fuselage and engine pod as well as a traveling-wave (TW) return from the stabilizer root.
- At 90° broadside, specular returns from the fuselage, vertical fin, and engine pod dominate the scattering. At this angle, the presence of the wing shields (i.e., shorts out) some of the incident field on the fuselage.
- At 105° , the scattering centers are the rear fuselage and engine pod.
- At 120° , the left trailing-edge wing root is dominant.

- At 135°, the trailing edge of the left wing and the stabilizer are peak scattering centers.
- At 150°, a TW return from the vertical fin is the peak scatterer.
- At 165°, scattering is minimal with multiple low-level returns from the wing and stabilizer tips and edges.
- At 180° (tail-on), the peak scattering center is the stabilizer trailing edge.

Body-of-Revolution MOM Computer Code Implementation

In BOR-MOM computer codes, the fundamental coordinate system is cylindrical (ρ, ϕ, z) with orthogonal radial, azimuthal, and axial components. In this case the row measurement subroutine is based on \mathbf{k}_ρ , \mathbf{k}_z , and ϕ where $(\mathbf{k}_\rho, \mathbf{k}_z)$ are a function of the polar angle θ of the desired field computation. In the BOR-MOM formulation, the n th-modal scattered field at (θ, ϕ) is

$$E_n^{\alpha,s}(\theta, \phi) = e^{jn\phi} R_n^\alpha(\theta) \mathbf{J}_n \quad (25)$$

where R_n and \mathbf{J}_n are the n th-modal row measurement and current column vectors, respectively. The computation of R requires \mathbf{k}_ρ - and \mathbf{k}_z -vector components as functions of θ inside the row or voltage matrix subroutine. These \mathbf{k} -vector components are computed inside the R subroutine as

$$\left. \begin{aligned} k_\rho &= \frac{2\pi}{\lambda} \sin \theta \\ k_z &= \frac{2\pi}{\lambda} \cos \theta \end{aligned} \right\} \quad (26)$$

Note that the row (or voltage) matrix is a function only of the polar angle θ . For bistatic imaging, the R subroutine can be modified to input the \mathbf{k}^s vector directly. The bistatic scattered field is computed with \mathbf{k}_ρ and \mathbf{k}_z input to the row measurement subroutine with the definitions (fig. 9) of

$$\left. \begin{aligned} \mathbf{k}_\rho &= -\mathbf{k}_{\text{down}} \sin \theta + \mathbf{k}_{\text{cross}} \cos \theta \\ \mathbf{k}_z &= -\mathbf{k}_{\text{down}} \cos \theta - \mathbf{k}_{\text{cross}} \sin \theta \end{aligned} \right\} \quad (27)$$

For the BOR, the cross-range direction is in the polar θ direction because by definition the body is rotationally symmetric in azimuth ϕ .

For BOR volumetric images, \mathbf{k}_{vol} is in the azimuthal ϕ direction shown in figure 10. Thus, the bistatic BOR radiation is computed at an azimuth angle of

$$\phi^s = \arctan\left(\frac{k_\phi}{k_{\rho|\phi=0}}\right) \quad (28)$$

and a new \mathbf{k}_ρ is computed as

$$k_{\rho|\phi=\phi^s} = \sqrt{(k_{\rho|\phi=0})^2 + k_\phi^2} \quad (29)$$

Note that \mathbf{k}_z does not require modification because it is not a function of \mathbf{k}_ϕ .

From the previous discussion, the computation of the bistatic $E^s(\mathbf{k}^s)$ image array can be accomplished with minor changes to the existing algorithms that compute scattered radiation from a current distribution \mathbf{J} .

Body-of-Revolution Image Examples

Sphere. The first BOR example is a sphere ($ka = 4$) of radius $a = 0.636\lambda$ (circumference equal to 4λ). This puts the sphere in the resonant regime for scattering where the two scattering mechanisms are the specular front face reflection and the two lower level surface creeping waves propagating around the back (shadow) side. The BOR computer code used for this example is described in the appendix of reference 9. The sphere-generating curve was composed of 62 segments resulting in 61 triangle functions and 122 (2×61) t and ϕ unknowns per Fourier mode. The number of modes was $ka + 1 = 5$. The sample density was 31 triangles per wavelength of the generating curve; the wavelength was 1.0 m.

The net RCS is the phasor sum of the front face and creeping-wave returns, which is approximately 0 dBsm. The 1-D and 2-D images are shown in figure 11 where the front face and rear creeping-wave scattering mechanisms are clearly evident. The front face specular reflection is equal to $\sigma_{\text{GO}} = \pi a^2 = 1.27 \text{ m}^2 = 1.05 \text{ dBsm}$, which is the value shown in the 1-D downrange image. The creeping-wave contribution shown in the downrange image is approximately -12 dBsm and originates from the rear of the sphere. The creeping wave in vertical polarization is over the top and bottom of the sphere, while in horizontal polarization, the creeping-wave path is on each side. The horizontal and vertical polarization returns are the same as required by geometrical considerations.

Airplane configuration BOR-PATCH model. A hybrid BOR-PATCH configuration target is the previous airplane configuration (MOM-patch computer code) with the fuselage modeled as a body of revolution and the wings, engines, and control surfaces patch modeled with triangles. The BOR-PATCH computer code from reference 9 was utilized for this image computation. The fuselage-generating curve was composed of 73 triangles for 72 t and ϕ BOR unknowns for a total of 144 BOR unknowns. The number of BOR modes was three. The wings, engines, and control surfaces were modeled

exactly as in the all-patch representation. The principal characteristics of the hybrid model are that the wing-fuselage and control-surface-fuselage interfaces were not electrically connected surfaces, i.e., the patches were not overlapped onto the BOR fuselage, and the slight mold line changes for the fuselage crew station were neglected. The configuration is shown in figure 12 along with the horizontal polarization azimuth-cut monostatic RCS. The 2-D downrange-cross-range images are presented in figure 12 at increments of 15° from 0° to 180° , just as was done before in figure 8. The resolution of 0.5λ was also as before. As expected, the BOR-patch and all-patch models show very similar scattering centers and levels. The two models, while very similar, are not quite electrically the same; the BOR-patch model does not include the electrical connection and the crew station.

Physical Optics Computer Code Implementation

Physical optics computational models are another class of EM algorithms to which bistatic k -space imaging can be applied. In physical optics the body current distribution is determined by the incident magnetic field. No matrix fill or LU factorizations are required as with MOM. For PO, the experimental swept-frequency-angle-rotation approach to imaging could be used to create computational images without computational penalty. However, the bistatic technique can also be used to provide the advantage of imaging radiation from a single-current distribution, i.e., the currents resulting from one frequency and one illumination angle excitation.

The physical optics assumption for the currents induced on a PEC surface from an incident plane wave is that, on the illuminated portions of the surface, the currents are twice the incident tangential magnetic field:

$$\mathbf{J}_{\text{PO}} = 2\hat{\mathbf{n}} \times \mathbf{H}^i \quad (30)$$

where $\hat{\mathbf{n}}$ is the local surface normal. On the shadow surfaces the currents are assumed to be zero. The PO current assumptions hold well for surfaces greater than several λ in size with a radius of curvature greater than several λ . Physical optics does not hold near edges and, thus, does not predict edge diffraction scattering or nonspecular scattering phenomena such as traveling, edge, and creeping waves. Nevertheless, PO is a useful optics regime computational model for those geometries where nonspecular mechanisms are insignificant. Physical optics, by its very optics nature, is polarization independent. The PO algorithms can also be constructed to include edge diffraction models to account for these polarization-dependent scattering mechanisms.

The scattered field from physical optics currents in direction \mathbf{k}^s due to surface currents induced by a plane wave with incident direction \mathbf{k}^i is expressed in cross-sectional form (ref. 3) as

$$\sqrt{\sigma}^\alpha = \frac{jk}{\sqrt{\pi}} \iint \hat{\mathbf{n}}^\alpha \cdot (\hat{\mathbf{e}}_r \times \hat{\mathbf{h}}^i) e^{-j(\mathbf{k}^i - \mathbf{k}^s) \cdot \mathbf{r}} dS \quad (31)$$

where $\hat{\mathbf{n}}^\alpha$ is the local surface normal, $\hat{\mathbf{e}}_r$ is the receiver unit polarization vector, and $\hat{\mathbf{h}}^i$ is the incident magnetic field. For the usual PO integral the spatial directions of \mathbf{k}^i and \mathbf{k}^s are radial, i.e., in the directions of incidence (excitation) and scattering, respectively, and are functions of the polar and azimuthal angles (θ , ϕ). The scalar magnitude of each is equal to the free-space wave number $|\mathbf{k}| = 2\pi/\lambda$.

For bistatic k -space imaging, the radial \mathbf{k}^s vector is replaced with

$$\mathbf{k}^s = \mathbf{k}_{\text{down}} + \mathbf{k}_{\text{cross}} + \mathbf{k}_{\text{vol}} \quad (32)$$

where \mathbf{k}_{down} , $\mathbf{k}_{\text{cross}}$, and \mathbf{k}_{vol} are given by equation (15).

Now \mathbf{k}^s is not radial (except for downrange-only images) and its magnitude is not equal to the free-space wave number. For a given resolution and image extent, the $\sqrt{\sigma(\mathbf{k}^s)}$ array is computed by equation (31) with equation (32) for input to the FFT algorithm that produces the image. Conceptually, bistatic k -space imaging for PO computer codes is reasonably straightforward to implement.

Physical Optics Image Examples

NASA almond. The first example of a physical optics image will be the NASA almond whose geometric description was presented earlier. This target is a pointed tip with doubly curved geometry, which has low RCS when viewed in the tip angular sector (Azimuth = 180°). (See fig. 13.) Outside of the low frontal sector, a surface normal is always pointing back toward the radar creating a bright high-level specular RCS return.

The RCS and 2-D images were computed with the PO PIXEL computer code from reference 10. The monostatic RCS at 9.92 GHz is presented in figure 13. At this frequency the almond is 8.34λ in length, which places the scattering regime just inside the optics region. The PIXEL computer code model is pure PO; hence, the backscatter results are polarization independent. Edge diffraction is not included in the model. Also, as is always the case with any PO computer code, a discontinuity exists in current from the illuminated region to the shadow region. This shadow boundary current discontinuity creates a *false* RCS return. This phenomenon is

shown in some of the 2-D images in figure 13, most predominately at Azimuth = 90°. The so called “poor man’s” shadowing was used, i.e., only those facets whose surface normal point into the half space occupied by the transmitter-receiver are included in the PO computation.

Downrange–cross-range 2-D images are shown in figure 13 at 15° increments of azimuth angle from 0° to 180°. Again, the specular nature of the scattering is clearly evident on this target from 0° to 120° where a surface normal is always pointing back toward the transmitter-receiver. When viewed in the region of 135° to 180°, a tip return due to the tip current discontinuity is apparent. The false shadow boundary RCS is clearly shown in the 180° tip view and at broadside 90° and shows to a lesser extent in the other views.

Airplane configuration. Our PO example of an airplane configuration uses the same triangle-faceted model as was used in the all-patch MOM3D image example in figure 8 at the same 6-GHz frequency. As such, the airplane is more appropriately in the resonant regime rather than in the optics scattering regime where PO is more appropriate. Nevertheless, the same geometric model was analyzed with the PO PIXEL computer code. The PO monostatic RCS for an azimuth cut at 0° elevation is shown in figure 14.

The 2-D downrange–cross-range images, computed with the same 0.5λ resolution as before, are presented at increments of 15° from 0° to 180° in figure 14. Comparison of these PO images with those computed from MOM3D (fig. 8) is instructive. When specular scattering dominates the RCS, such as broadside to the airplane, PO and MOM3D produce similar RCS levels. In the front and rear sectors, where edge diffraction and surface wave phenomena dominate scattering, the PO-predicted results are much lower than the MOM3D predictions.

Finite Element Frequency Domain Computer Code Implementation

The implementation of the imaging algorithm to finite element frequency domain computer codes requires that the near-field to far-field transform be modified to compute the scattered fields for the various \mathbf{k}_{down} and $\mathbf{k}_{\text{cross}}$ values. Several transforms are used to compute FEFD far-field data. The harmonic expansion, the Green’s theorem integral, and the volume source integral methods are described in reference 11. The bistatic-imaging technique is very difficult to implement in the harmonic expansion method and will not be discussed.

The Green’s theorem integral uses the tangential fields on a surface surrounding the scatterer to determine

surface equivalent currents. These equivalent sources are integrated to the far field. However, uniqueness of the actual sources on the scatterer is lost, and this method is not useful for this type of imaging.

The volume source integral far-field transform uses the actual sources on the scatterer to compute the far field, as is typically done in moment method far-field calculations. The volume source integral transform for horizontal polarization is given by

$$\begin{aligned} \mathbf{H}^s(\rho) = & k^2 \iint_V (\mu_r - 1) \mathbf{H}^t(\rho') G(\rho, \rho') \partial a' \\ & + \iint_V \left[\hat{\mathbf{z}} \cdot \nabla \times \frac{\epsilon_r - 1}{\epsilon_r} \nabla \times \mathbf{H}^t(\rho') \right] G(\rho, \rho') \partial a' \\ & + \int_{S_c} \mathbf{H}^t(\rho') \nabla G(\rho, \rho') \partial l' \end{aligned} \quad (33)$$

where the region V includes all permeable regions in the solution space, and S_c includes all conductive regions in this space. The 2-D Green’s function $G(\rho, \rho')$ is modified for the far field by

$$H_0^{(2)}(k\rho) \xrightarrow{\rho \rightarrow \infty} \sqrt{\frac{2j}{\pi k\rho}} e^{-jk\rho} \quad (34)$$

and the k values required for the image are introduced into the integral. The volume source integral methods have been implemented for both polarizations. Details concerning the implementation of this method are found in reference 12.

Finite Element Frequency Domain Image Examples

Example images are shown for the Electromagnetic Code Consortium (EMCC) 2-D Benchmark case 4. (See ref. 6.) The geometry and bistatic k -space images obtained from FEFD results for this case are shown in figure 15. The incident field is vertically polarized for this case and is impinging from the bottom. The minimum image contour is $-10 \text{ dB}\lambda$ with a 5-dB increment. The resolution is set to 1.5λ .

The images in figure 15 reveal that the primary scattering center in this geometry for scattering vertical polarization at these angles of incidence is the metallic wedge behind the three layers of low-loss dielectric. The low-loss dielectric does not attenuate any energy prior to impinging on the metallic wedge, but the image does show some diffraction from the dielectric layers. The magnitude of the backscatter from the wedge increases from 180° to 210° as one side of the wedge becomes more perpendicular to the incident wave.

MOM Computer Code Implementation of 5λ-Long End-Fed Antenna

The application of the bistatic k -space image technique for antenna method-of-moments (MOM) computer codes is implemented in exactly the same manner as for scattering. The only difference is that the right side voltage-forcing function now corresponds to localized port excitation on the body. (See refs. 2 and 7.) By specification of a localized feed point, amplitude, and phase, the resulting current distribution \mathbf{J} is computed. Then, just as in scattering cases, this current radiates a scattered field. A 1-D, 2-D, or 3-D image of the radiation produced by this current distribution in any specified spatial direction can be computed. The same image algorithms and subroutines used for scattering can also be used for antenna images.

Because the image resolution is typically 0.5λ or greater, the bistatic-imaging technique can produce useful diagnostic images for those antennas whose size is greater than the desired resolution. Thus, imaging multi-wavelength antennas is meaningful but imaging quarter-wavelength antennas may not be.

The example antenna image is that of a long-wire 5.0λ end-fed antenna shown schematically in figure 16. This antenna is a traveling-wave end-fire radiator whose maximum gain is produced near grazing at an angle $\theta_{TW, \max} \approx 49(\lambda/l)^{1/2} = 22^\circ$. The traveling-wave current produced by the end voltage excitation produces the main lobe. Then, if the end is not terminated in a matched load, this traveling-wave current is reflected and then proceeds to radiate a secondary end-fire lobe in the opposite direction. The radiation pattern for our end-fed 5.0λ antenna is shown in figure 17(a) for horizontal polarization. The maximum gain is almost 10 dBi (dB above isotropic) in the forward direction (158°) and 7 dBi for the reflected traveling-wave lobe in the back direction (22°).

Two-dimensional images for this antenna were computed for four resolutions from 0.5λ to 2.0λ in steps of 0.5λ and are shown in figure 17. The image angles were centered near the forward TW lobe at 160° , near the reflected TW lobe at 20° , on a forward intermediate side lobe at 120° , and on a rear side lobe at 60° . When the resolution is 1.0λ or greater, the following results were observed:

- As expected, the image forward traveling-wave scattering is greater than the reflected wave scattering.
- Traveling-wave radiation is produced over the length of the antenna with the peak amplitudes occurring near the feed end for the forward traveling wave and near the opposite end for the reflected wave.

- The side lobe radiation is produced from the ends of the antenna with the forward side lobe having greater amplitude than the rear side lobe. In each case the excitation end appears to produce the larger contribution.

Three-Dimensional Image Implementation Examples

The application of the bistatic k -space image technique to three dimensions is straightforward. The region in k space now becomes a volume, the image integral equation (9) is threefold; and the Fourier transform becomes three dimensional. Each dimension in filling the $E(\mathbf{k}^s)$ array is a loop over the corresponding $\mathbf{k}^s = (\mathbf{k}_{\text{down}}, \mathbf{k}_{\text{cross}}, \mathbf{k}_{\text{vol}})$ values. The FFT can then be computed with a multiple-dimension algorithm or can be done by rows, columns, and planes with a one-dimensional transform.

The real difficulty with three-dimensional images is not the computation of the image but the display of the resulting data. The approach taken for the examples in this study uses the marching-cubes algorithm in the Silicon Graphics Explorer Package. (See refs. 13 and 14.) The Explorer Package contains individual modules (i.e., precompiled subroutines with standard interfaces) which can be combined by the user for the various tasks required to create the image. The resulting FFT image data and geometry is read in the appropriate modules. The 3-D volumetric image data amplitude values are converted to user-specified isosurface levels (i.e., the equivalent of a single-value 2-D contour map). These isosurface levels are then viewed interactively from selected view angles.

Three-dimensional image for point targets. This example is a very simple array of point targets as shown in figure 18. Each point has an assigned spatial location and RCS value. This type of target is a very useful diagnostic for development of imaging software. The target array can be created to uniquely identify each spatial axis by variation of position and/or RCS level so that the resulting image coordinate system can be debugged. Each point target is independent of the others and scatters isotropically. The net RCS from a collection of N points is computed as the phasor sum

$$\sigma = \left(\sum_{i=1}^N \sqrt{\sigma_i} e^{j\mathbf{k}^{\text{inc}} \cdot \mathbf{r}_i} \right)^2 \quad (35)$$

where \mathbf{k}^{inc} is the wave-number vector (direction of incidence) and σ_i and \mathbf{r}_i are the RCS amplitude in m^2 and the spatial location, respectively, of the i th-point target.

The target array chosen for the 3-D image in figure 18 has four points: one at the origin with an

amplitude of 10 m^2 and one on each positive coordinate axis 1.0 m from the origin, each with an amplitude of 1 m^2 . For analytical purposes, the wavelength $\lambda = 1.0 \text{ m}$, the resolution $\Delta r = 0.25\lambda$, and the image volume extent was 4 m . The resulting FFT size was $16 \times 16 \times 16$. The excitation view angle \mathbf{k}^{scat} was set perpendicular to the plane of the three points on the coordinate axes and resulted in an elevation angle of 35° and an azimuth angle of 45° . The isosurface contour was set at -10 dB .

The resulting 3-D isosurface levels are shown in figure 18. The axis system and excitation vector are superimposed in figure 18 for clarity. Each of the three axis targets has the same magnitude, albeit smaller than the origin target because each was input with a smaller RCS value.

Three-dimensional image for parallel square plates. A pair of parallel 3.0λ -square plates 1.0λ apart has been imaged volumetrically in figure 19. The wavelength $\lambda = 1.0 \text{ m}$. In this example, a 2-D image overhead would not show the separate scattering centers of each plate because the two plates overlay each other. The illumination angles are edge-on to the plate at 0° and along the diagonal of the plate at 45° . The 3-D images are shown for horizontal polarization for two resolutions of 0.25λ and 0.5λ .

When viewed edge-on, the two leading edges of the plate are the dominant scattering centers due to parallel polarization edge diffraction and an edge traveling wave reflecting from the rear vertices. Because the plates are only 1.0λ apart, the 0.25λ resolution shows these scattering mechanisms more distinctly. Also, 3-D image results show a multiple-bounce scattering center appearing from the center of the plates that is probably due to the Keller cone bistatic radiation from each edge illuminating the opposite plate. This scattering mechanism is not apparent for the single plate in figure 5.

When viewed along the plate diagonals at 45° , the scattering mechanisms are the two edge waves reflected from the midvertices and a front vertex tip diffraction. In addition, longitudinal lines of multiple-scattering sources are shown on the plates. The origin for these is not certain; however, these sources may be due to the bistatic radiation from each of the two edge waves illuminating the opposite surface in and out of phase. Again, these mechanisms do not appear on the single plate in figure 5.

Three-dimensional image for sphere. A volumetric image for a resonant region sphere ($ka = 4$) is shown in figure 20. The sphere radius was $a = 0.637 \text{ m}$ and the wavelength $\lambda = 1.0 \text{ m}$. The image resolution was set at 0.25λ . The image was computed by the MOM3D com-

puter code. Polarization is vertical, and the isosurface level was set to -30 dB .

The image clearly shows the large front face reflection as the dominant scattering mechanism. The creeping waves, which spin around over the top and bottom for vertical polarization on the shadowed back side, are clearly evident. Compare these results with the 2-D images in figure 11. The 3-D images tend to be qualitative, whereas, 1-D and 2-D images are more quantitative.

Three-dimensional image for an airplane. The airplane geometry previously described has been imaged volumetrically in figure 21. The target was illuminated with horizontal polarization with nose-on incidence. The frequency was 6 GHz , and the resolution was set at 0.25λ . Induced body currents computed with the algorithm described in reference 15 cannot be seen in the black and white version of figure 21. The isosurface level was set to -40 dB .

The volumetric image shows the engine pods as being the dominant scattering centers for this illumination. This volumetric image corresponds to the 2-D image shown in figure 8.

Comparison of Analytical and Experimental Images

In this section the computational bistatic-imaging technique is compared with the experimental swept-frequency-angle-rotation image technique. The two techniques *are not* equivalent. While each approach produces images that are similar in many respects, important differences exist. In this section experimental image theory is reviewed, and then, results for the same geometry imaged with both techniques for downrange and downrange-cross-range are presented.

Experimental Theory

The experimental approach, discussed in reference 1, is a monostatic (backscatter) swept frequency measurement for downrange coupled with a target rotation for cross-range, i.e., an inverse synthetic aperture radar (ISAR) image. In two dimensions, the Fourier transform is on frequency and angle.

The derivation of the experimental image Fourier transform starts in the same manner as that used for the bistatic image. Equation (9) is written for 2-D images as

$$E(\mathbf{r}_{\text{down}}, \mathbf{r}_{\text{cross}}) = \iint W(\mathbf{k}) E(\mathbf{k}^e, \mathbf{k}^s = \{\mathbf{k}_{\text{down}}, \mathbf{k}_{\text{cross}}\}) \times e^{j(\mathbf{k}_{\text{down}} \cdot \mathbf{r} + \mathbf{k}_{\text{cross}} \cdot \mathbf{r})} dk_{\text{down}} dk_{\text{cross}} \quad (36)$$

The first step is to recognize that experimental images are backscatter monostatic amplitude and phase

measurements of the scattered field rather than bistatic. This means that the excitation of the target body will vary with illumination frequency and angular direction and that the distance \mathbf{r} in equation (36) is replaced with $2\mathbf{r}$ because a two-way path from transmitter to target and back to receiver is involved. For backscatter, the excitation and scattering directions are directly related to the incident excitation \mathbf{k}^{inc} :

$$\left. \begin{aligned} \mathbf{k}^e &= \mathbf{k}^{\text{inc}} \\ \mathbf{k}^s &= -\mathbf{k}^{\text{inc}} \end{aligned} \right\} \quad (37)$$

where the scattering direction is opposite of the excitation direction. The incident excitation is centered about the angular direction of the desired image shown in figure 22 and is a function of frequency and rotation angle:

$$\begin{aligned} \mathbf{k}^{\text{inc}} &= \frac{2\pi}{\lambda}(\hat{\mathbf{k}}_{\text{down}} \cos \theta, \hat{\mathbf{k}}_{\text{cross}} \sin \theta) \\ &= \frac{2\pi f}{c}(\hat{\mathbf{k}}_{\text{down}} \cos \theta, \hat{\mathbf{k}}_{\text{cross}} \sin \theta) \\ &= \frac{\omega}{c}(\hat{\mathbf{k}}_{\text{down}} \cos \theta, \hat{\mathbf{k}}_{\text{cross}} \sin \theta) \end{aligned} \quad (38)$$

Thus, the experimental variables become excitation frequency f and view angle θ . By sweeping the frequency and rotating the target, an annular circular arc region of k space is sampled by measurement of $E^s(f, \theta)$. Because this is a circular region, \mathbf{k}_{down} and $\mathbf{k}_{\text{cross}}$ are not independently sampled by (f, θ) , i.e., \mathbf{k}_{down} and $\mathbf{k}_{\text{cross}}$ both depend on (f, θ) . To associate downrange with only the frequency sweep and to associate cross-range with angle rotation, the small rotation angle approximation is introduced as in references 1 and 16 so that

$$\left. \begin{aligned} \cos \theta &\approx 1 \\ \sin \theta &\approx \theta \end{aligned} \right\} \quad (39)$$

With this approximation, the incident \mathbf{k} vector becomes

$$\mathbf{k}^{\text{inc}} \approx \frac{\omega}{c}(\hat{\mathbf{k}}_{\text{down}}, \theta \hat{\mathbf{k}}_{\text{cross}}) \quad (40)$$

so that the measured scattered field is sampled in k space as

$$E^s = E^s(\mathbf{k}^{\text{inc}} = k\hat{\mathbf{k}}_{\text{down}} + k\theta\hat{\mathbf{k}}_{\text{cross}}) \quad (41)$$

where $k = 2\pi/\lambda = 2\pi f/c = \omega/c$. Thus, \mathbf{k}_{down} is a function only of frequency, and for each frequency, $\mathbf{k}_{\text{cross}}$ is a function of angle. The image Fourier transform equation

(36) is reformulated to the Fourier transform equation in references 1 and 16:

$$E\left(t = \frac{2\mathbf{r}_{\text{down}}}{c}, \frac{2\mathbf{r}_{\text{cross}}}{\lambda}\right) = \int_{\theta_1}^{\theta_2} \int_{f_1}^{f_2} W(f, \theta) e^{j2\pi f t} df \times e^{j2\pi\left(\frac{2\mathbf{r}_{\text{cross}}}{\lambda}\right)\theta} d\theta \quad (42)$$

The downrange transform is time, or distance when time is multiplied by the speed of light c , while the cross-range transform is the rotation angle. The factor of 2 in the distance expression occurs because this is a two-way measurement from transmitter to target and then back to receiver.

By comparison of this approach with the bistatic image approach, the following differences are noted:

- The experimental image is backscatter.
- The transform domain is frequency and rotation angle, which results in the transform variables of time and cross-range.
- The experimental domain maps to a circular or polar region in k space. To prevent downrange–cross-range coupling, with resultant defocus and image smear, a small angle approximation must be made. Otherwise a focusing algorithm must be utilized.
- The measured scattered field which results from the target current distribution is a function of frequency and illumination angle; hence, the resulting image is a composite over the frequency bandwidth and angular rotation.

Bandwidth and Resolution

The experimental image resolution is proportional to bandwidth,

$$\Delta r_{\text{down}} = \frac{c}{2B} = \frac{\lambda}{2\Delta f/f} \quad (43)$$

where c is the velocity of light, B is the bandwidth, and $\Delta f/f$ is the fractional bandwidth. A 100-percent bandwidth, i.e., from $f = f_0/2$ to $3f_0/2$, is required for 0.5λ resolution.

Cross-range resolution is (ref. 1)

$$\Delta r_{\text{cross}} = \frac{\lambda}{4 \sin(\Delta\theta/2)} \approx \frac{\lambda}{2\Delta\theta} \quad (44)$$

The bistatic k -space bandwidth is twice the equivalent experimental bandwidth for the same resolution. This can be shown by equating the fundamental Fourier transform pair variables as

$$\Delta r \Delta k = \Delta \omega \Delta t = 2\pi \quad (45)$$

The time delay is $\Delta t = 2\Delta r/c$; for equivalent resolutions Δr , Δr can be canceled. Thus, the bistatic k -space bandwidth must be twice the experimental frequency bandwidth for equivalent resolutions:

$$\Delta k = 2\left(\frac{\Delta\omega}{c}\right) \quad (46)$$

For 0.5λ resolution, the experimental frequency sweep must be $\Delta f/f_0 = 1$, so that the illumination frequency is bounded by

$$0.5f_0 \leq f \leq 1.5f_0 \quad (47)$$

For the equivalent 0.5λ resolution bistatic case, the k -space bandwidth is $\Delta k = 4\pi/\lambda_0 = 2k_0$. In downrange k_r is centered on $k_0 = 2\pi/\lambda_0$; hence, k_r is bounded by

$$0 \leq k_r \leq 2k_0 \quad (48)$$

Because of the swept frequencies in the experimental image, the downrange information has a time delay, i.e., frequency and time are a Fourier transform pair. This results in scattering mechanisms, which are delayed in time, being imaged farther downrange. Thus, multiple-bounce mechanisms will often image past the end of the body. For cavities imaged at an angle, the downrange–cross-range image will show the rear cavity return at the downrange location with a cross-range at the location of the cavity opening.

Traveling-wave current radiation is not imaged at the source but at the geometric reflection point because of the swept frequency nature of the experimental image. This phenomenon occurs because the image average over frequency phase cancels. The only stationary phase point is the geometric reflection point on the body.

Some of the scattering issues and comments on how the computational k -space bistatic approach and the experimental approach differ are listed in table I.

Experimental and Bistatic k -Space Images

In this section 1-D downrange and 2-D downrange–cross-range-measured images are presented for comparison with bistatic k -space images. The target is a 6-in.- (0.15-m-) square plate viewed from three aspect angles: normal to the plate, edge-on at 10° elevation, and at 45° azimuth along the diagonal at 10° elevation. The nominal illumination frequency is 10 GHz with $\lambda = 1.18$ in. (0.03 m).

When images are compared, particularly 2-D images, the same window weight function and resolutions should be used. In our examples the Hanning window was utilized, and three resolutions for the computed images are presented. The amplitude and distance data

scales are identical for both the experimental and computed images. However, note that on the 1-D experimental images, the downrange distance is 0.5 m at a downrange location of 0.3 to 0.8 m.

Experimental parameters. The square plate was imaged utilizing a compact range with a center frequency of 10 GHz and a frequency bandwidth of 4 GHz, from 8 to 12 GHz. The resulting downrange resolution was, from equation (43), $1.25\lambda = 1.47$ in. = 0.0375 m. The angular illumination sweep was $\Delta\theta = 20^\circ$.

Computational parameters. The square plate bistatic k -space images were computed by MOM3D. (See ref. 2.) The mesh model had 5000 triangles, which result in 7400 unknowns. The geometry symmetry option was utilized so that the system matrix was decomposed into two smaller matrices of 3725 and 3675 unknowns each. The sample density was 286 unknowns per square wavelength. The image extent was set to 0.5 m and the window weight function was Hanning. Three resolutions of 0.5λ , 1.0λ , and 1.5λ or 0.015, 0.030, and 0.045 m, respectively were computed.

Image comparisons. View 1 is perpendicular to the plate shown in figure 23 for 1-D and 2-D images for horizontal polarization (vertical polarization is not shown because the results are the same). The dominant scattering for this case is specular with a peak RCS of $\sigma_{\text{specular}} = 4\pi A^2/\lambda^2 = 7.6 \text{ m}^2 = 8.8 \text{ dBsm}$ as shown in the experimental and computed 1-D images. For the 2-D images, the backscattered radiation is coming uniformly from the entire plate. For the computed images, the coarser resolutions smear the image over a larger spatial region. For the 1-D images, the peak RCS stays constant with resolution. For 2-D images the peak RCS varies from 3.5, 0, and -5 dBsm for resolution equal to 1.5λ , 1.0λ , and 0.5λ , respectively. This is one reason why the same resolution should be used when image comparisons are made. The experimental image shows a lower level source, which is probably due to edge-to-edge diffraction and is sometimes called “talking edges,” emanating from behind the plate. This return is categorized as a multiple bounce and images later in time downrange of the plate. This effect is not apparent in the computed images. Residual signal-processing side lobes are shown in the computed 1-D and 2-D images.

View 2 is normal to the plate edges (Azimuth = 0°) at an elevation angle of 10° horizontal polarization as shown in figure 24. The dominant scattering is due to leading-edge diffraction in this polarization. For vertical polarization, the trailing edge is the dominant scatterer because of traveling-wave reflection as shown in figure 25.

The images with horizontal polarization (fig. 24(a)) show the leading edge as the dominant scattering mechanism along with two edge waves reflecting from the rear vertices. The leading-edge return for the 1-D images (fig. 24(b)) is close to the theoretical knife-edge value of $\sigma_{\text{edge}} = l^2/\pi = 0.00074 \text{ m}^2 = -21.3 \text{ dBsm}$. The experimental image also shows a scattering center behind the plate that is due to rear corner-to-corner diffraction, which arrives later in time. The edge wave mechanism in the computed images shows a spatial distribution with a peak at the rear vertex. This distribution can be interpreted as the edge wave, which upon reflection loses energy from radiation as it travels back toward the front corner. Thus, a decaying intensity of the image is observed. The computed coarser resolution images smear the return over a larger spatial extent.

The vertical polarization images (fig. 25(a)) show the trailing edge as the dominant scattering mechanism. The experimental image also shows a scattering center behind the plate that is due to a second-bounce surface wave, i.e., from the rear edge to the front and a second reflection from the back edge. This wave arrives later in time and experimentally images behind the plate. This scattering center is not present in the computed images. The trailing-edge return from the 1-D images (fig. 25(b)) is much less than the theoretical knife-edge value of $\sigma_{\text{edge}} = l^2/\pi = 0.00074 \text{ m}^2 = -21.3 \text{ dBsm}$. The view angle for this case is much less than the elevation angle for a maximum traveling-wave return that would occur at an excitation elevation angle $\theta_{\text{TW}} = 49(\lambda/l)^{1/2} = 22^\circ$. As before, the computed coarser resolution images smear the return over a larger spatial extent.

The experimental vertical polarization images (fig. 25(a)) suggest a scattering mechanism from the front edge of the plate, which is not observed in the computed images. This scattering is hypothesized to be due to the trailing-edge-reflected surface wave, and that if the plate were electrically longer, the leading-edge scattering would not be seen. The computed images do not show a leading-edge scattering center. The dominant mechanism for this viewing angle is the trailing-edge traveling-wave reflection. In the computed 1-D and 2-D images, the peak occurs at the rear and decays toward the front of the plate. This corresponds to the interpretation that the traveling wave, upon reflection, loses energy from radiation as it travels back toward the front edge. Thus, the image decays in intensity. This phenomenon is not observed in the experimental data because the swept frequency nature of the image causes the stationary phase locations to coincide with the edges of the plate. The leading-edge return in the experimental images is interpreted as the trailing-edge-reflected surface wave, which has not completely decayed by the time it reached the front. This phenomenon is known to occur because the multiple-

bounce traveling wave arrives later in time. Because the traveling-wave mechanism images differently for the computed and experimental approaches, the magnitudes of high peaks are not the same.

View 3 is along the plate diagonal, at an azimuth angle of 45° , and at an elevation angle of 10° as shown in figures 26 and 27 for horizontal (parallel) and vertical (perpendicular) polarizations, respectively. The dominant mechanisms are nonspecular edge and traveling waves.

The horizontal polarized images (fig. 26(a)) show scattering from the four tips of the plate. The two dominant tips are the midvertices, which reflect the edge traveling wave. The 1.0λ - and 0.5λ -resolution images show these reflected edge waves on the two front-illuminated edges with the peak amplitudes near the reflection point. The rear vertex scattering center is probably due to edge waves which *turned the first corner* and then reflected from the rearmost vertex and/or to tip diffraction because the plate is viewed at an elevation of 10° . The front tip return has the lower magnitude due to tip diffraction.

The experimental images show the front vertex with a lower amplitude than the rear. The opposite occurs in the computed images. The reason for this difference is not clear. Possibly, the measured front tip image is the phasor sum of tip diffraction and the remainder of the reflected edge wave, which are phase subtracting to produce a smaller return.

The vertical polarization images (fig. 27(a)) show scattering from the rear vertex, which is due to the reflected surface traveling wave. As before with traveling-wave mechanisms, the experimental and computed image magnitudes differ. The computed results show a lower amplitude spatially distributed return, while the experimental image shows a higher amplitude return localized to the rear vertex. The computed images show the maximum amplitude near the aft reflection point with the reflected traveling wave decreasing in intensity as it propagates toward the front. The 1-D-measured image shows a small return from the front tip, which may be the stationary phase residual of the reflected traveling wave. The view angle in elevation is less than the angle of approximately 18° for maximum surface wave reflection that would occur with the plate diagonal length.

Comparison of the experimental images with the bistatic k -space images shows the following:

- Scattering mechanisms that are localized produce similar images. The experimental and computed images are similar in most respects for specular and leading-edge scattering. For trailing-edge diffraction images may be

similar; however, this comparison has not been made for a truly large target many wavelengths in size.

- Multiple-bounce scattering mechanisms image differently. The experimental images show multiple reflections farther downrange because of a time-delay mechanism. This agrees with the physical view. The bistatic k -space approach images the current distribution, which, by definition, exists only on the surface and, thus, cannot be farther downrange. The computed images show multiple-bounce mechanisms as locations on the body where those current mechanisms exist, i.e., placement of radar-absorbing material at these locations would reduce the scattering.
- Surface traveling waves and edge waves image differently. The computed images tend to show edge and traveling waves as distributed sources over the scattering surfaces, which corresponds to physical intuition for this mechanism. The swept-frequency-measured images show these mechanisms at the body fore and aft end point locations. In this case the bistatic images more closely resemble the physical interpretation.

Summary Remarks

A bistatic k -space analytical imaging technique has been introduced which allows diagnostic images to be inexpensively computed from a single-body current distribution. A significant reduction in computational processing is obtained because a frequency sweep over a short-pulse bandwidth is not required.

Images permit physical insight and understanding into how a radiation or scattering pattern is produced by decomposing the resultant radiation into contributions from localized scattering centers or hot spots. Knowledge of these hot spots permits a user to understand and modify the structure to obtain desired features.

The costs associated with computation of bistatic images are usually small compared with the effort required to obtain the current distribution. From the currents, the bistatic k -space fields are computed with the generalized radiation integral. This is similar to the effort required to compute a radiation pattern. The computed k -space $E(\mathbf{k})$ fields are then Fourier transformed to obtain the spatial image.

The bistatic k -space technique can be applied to both antenna and scattering problems. It can be used with any frequency domain computer algorithm that produces a current distribution on the geometric structure. The technique may be used with computer codes such as method of moments, finite element frequency domain, and physical optics. Images may be computed in one, two, or three dimensions typically corresponding to downrange, downrange-cross-range, and volumetric images, respectively.

The k -space scattered fields are computed on an orthogonal grid in k space corresponding to $(\mathbf{k}_{\text{down}}, \mathbf{k}_{\text{cross}}, \mathbf{k}_{\text{vol}})$. These are independent and, thus, eliminate image-smearing problems commonly associated with circular arc ISAR experimental images.

Bistatic k -space images are not the same as those produced by the sweep frequency experimental approach. Some contrasts are listed as follows:

- Specular scattering mechanisms image similarly.
- Traveling-wave-distributed radiation sources image along the current source rather than at the experimental stationary phase end points.
- Multiple-bounce time-delay mechanisms image at the body locations responsible for scattering.
- Bistatic images are formed from currents caused by a single frequency and a single-excitation angle.
- Experimental backscatter images are formed from currents caused by a bandwidth of frequencies and multiple excitation angles.

Several EM computer code applications have been shown, and an implementation approach was given for each. Implementation is not difficult because most computer codes already have subroutines that utilize the normal radiation integral. The radiation subroutines need only to be generalized to compute arbitrary points in k space rather than to use $\mathbf{k}^{\text{radial}}$ as a function of angle.

NASA Langley Research Center
Hampton, VA 23681-0001
March 1, 1996

Appendix

Image Issues

The following image topics are reviewed:

- Resolution and bandwidth
- Dynamic resolution improvement with windowing
- Signal-processing gain
- Data smoothing
- Distributed image amplitude levels
- Image units

Resolution and Bandwidth

Resolution is the ability to distinguish the separation between two adjacent scattering centers. The following two cases arise: (1) when the two scattering centers have the same amplitude and (2) when they do not. Resolution is inversely related to bandwidth B , i.e., greater bandwidth is required for greater resolution (smaller Δr). In the monostatic case, resolution in downrange is

$$\Delta r = \frac{c}{2B}$$

which can be rewritten in terms of fractional bandwidth:

$$\Delta r = \frac{c}{2B} = \frac{\lambda}{2\Delta f/f_c}$$

This relationship is derived from the maximum change in phase that can occur without aliasing. With the FFT process to transform the frequency data (far field) to range data (near field), resolution is the peak-to-null distance or the FFT half period.

Cross-range-imaging resolution is obtained by rotational bandwidth $\Delta\phi$. This is achieved either by rotating the target (inverse synthetic aperture radar (ISAR)), or by rotating the radar about the target (synthetic aperture radar (SAR)). The cross-range resolution is

$$\Delta r = \frac{\lambda}{2 \sin(\Delta\phi)}$$

This relationship can also be derived from the maximum change in phase that can occur without aliasing.

For example, at X band with a center frequency of 10 GHz and a bandwidth of 4 GHz (8 to 12 GHz), the fractional bandwidth is 0.4 for a resultant resolution of $\Delta r = (1.18/2)(1/0.4) = 1.475$ in. (See fig. A1.) In this figure the target is a point scatterer with an amplitude of $1 \text{ m}^2 = 0 \text{ dBsm}$. For the cross-range image to have the same resolution, the angular bandwidth (rotation) would be 23° .

Two equal-amplitude 1-m^2 point targets spaced one resolution cell apart can be compared in figure A2. The first scatterer is at the origin and the second is placed $\Delta r = c/2B = 1.475$ in. farther downrange. The image for a rectangular window function shows an error of 1.0 dB in amplitude and a shift error in position. This is caused by the close proximity of the two targets. By placement of the two point targets two resolutions cells apart at $\Delta r = 2(1.475) = 2.95$ in., figure A3 shows a reduction of the image amplitude error to 0.7 dB and also reduces the position error.

When adjacent scattering centers do not have equal magnitudes, the smaller target can become buried in the side lobes of the higher-amplitude scatterer. To resolve closely spaced unequal targets, dynamic resolution with the use of windowing functions is required.

Dynamic Resolution Improvement With Windowing

When adjacent scattering centers have unequal magnitude, the smaller scattering center can be lost in the image side lobes of the larger scattering center. Improved dynamic resolution can be obtained with an aperture-shaping–weighting function (or windowing function) on the image data before the Fourier transform to reduce the processing side lobes. This enhancement is obtained at the cost of poorer range resolution. The intrinsic window in the transformation is a rectangular window.

A nonrectangular window function makes resolving capabilities worse for equal-magnitude scatterers. The resolution is made poorer by the ratio of the area under the rectangular window divided by the area under the nonrectangular window function. This ratio defines the reciprocal of the window gain ($W_g < 1$).

$$\Delta r_{\text{effective}} = \Delta r \left[\frac{\int \text{Rectangular window}}{\int \text{Window function used}} \right] = \frac{\Delta r}{W_g}$$

A cosine (Hanning) window has side lobes which are down 31.5 dB; hence, the dynamic resolution or the ability to image lower level nearby scattering centers is made worse when compared with a rectangular window, which has its first side lobe down 13 dB. With the Hanning window the effective resolution is poorer by a factor of 2. A rectangular window is typically used to resolve closely spaced approximately equal amplitude scatters, whereas, a nonrectangular window is used to resolve widely spaced scatterers having significantly different amplitudes.

Signal-Processing Gain

The signal-to-noise ratio determines the lowest signal that can be recognized in its coherent form. Image Fourier transforms of N points produce a net gain in the signal-to-noise ratio because of the integration differences between coherent and noncoherent signals in the original data. This effect is called processing gain. Scattering centers add coherently ($\propto N^2$), while noise adds incoherently ($\propto N$). The net signal-processing gain in dB is the ratio of these two:

$$\left(\frac{\text{Signal}}{\text{Noise}}\right)_{\text{gain in dB}} = 10 \log_{10}\left(\frac{N^2}{N}\right) = 10 \log_{10} N$$

A 16-point data set would yield a Fourier transform signal-processing gain of 12 dB in signal-to-noise while a 32-point transform would have a 15-dB gain, a 3-dB improvement from doubling the number of points.

However, the signal-to-noise ratio is reduced when a windowing function is used. This is due to less energy being incorporated into the overall transform (area under the window). Now

$$\left(\frac{\text{Signal}}{\text{Noise}}\right)_{\text{gain in dB}} = 10 \log_{10}\left[\frac{(N \cdot W_g)^2}{(N \cdot W_g)}\right] = 10 \log_{10}(N \cdot W_g)$$

Data Smoothing

Smoothing the data processed by the Fourier transform is accomplished by addition of zeros to either end of the data set thereby increasing the size N of the transform. This affects only the sampling of the resultant transformation by making it finer but has no effect on either the range or dynamic resolution. Because of finer sampling, higher-precision position and level are obtained at the expense of making the transformation size larger.

For example, a 16-point transformation of 300-MHz bandwidth would yield an 0.5-m step size. (See fig. A4.) By zero padding the data set by a factor of 4 (a transformation of 64 points) the resultant step size would be 0.125 m, which results in the smoother image in figure A5. The smoothing benefit becomes minimal after a few factors of zero padding have been applied because of the resultant transform being highly sampled.

Distributed Image Amplitude Levels

A target with a distributed image is one where the coherent RCS is formed from the coherent elemental addition from an extended spatial region on the target. Examples are: (1) a surface-viewed specular where the coherent RCS is the phase sum from the entire constant-

phase specular region and (2) a traveling-wave source viewed at the angle for which the elemental current sources add in phase.

A two-dimensional image of a flat-plate-viewed specular produces an almost uniform image distributed over the perpendicular plate dimension. The amplitude level of this distributed image is not the plate coherent level. Rather it becomes a function of the effective resolution and coherent length.

If the effective resolution Δr_{eff} is greater than the coherent length l_c , then the image amplitude is just the total coherent sum within the resolution cell. When the resolution cell Δr_{eff} is less than the spatial coherent length l_c , the image amplitude is decreased because only the constant-phase region within the resolution cell can contribute to the image (power) magnitude. Thus, the distributed amplitude is smaller than the coherent amplitude by the square of the ratio

$$(\text{Distributed amplitude}) = (\text{Coherent amplitude}) \left(\frac{\Delta r_{\text{eff}}}{l_c}\right)^2 \quad (\Delta r_{\text{eff}} < l_c)$$

Thus, the distributed image amplitude is decreased as the effective resolution Δr_{eff} becomes smaller. Expressed in dB reduction, this becomes

$$(\text{Amplitude reduction})_{\text{dB}} = 20 \log_{10}\left(\frac{\Delta r_{\text{eff}}}{l_c}\right)$$

For example, image a 1-m-square plate at 300 MHz ($\lambda = 1$ m). The coherent specular flash is $\sigma = 4\pi A^2/\lambda^2 = 11$ dBsm. A downrange image normal to this plate would produce an image amplitude equal to the coherent level of 11 dBsm because the coherent length of the plate in the downrange direction is nominally zero.

However, a two-dimensional image normal to the plate becomes a distributed image over the 1-m width of the plate. If the bandwidth is assumed to produce an image resolution of 0.1 m and a cosine (Hanning) window function is utilized, the effective resolution is $\Delta r_{\text{eff}} = 0.2$ m. The two-dimensional image amplitude over the plate would be decreased by $20 \log(0.2/1.0) = -14$ dB. Thus, the two-dimensional image of this plate would have a magnitude of $11 \text{ dB} - 14 \text{ dB} = -3 \text{ dB}$ over the 1-m plate width.

Image Units

Radar cross section units are that of area, typically in square meters. In decibel or log space, the reference is 1 m^2 , which results in units of dBsm. However, images do not have the same units as coherent radar cross section.

Downrange images present scattering power amplitudes versus downrange distance of cross section per unit distance (σ/m). Hence, downrange images have amplitude units of σ/m versus distance or decibel units of $\log(\sigma/m) = \log(m^2/m) = \log(m) = \text{dBm}$.

Two-dimensional downrange–cross-range images present scattering power amplitudes versus area of cross section per unit area (σ/m^2). This area image has amplitude units of σ/m^2 versus downrange–cross-range. In decibels units, this becomes $\log(\sigma/m^2) = \log(m^2/m^2) = \log(1) = \text{dB}$.

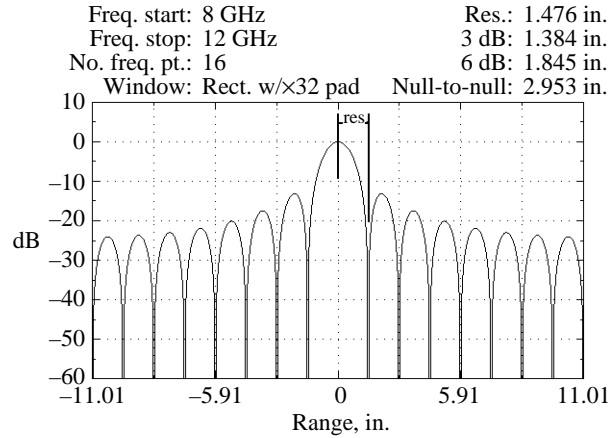


Figure A1. A 4-GHz bandwidth image showing a resolution of 1.475 in. from peak to null.

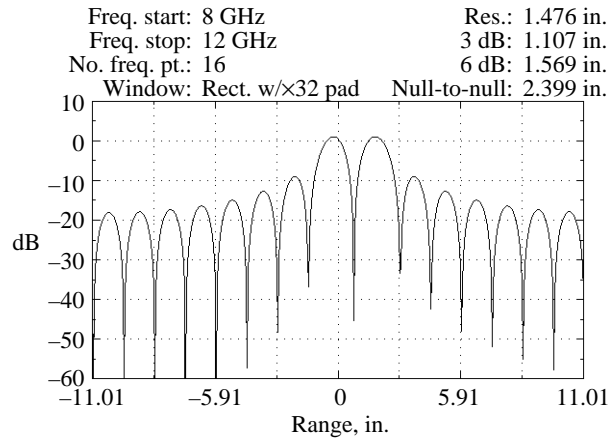


Figure A2. Two equal targets one resolution cell apart causing 1-dB amplitude error.

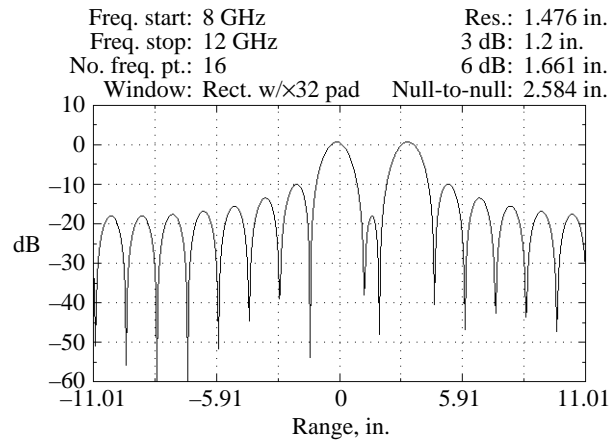


Figure A3. Two equal targets two resolution cells apart causing 0.7-dB amplitude error.

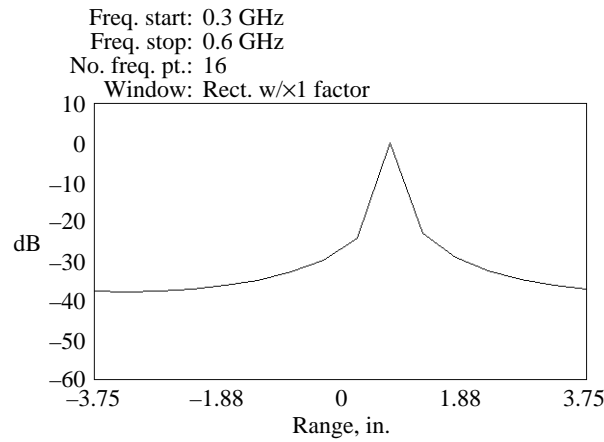


Figure A4. Data smoothed with 16-point FFT; 1-m² target.

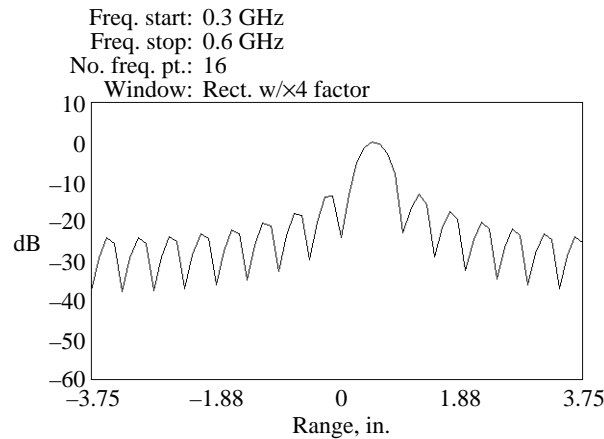


Figure A5. Data smoothed with 64-point FFT; 1-m² target.

References

1. Mensa, Dean L.: *High Resolution Radar Cross-Section Imaging*. Artech House, 1991.
2. Shaeffer, John F.: *MOM3D Method of Moments Code Theory Manual*. NASA CR-189594, 1992.
3. Knott, E. F.; Shaeffer, J. F.; and Tuley, M. T.: *Radar Cross Section: Its Prediction Measurement and Reduction*. Artech House, 1985.
4. Bhalla, R.; and Ling, H.: ISAR Image Formation Using Bistatic Data Computed From the Shooting and Bouncing Ray Technique. *J. Electromagn. Waves & Appl.*, vol. 7, no. 9, 1993, pp. 1271–1288.
5. Brigham, E. Oran: *The Fast Fourier Transform*. Prentice-Hall, Inc., 1974.
6. 2-D Benchmark Codes Subgroup Joint Services Electromagnetic Code Consortium: *Two-Dimensional Benchmark Problems for RCS Predictions—Tabulation of Results*. EMCC, Jan. 1990.
7. Harrington, Roger F., ed.: *Field Computation by Moment Methods*. Macmillan Co., 1968.
8. Woo, Alex C.; Wang, Helen T. G.; Schuh, Michael J.; and Sanders, Michael L.: Benchmark Radar Targets for the Validation of Computational Electromagnetics Programs. *IEEE Antennas & Propag. Mag.*, vol. 35, no. 1, Feb. 1993, pp. 84–86.
9. Shaeffer, John F.: *Combined Body of Revolution and Patch Moment Code—Theory Report*. NASA CR-194988, 1994.
10. Johnson, Stuart K.: *Convergence Characteristics of a Numerical Integration Technique for Solving the Physical Optics Equations*. NASA TM-4052, 1988.
11. Baucke, R. C.; D'Angelo, J.; and Crabtree, G. D.: Far-Field Transforms for Finite Element Frequency-Domain Solutions. *IEEE Trans. Antennas & Propag.*, vol. 41, no. 4, Apr. 1993, pp. 511–514.
12. Baucke, R. Craig; and D'Angelo, John: Numerical Imaging of Finite Element Frequency Domain Solutions. *9th Annual Review of Progress in Applied Computational Electromagnetics at the Naval Postgraduate School*, Mar. 1993, pp. 182–188.
13. *IRIS Explorer User's Guide*. Silicon Graphics, Inc., 1991.
14. Lorensen, William E.; and Cline, Harvey E.: Marching Cubes: A High Resolution 3D Surface Construction Algorithm. *Comp. Graph.*, vol. 21, no. 4, July 1987, pp. 163–169.
15. Hom, Kam W.: *EM-ANIMATE—A Computer Program for Displaying and Animating Electromagnetic Near-Field and Surface-Current Solutions*. NASA TM-4539, 1994.
16. Currie, Nicholas C., ed.: *Radar Reflectivity Measurement: Techniques & Applications*. Artech House, 1989.

Table I. Bistatic k -Space Image Issues Compared With Experimental Approach

Issue	Bistatic k -space images	Experimental images
Origin of scattered field	Bistatic scattered fields	Monostatic (backscatter) fields
Transform domain	Directly in k space	Frequency for downrange; angle for cross-range
Fourier transform variables	Wave number k and position r , kr	Frequency and time ωt for downrange and $kr\theta$ for cross-range
Target excitation currents (what the image represents)	Only at frequency and illumination angle of excitation	Varies over the excitation frequency and illumination angle
Focus/image smear	None because image is computed directly in k space on an orthogonal grid of uniformly spaced points	Rotation angle limited to small angle without use of focusing algorithms. Inherently a circular region in transform space
Resolution	$\approx \lambda/2$ limited only by granularity of current representation; typically, $\approx \lambda/10$ requires twice the experimental bandwidth	Set by available frequency bandwidth and small rotation angle approximation
Time-delayed multiple bounce	Images currents which radiate in direction of image	Images downrange as time delay. Hence, delayed in time
1-D images	Downrange (radial) in k space	Frequency sweep
2-D images	Add cross-range in k space	Add rotation angle
3-D images	Add perpendicular direction in k space	Add measurements over orthogonal plane
Fidelity for distributed current radiation (traveling waves)	Images the radiation as a distributed source	Because of frequency sweep, images the end points of distributed source
Antenna images	Straightforward application	Not done
Image in direction other than excitation, i.e., bistatic images	Straightforward application	Very difficult, seldom done
Cross-polarized image	Straightforward application	If separate transmit and receive feeds, rotate one feed
Geometry knowledge	Needed for analytics	Not needed
Target identification	No	Yes

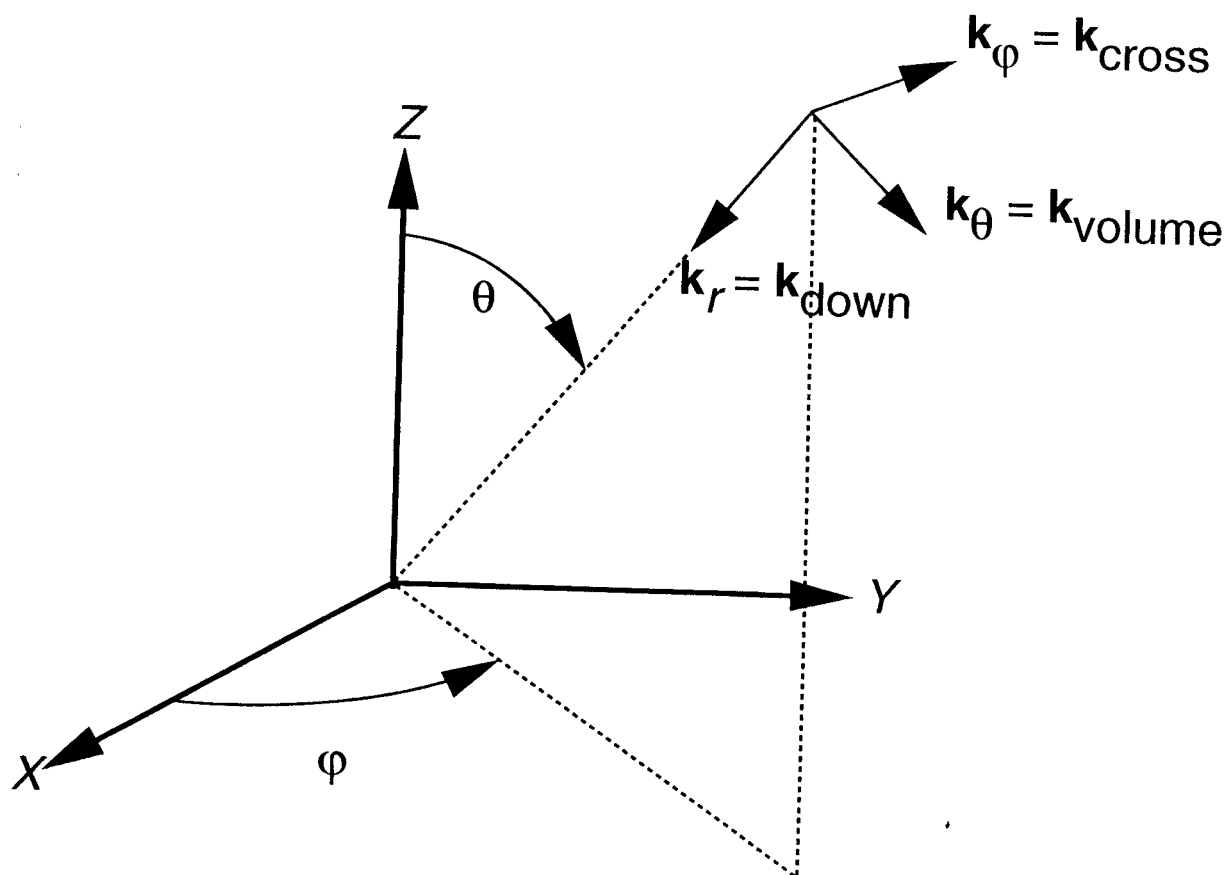


Figure 1. Bistatic k -space image coordinate system.

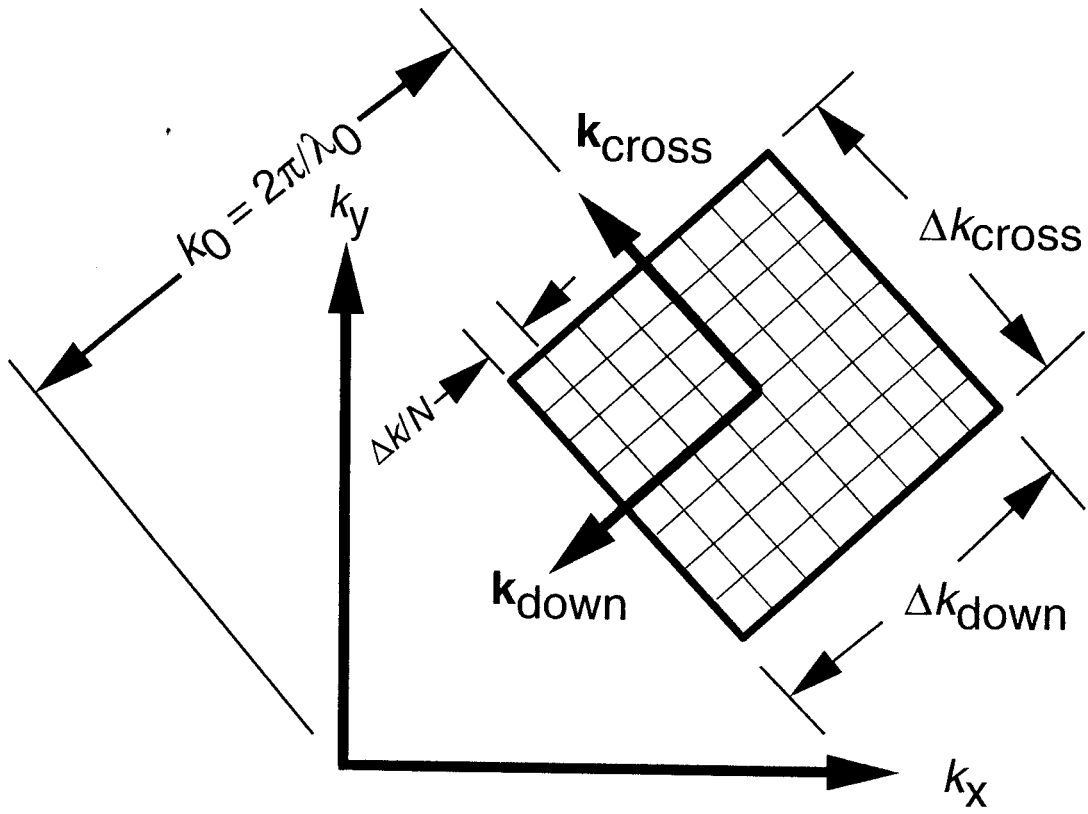


Figure 2. Computational domain for bistatic k -space images.

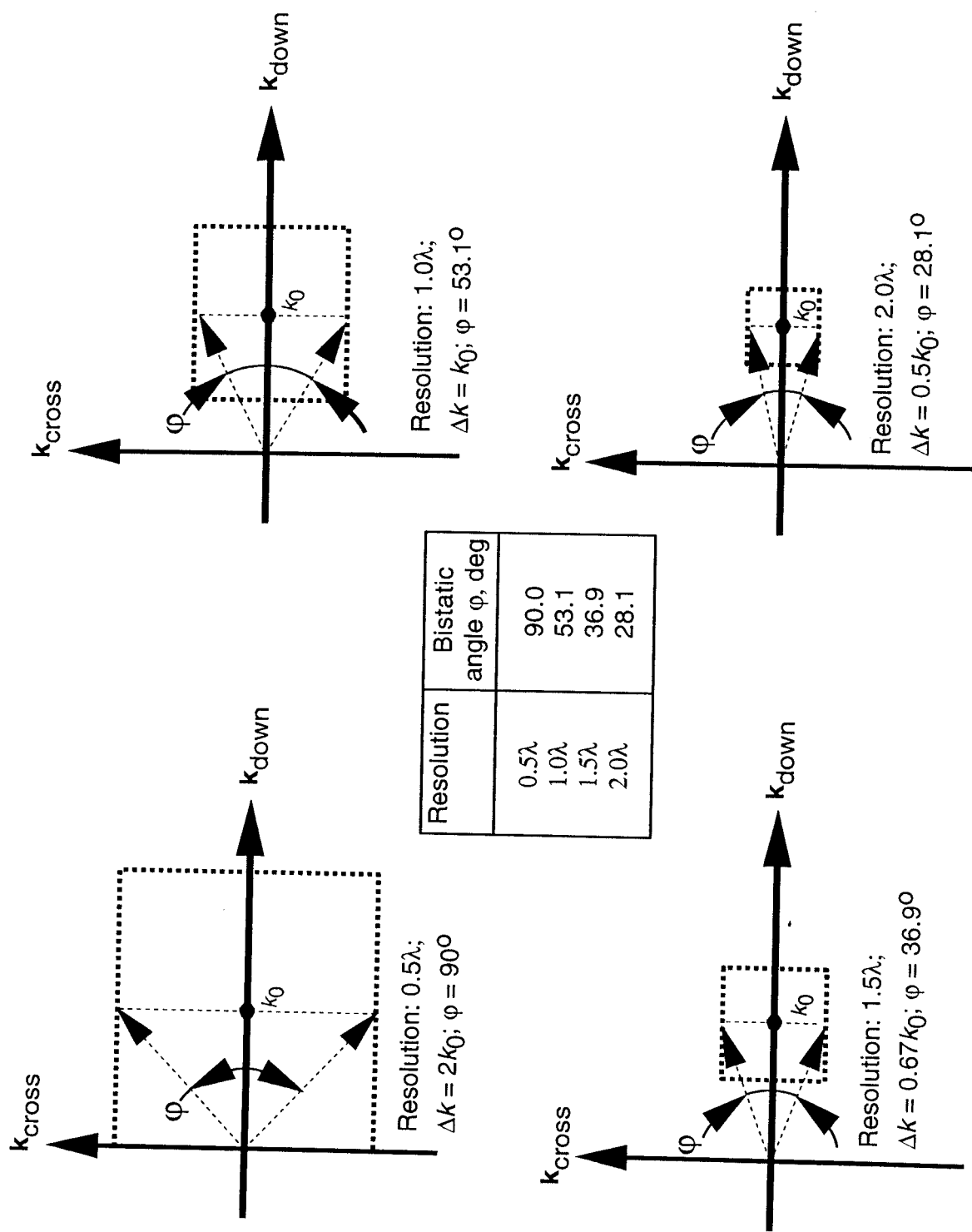
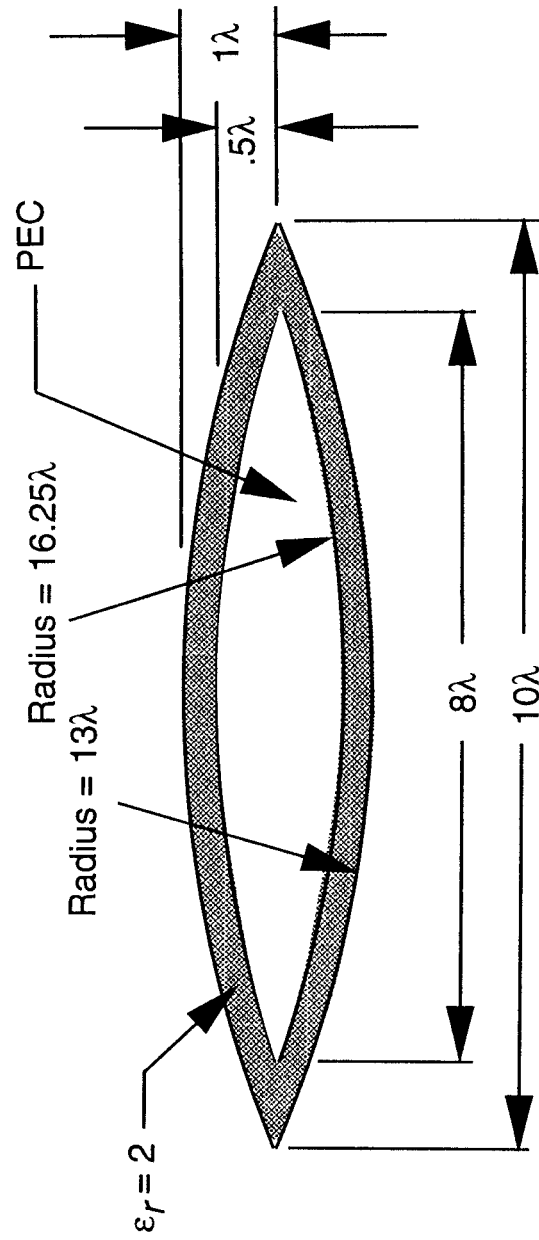
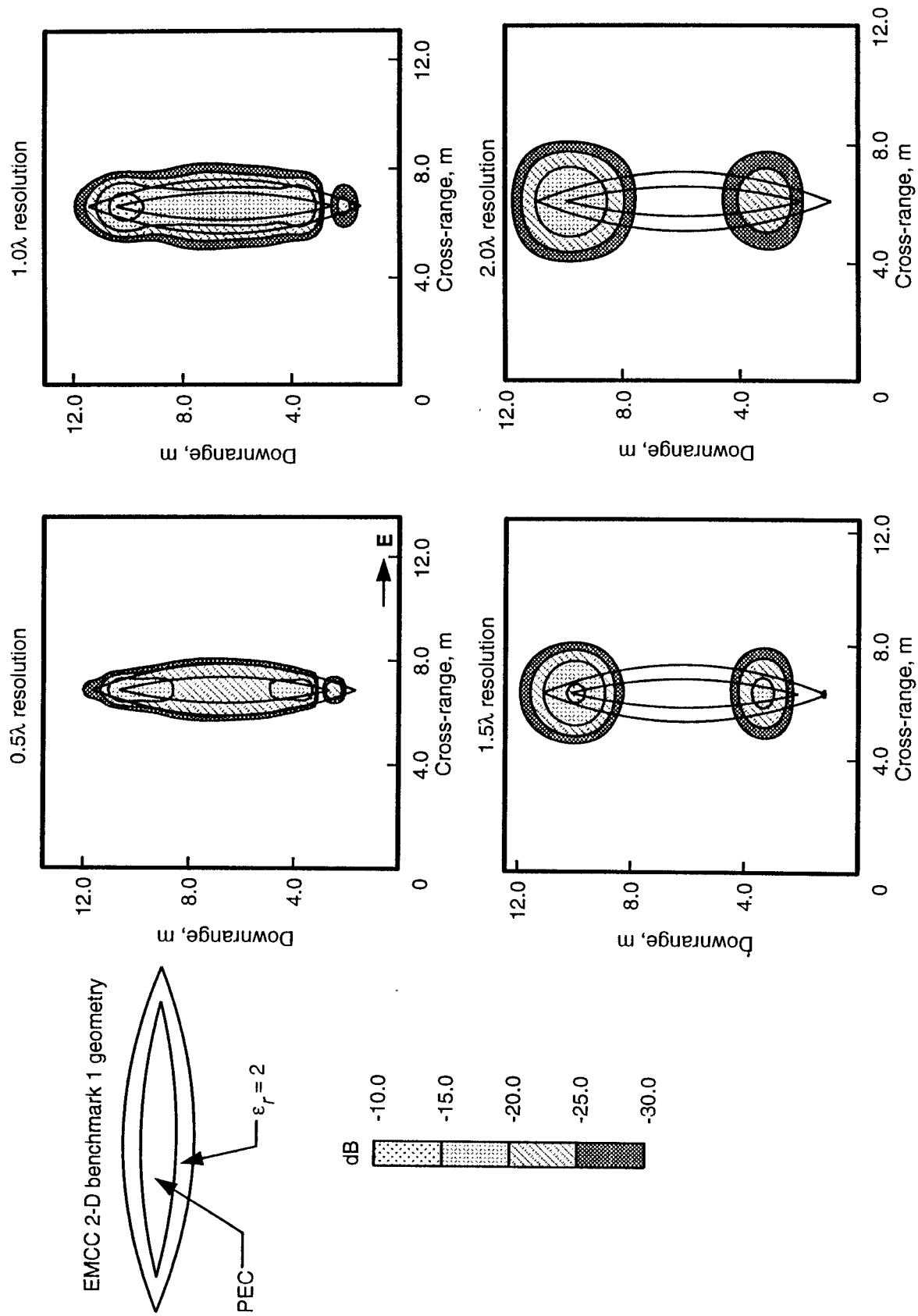


Figure 3. Bistatic k -space computational regions for 0.5λ , 1.0λ , 1.5λ , and 2.0λ resolutions. (Bistatic angle φ is included angle in azimuthal plane.)



(a) EMCC benchmark geometry description. Linear dimensions are in wavelengths.

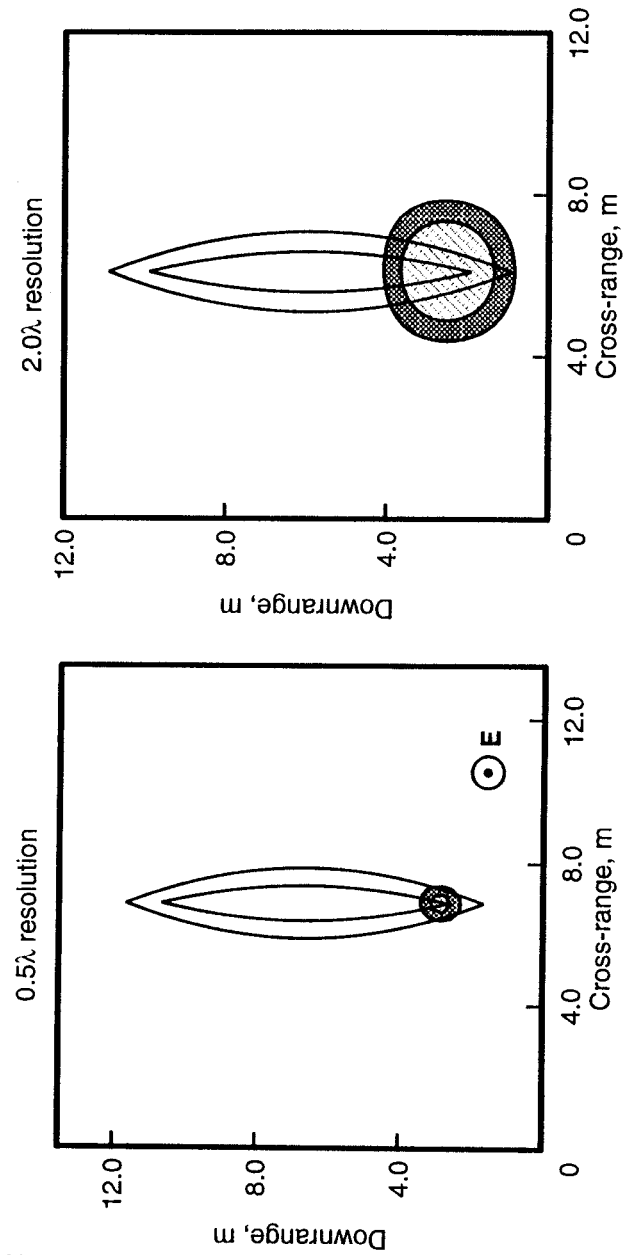
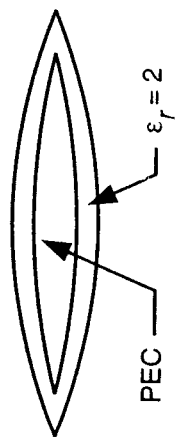
Figure 4. Resolution study for EMCC 2-D ogive benchmark geometry. Frequency = 0.3 GHz.



(b) Horizontal polarization.

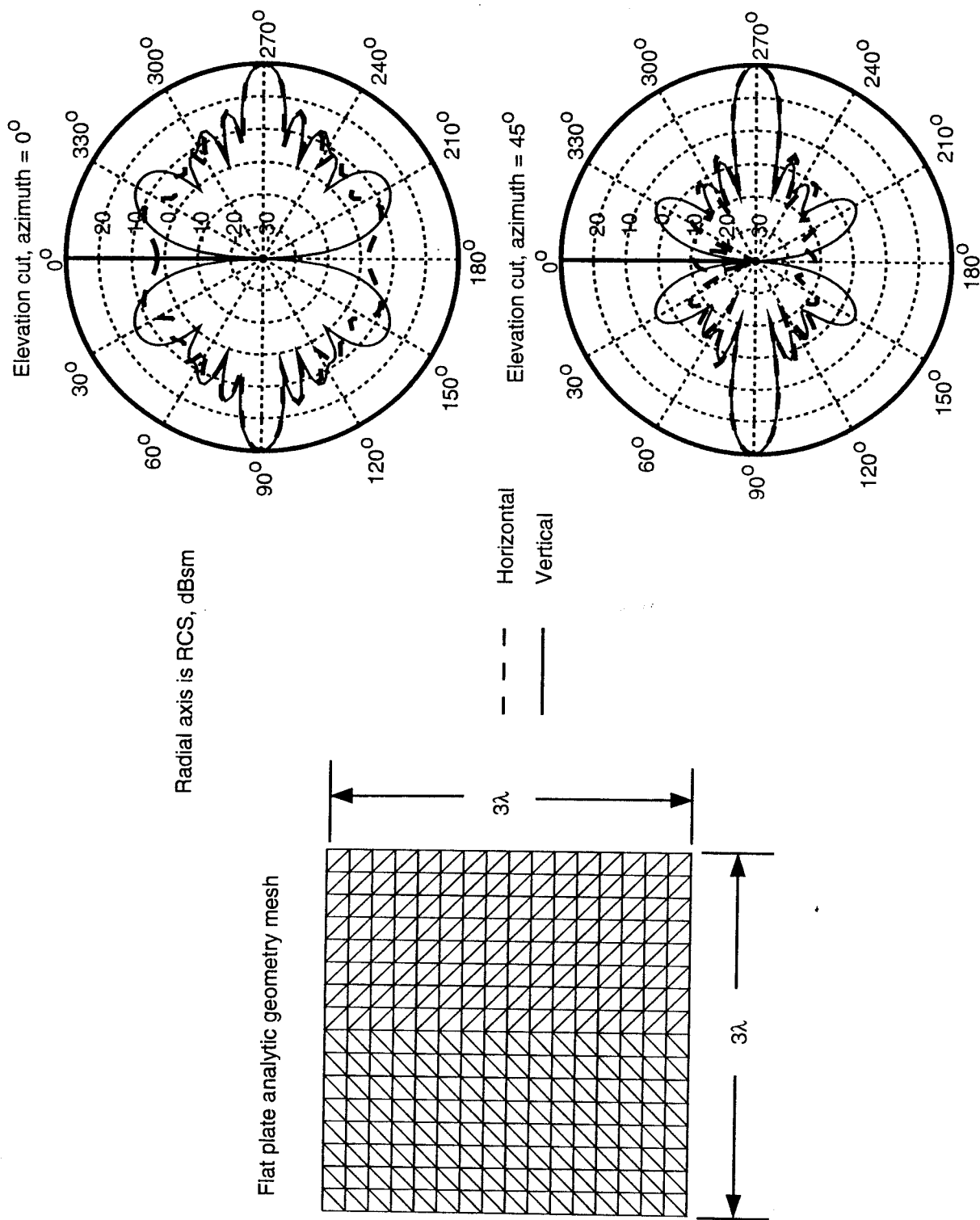
Figure 4. Continued.

EMCC 2-D benchmark 1 geometry



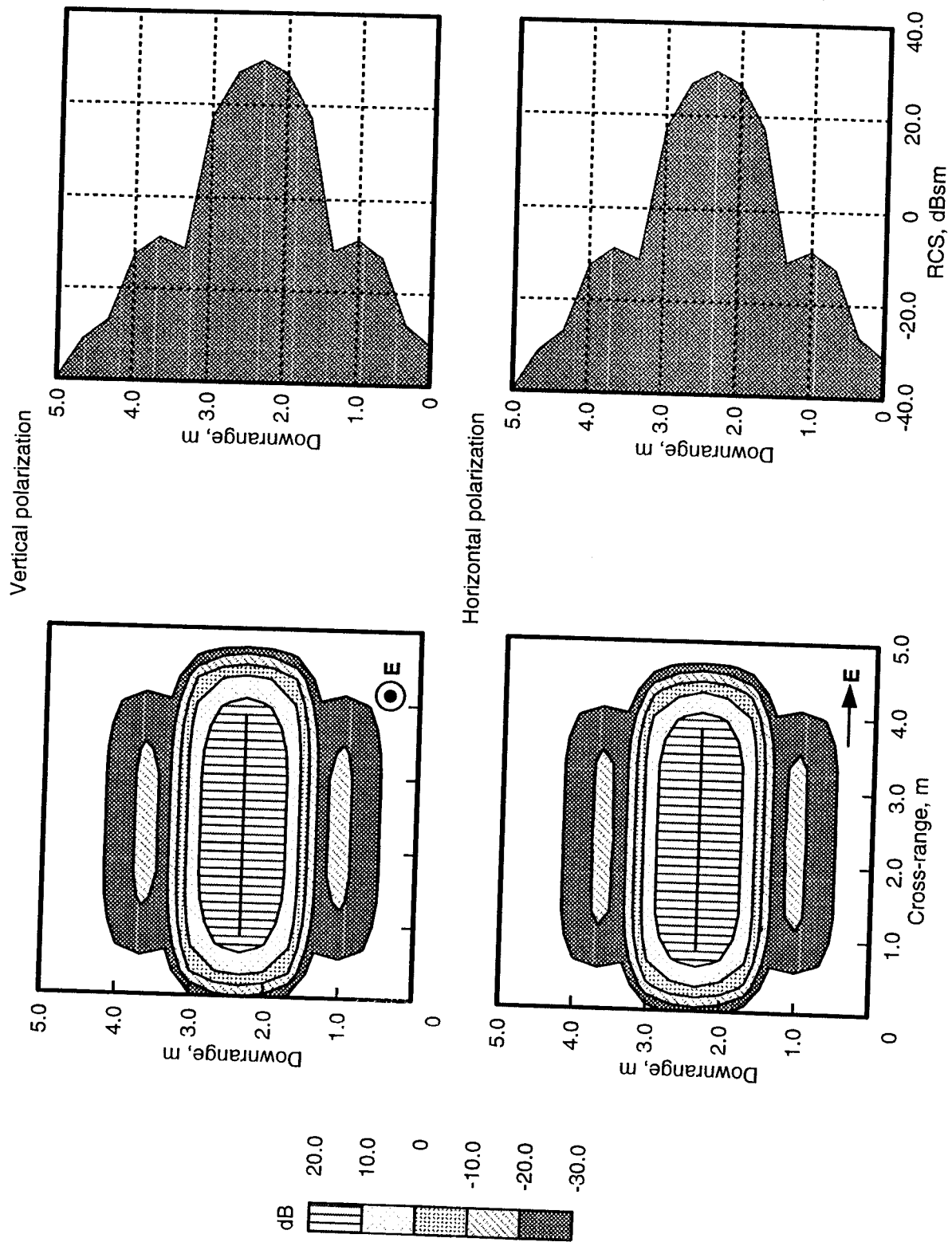
(c) Vertical polarization.

Figure 4. Concluded.



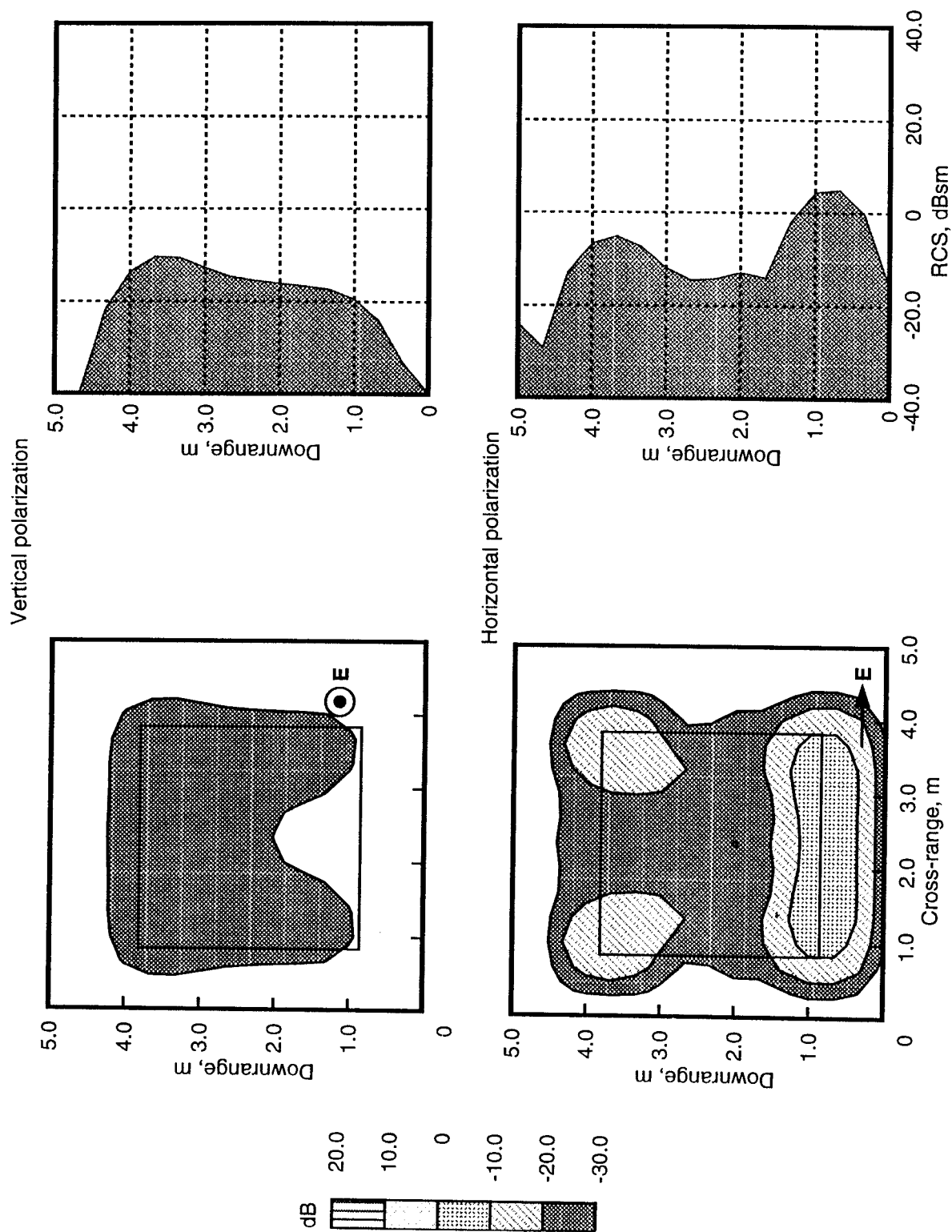
(a) Plate geometry and RCS polar plots.

Figure 5. Three-wavelength square metal plate MOM3D 1-D and 2-D images for three views. Frequency = 0.3 GHz; 0.5λ resolution; and horizontal and vertical polarization.



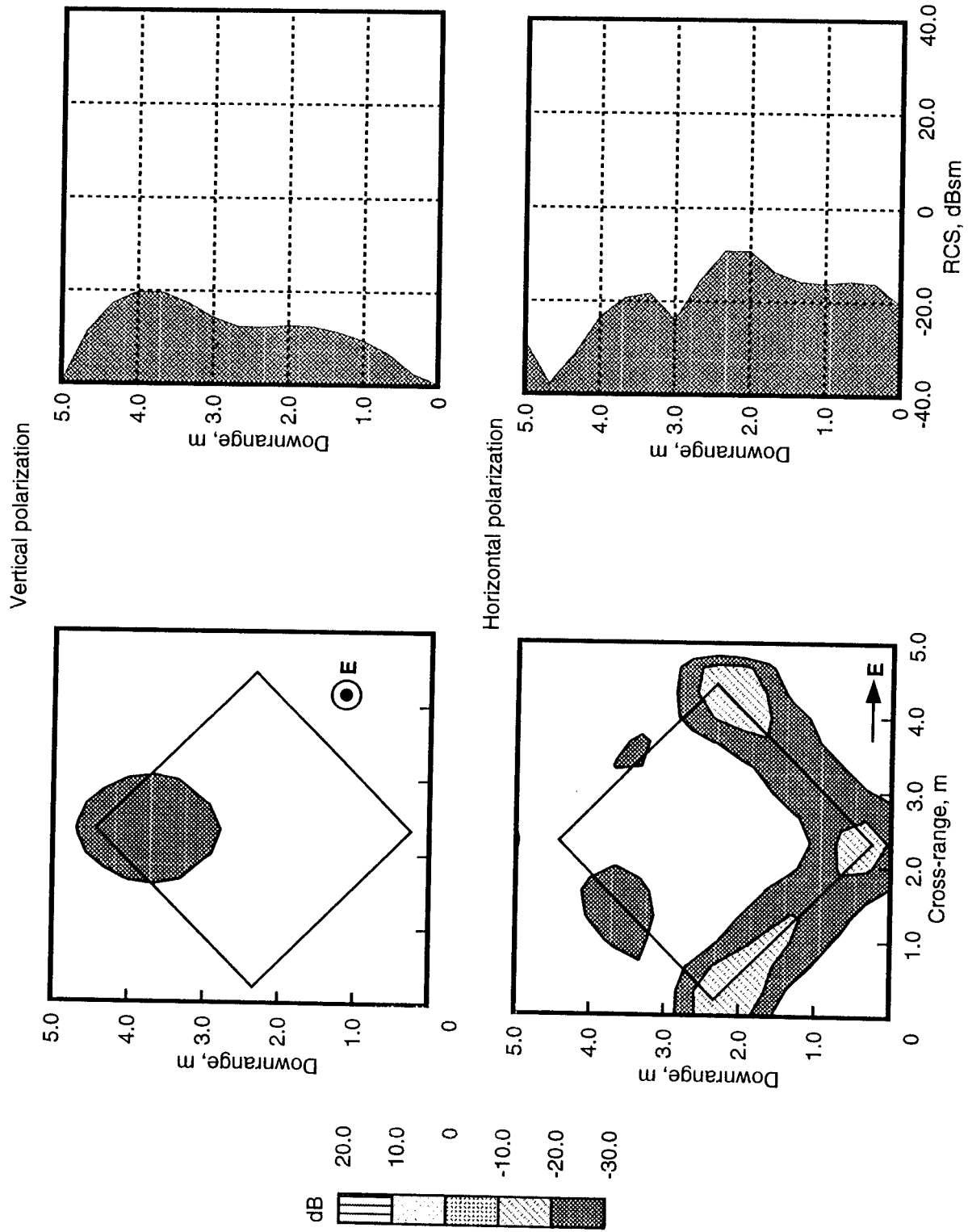
(b) View 1. Azimuth = 0° and Elevation = 90°.

Figure 5. Continued.



(c) View 2. Azimuth = 0° and Elevation = 10°.

Figure 5. Continued.



(d) View 3. Azimuth = 45° and Elevation = 10°.

Figure 5. Concluded.

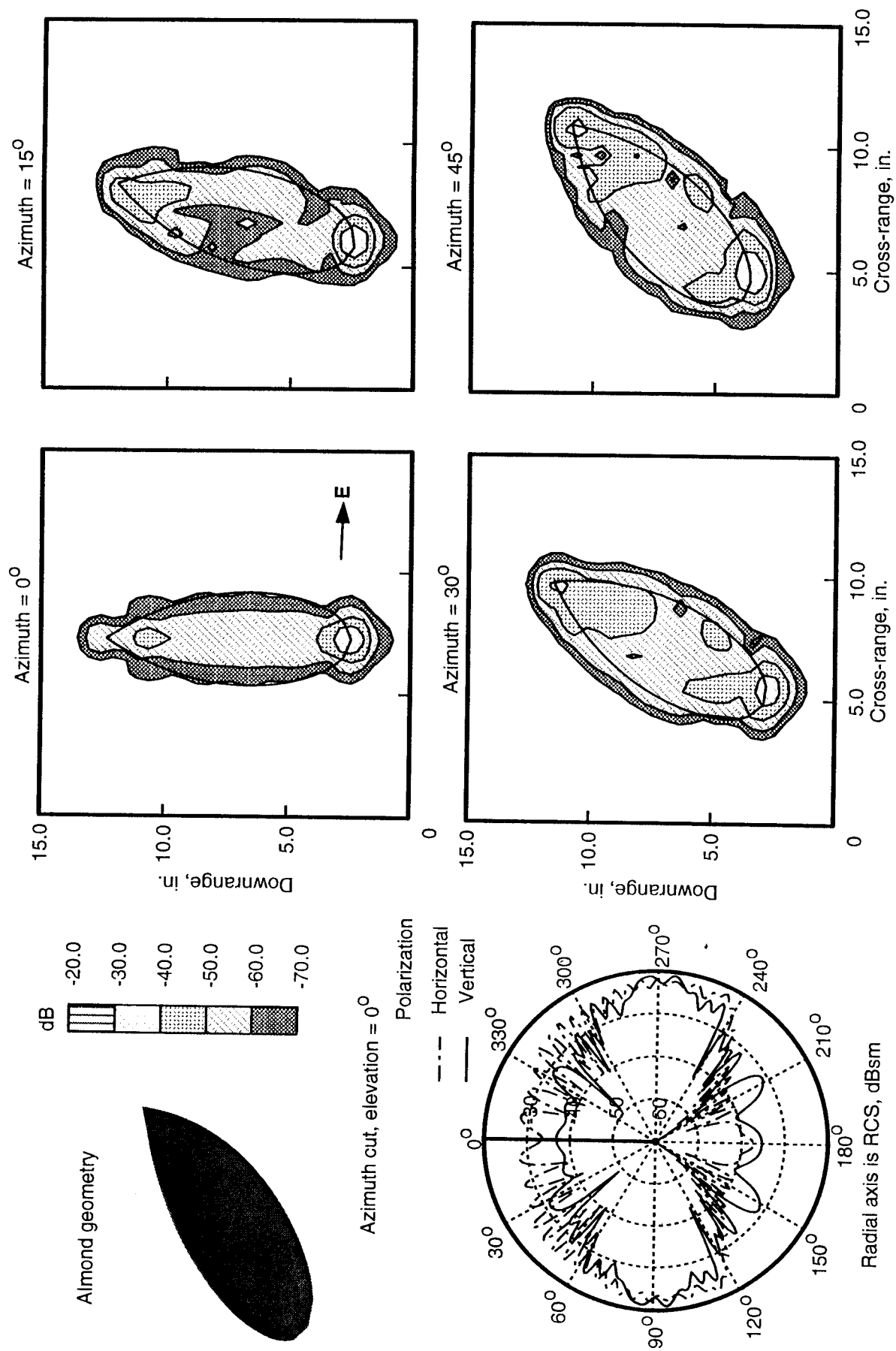


Figure 6. MOM3D 2-D images for 9.936-in. NASA almond. Frequency = 9.92 GHz; horizontal polarization; and 0.5λ resolution.

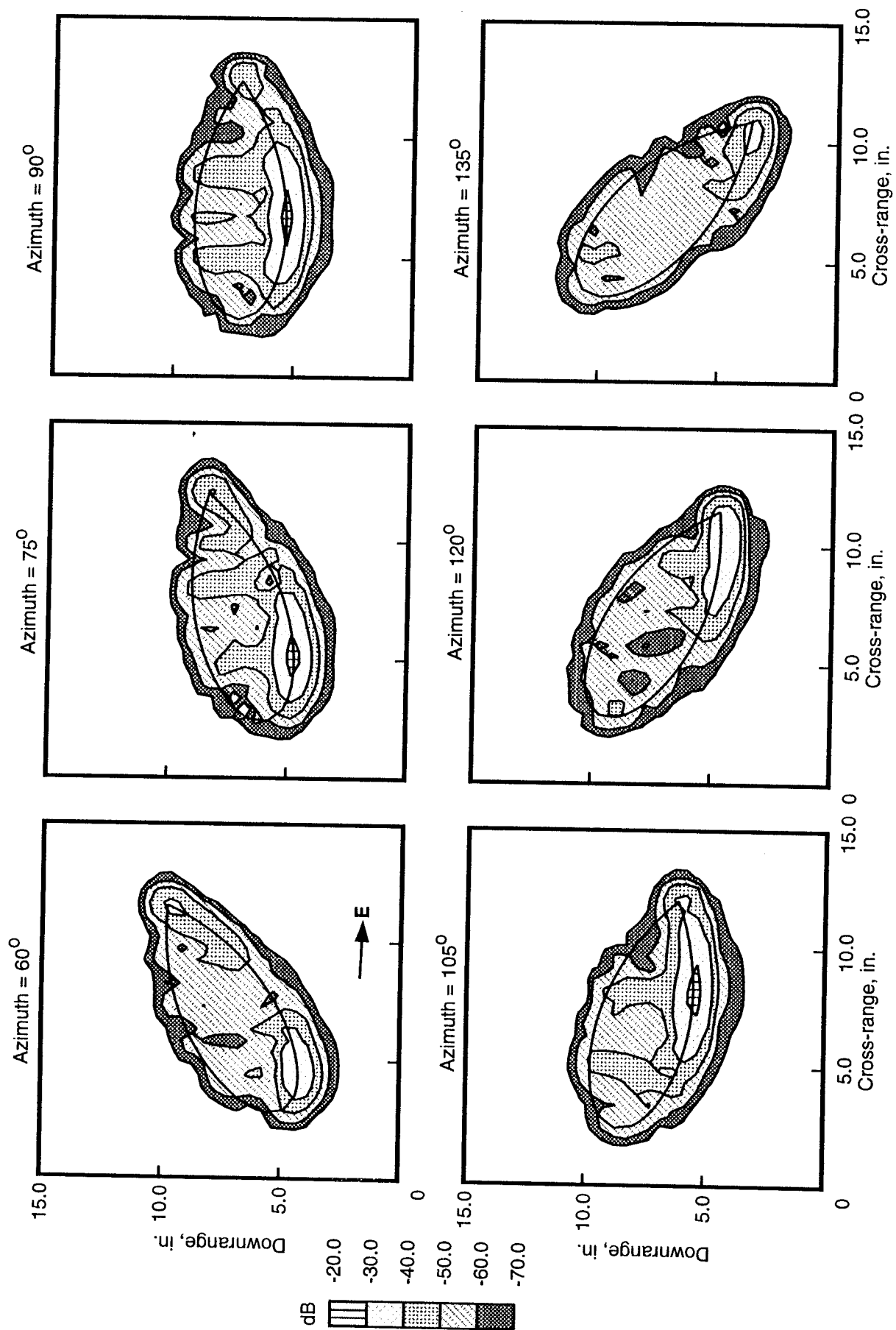


Figure 6. Continued

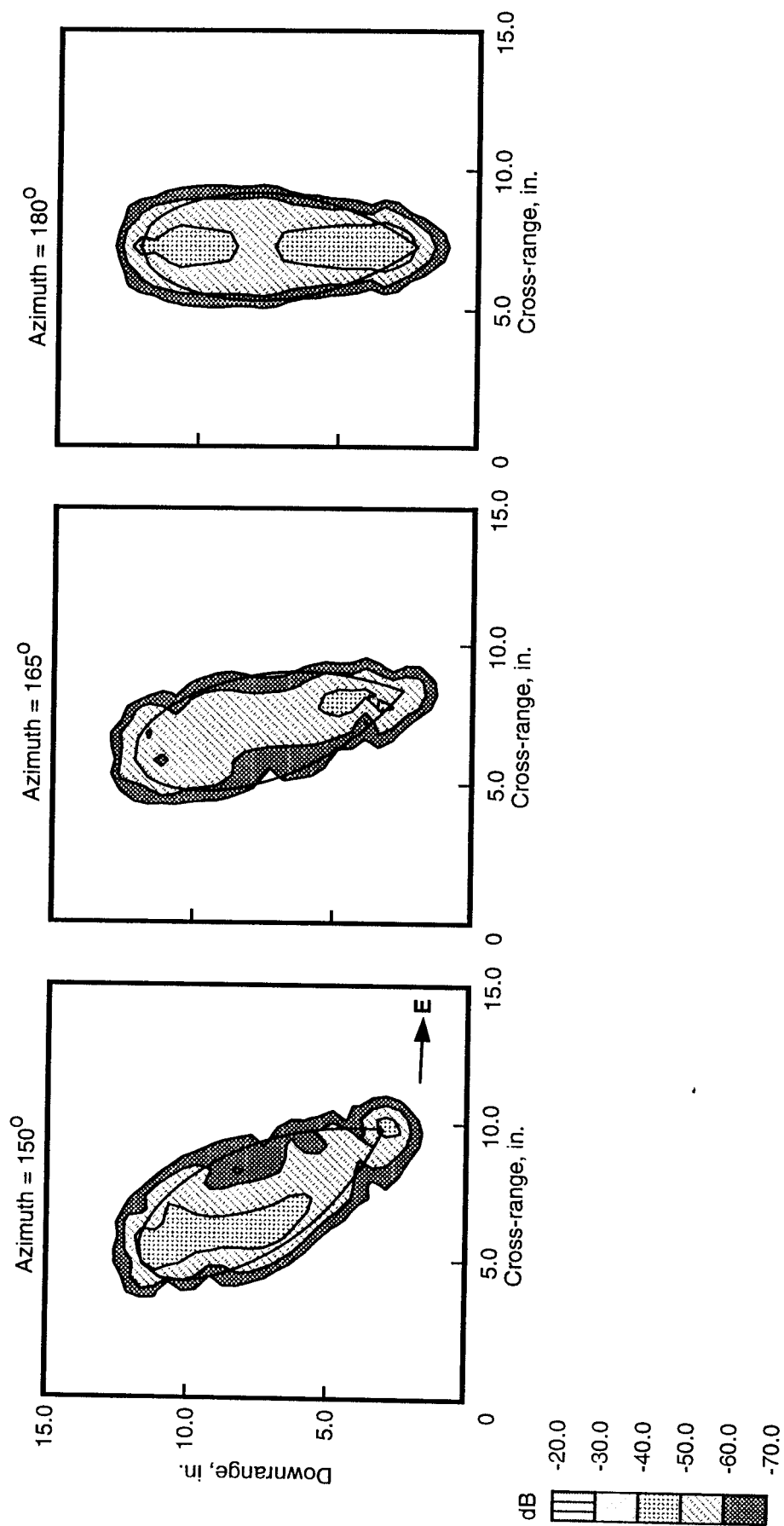


Figure 6. Concluded.

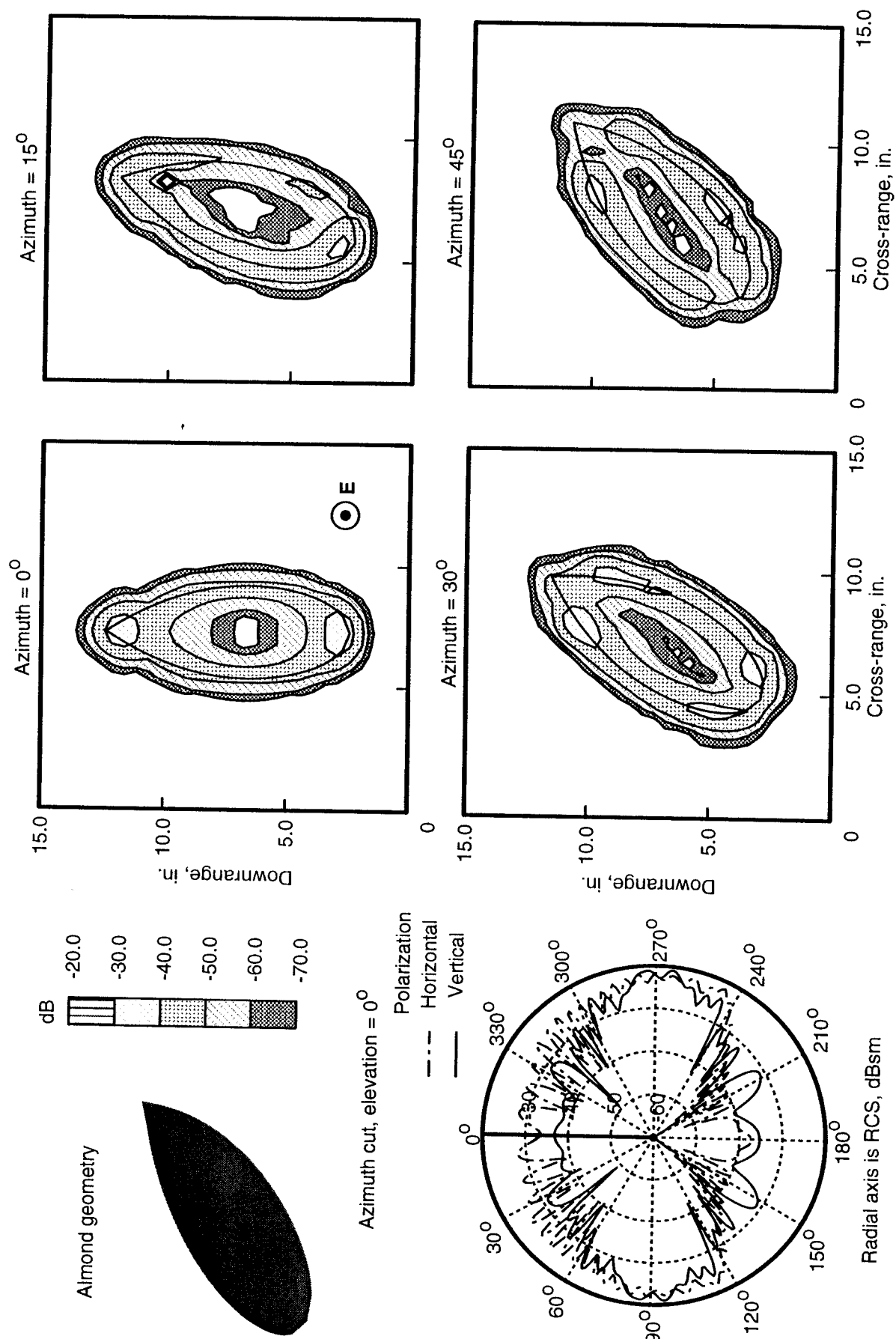


Figure 7. MOM3D 2-D images for 9.936-in. NASA almond. Frequency = 9.92 GHz; vertical polarization; and 0.5λ resolution.

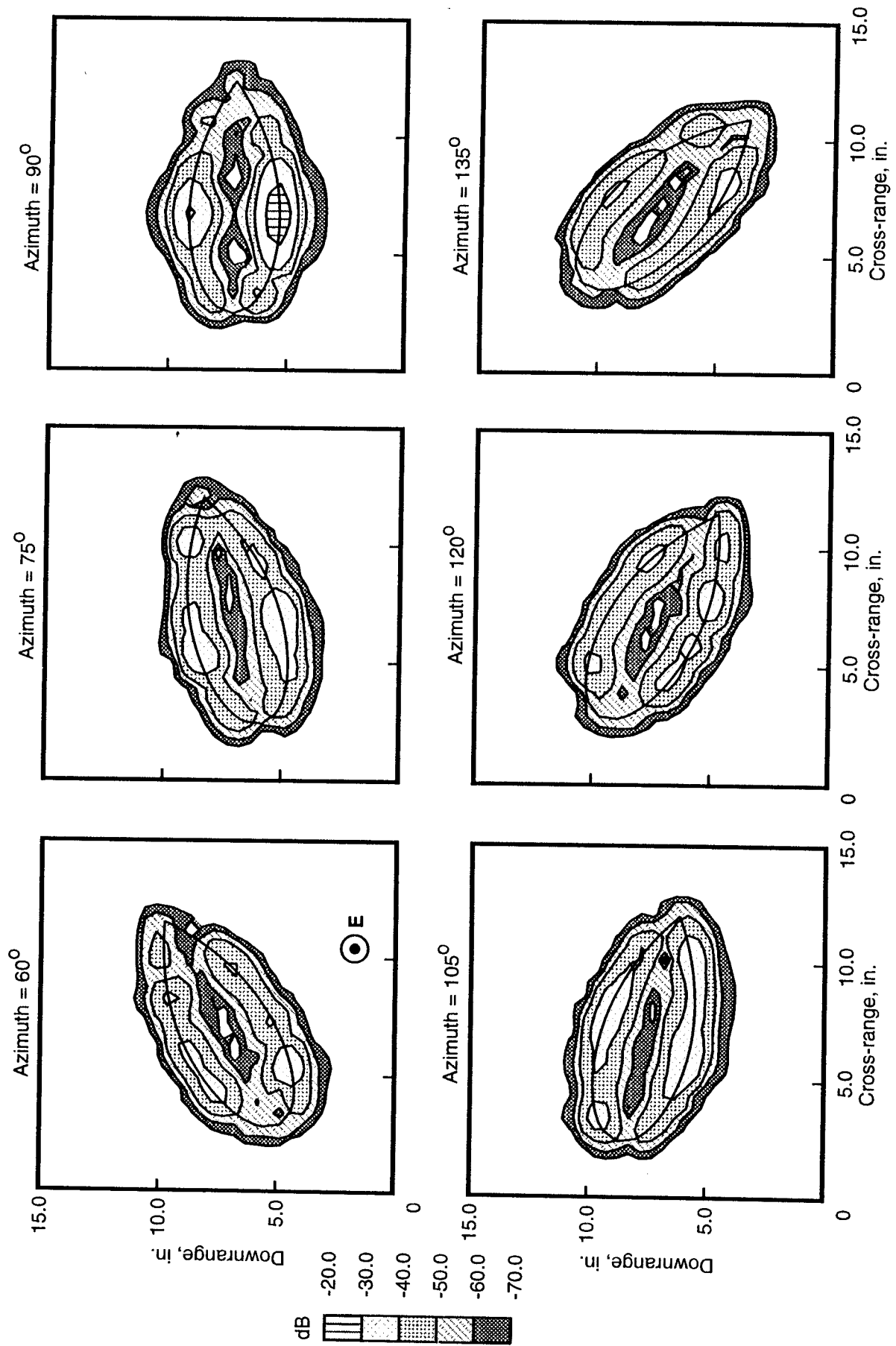


Figure 7. Continued.

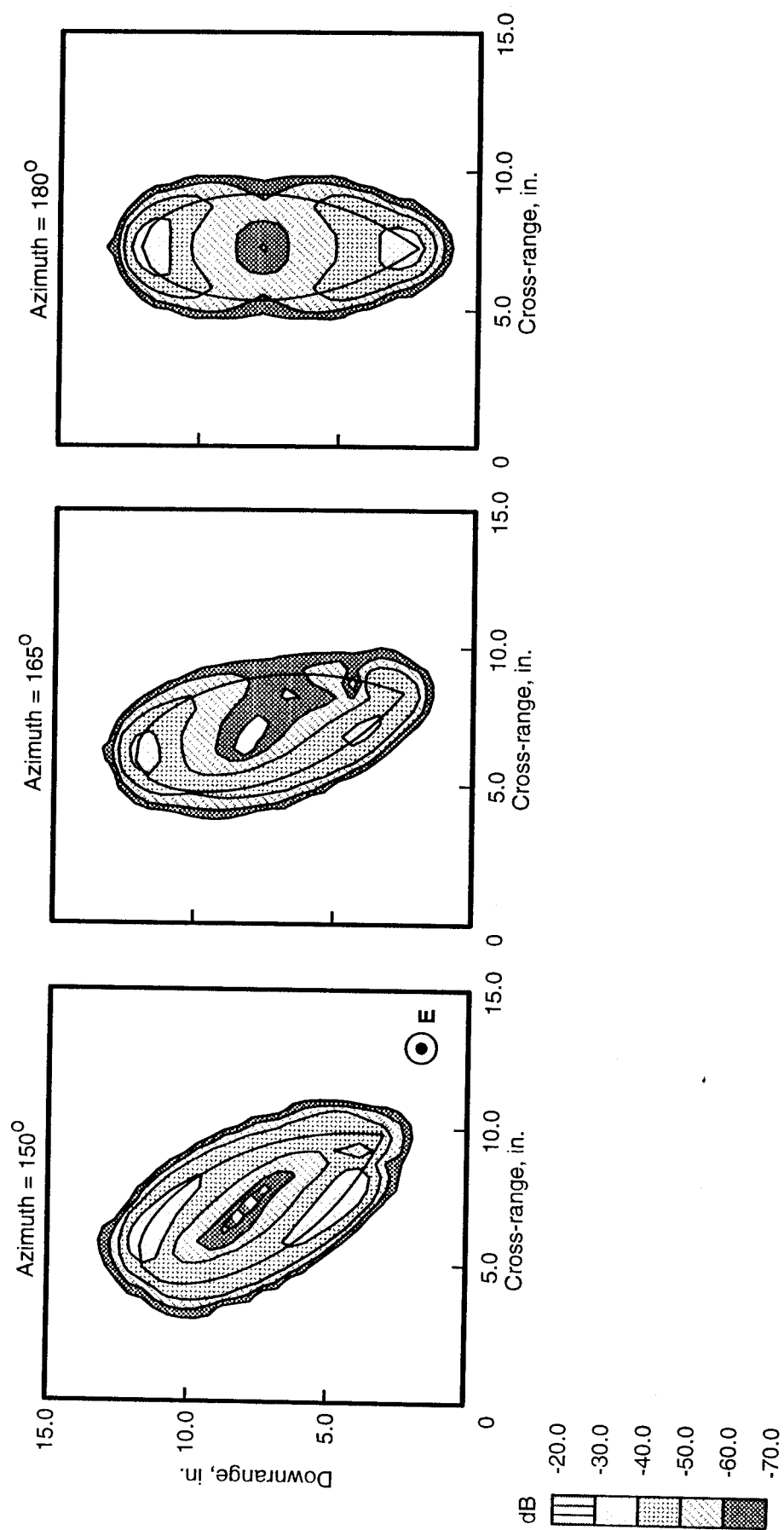
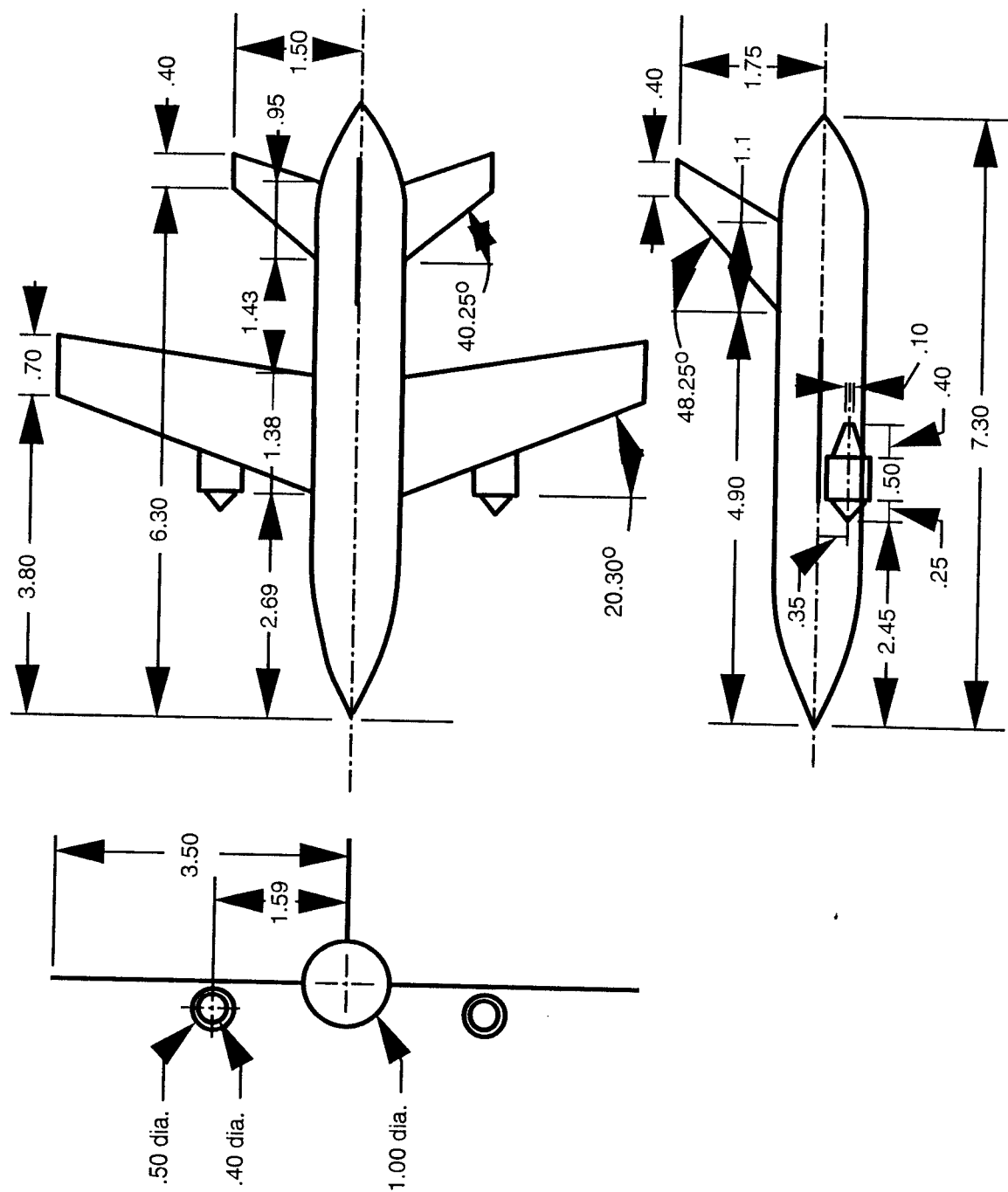
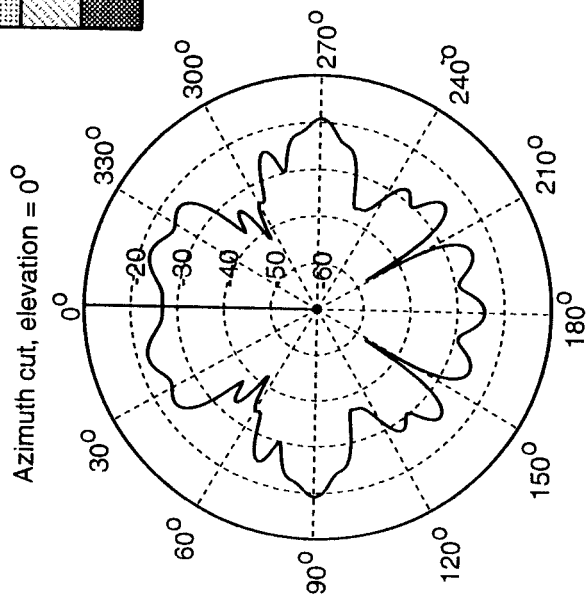
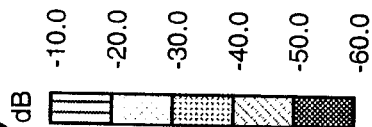
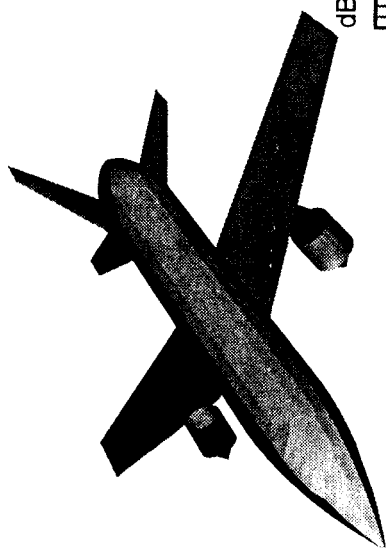


Figure 7. Concluded.

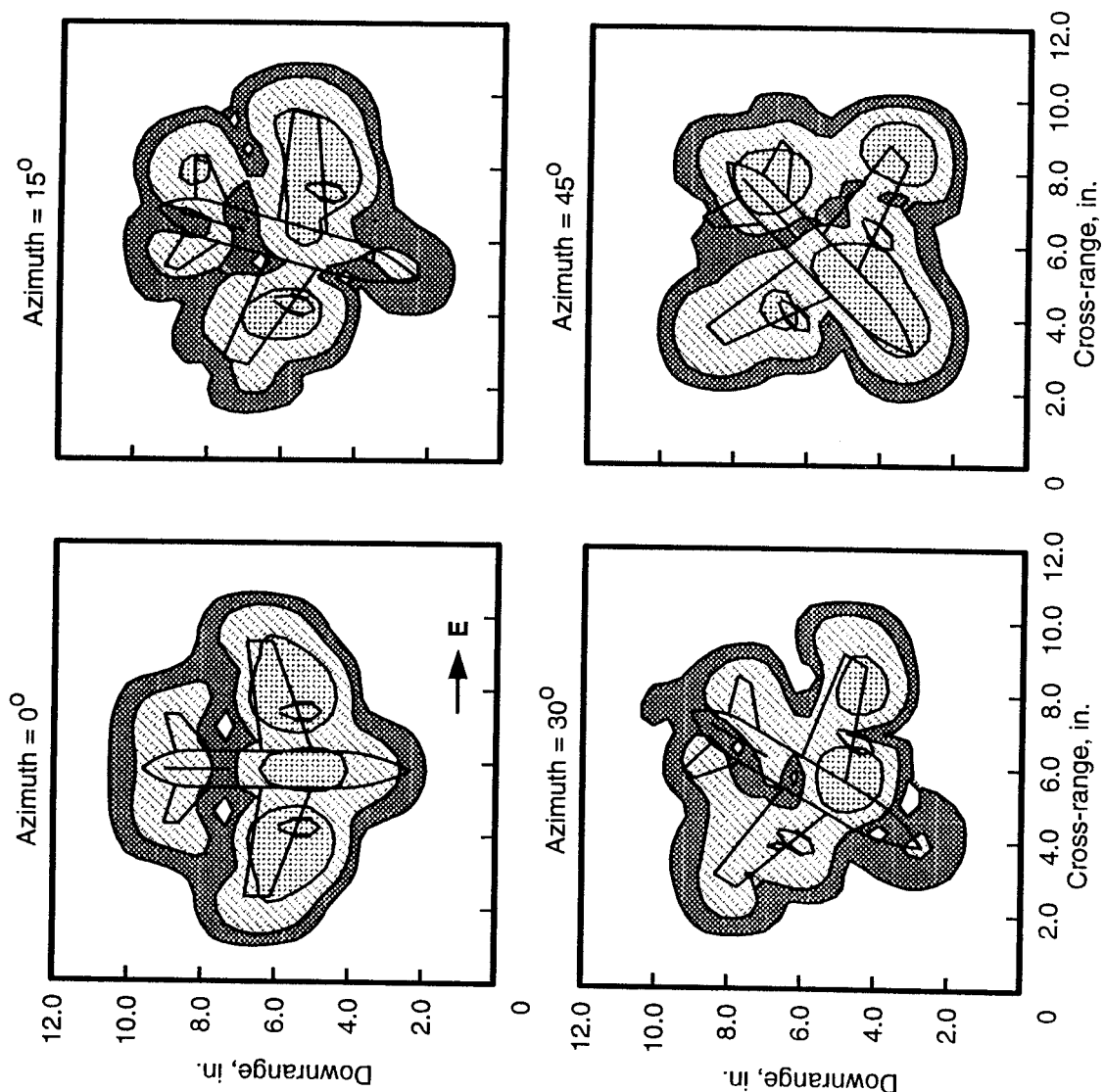


(a) Three views of airplane configuration. All dimensions are in inches.

Figure 8. Airplane configuration geometry and MOM3D 2-D images for multiple azimuth views. Horizontal polarization.

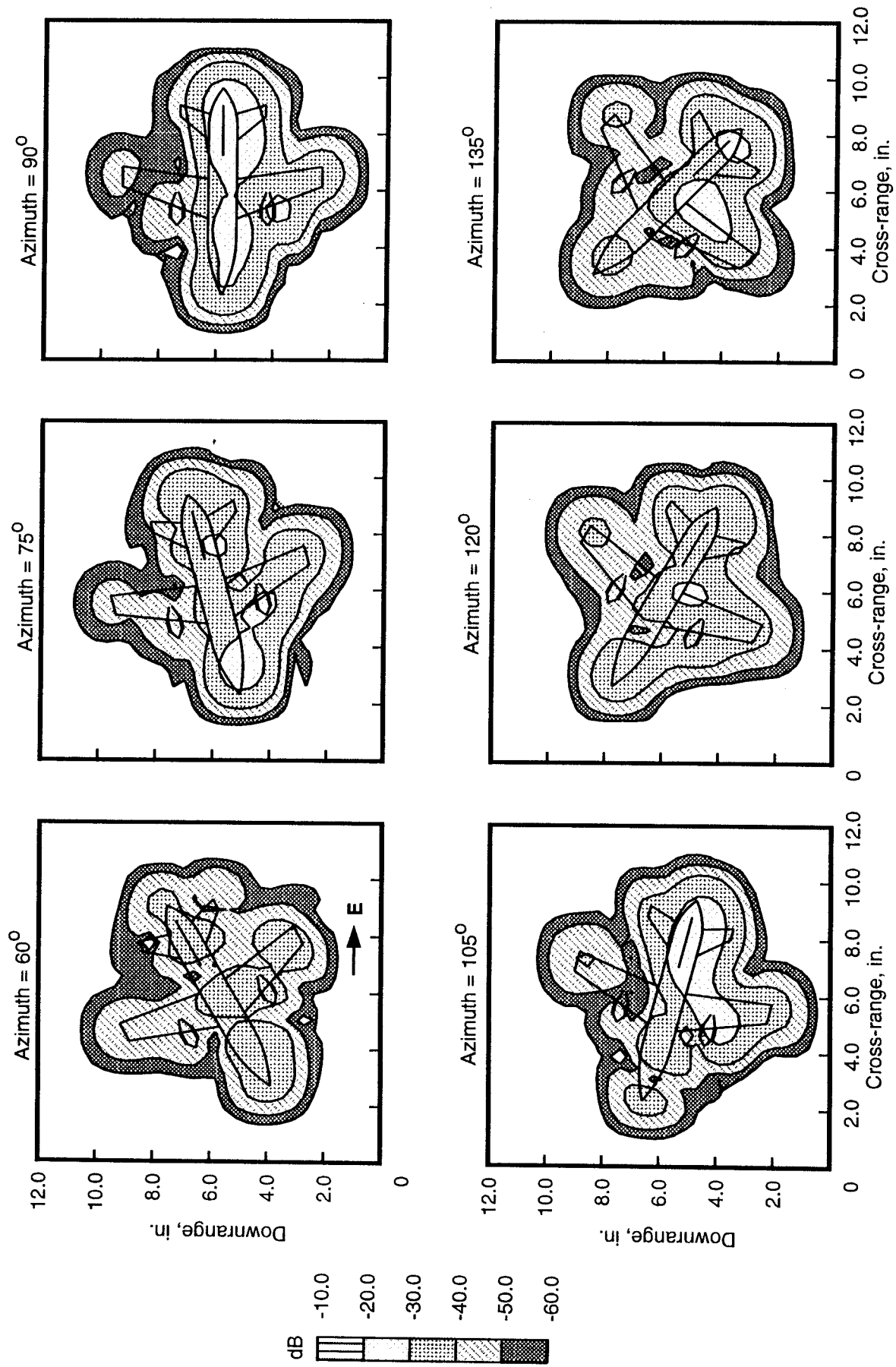


Radial axis is RCS, dBsm



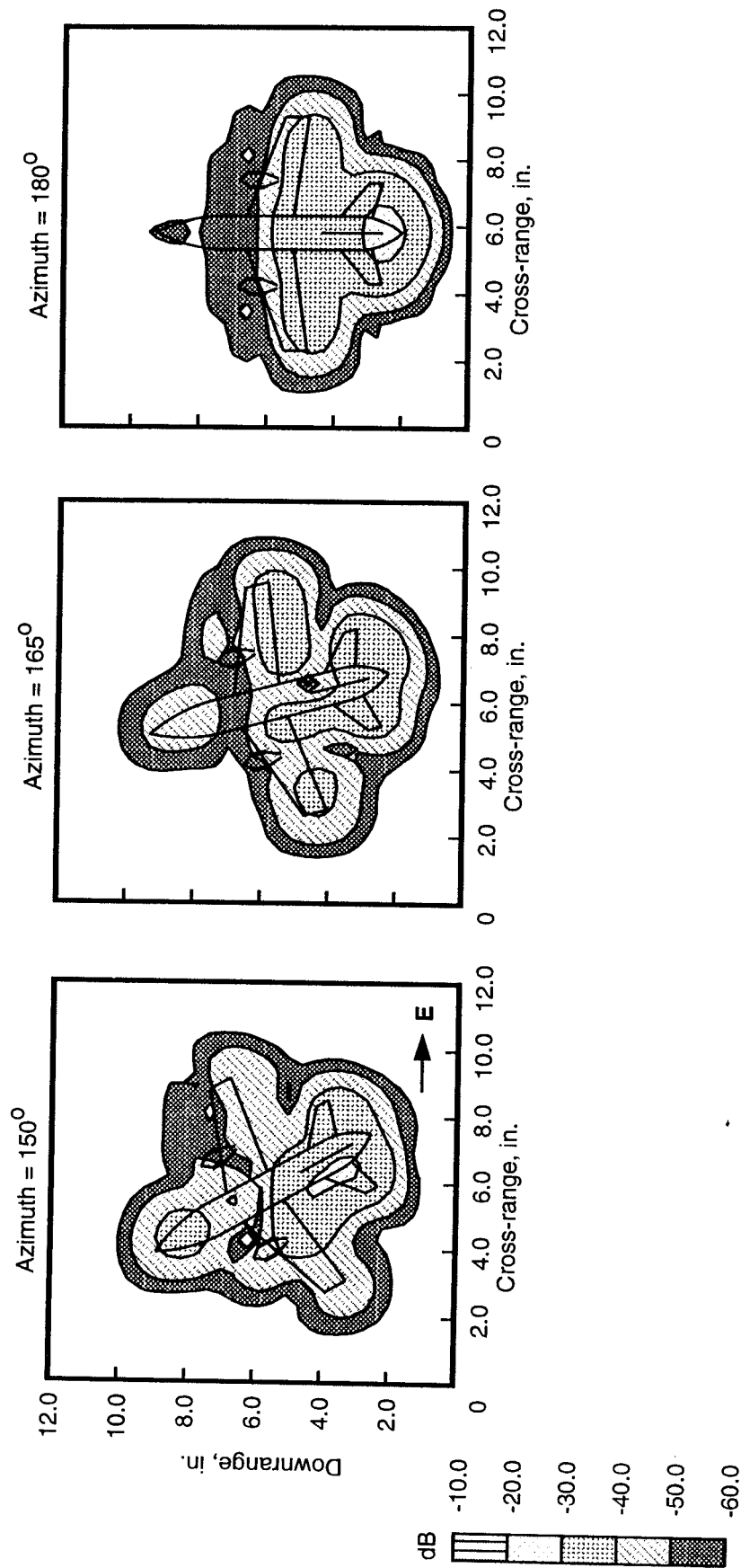
(b) RCS polar and MOM3D 2-D contour images. Horizontal polarization; Frequency = 6 GHz.

Figure 8. Continued.



(b) Continued.

Figure 8. Continued



(b) Concluded.

Figure 8. Concluded.

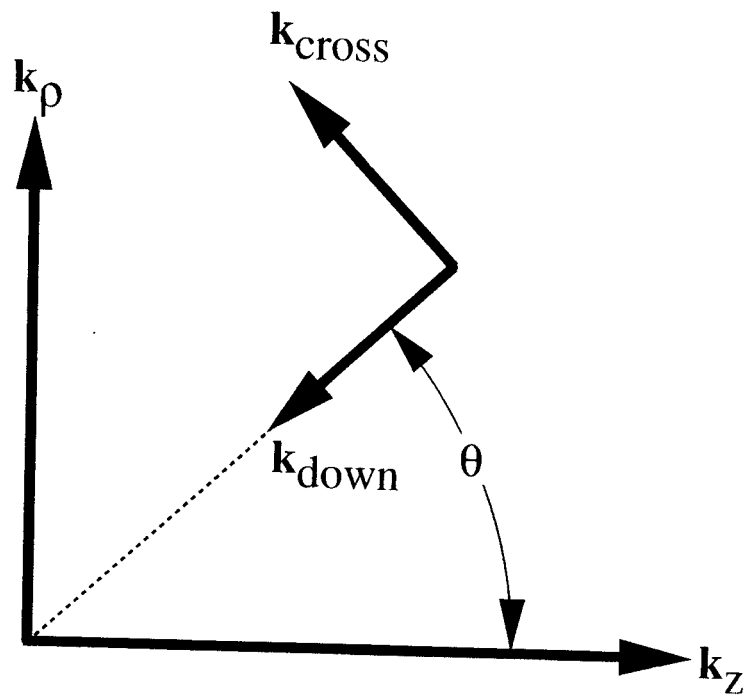


Figure 9. Body-of-revolution image coordinates for \mathbf{k}^s in terms of BOR k_ρ and k_z coordinates.

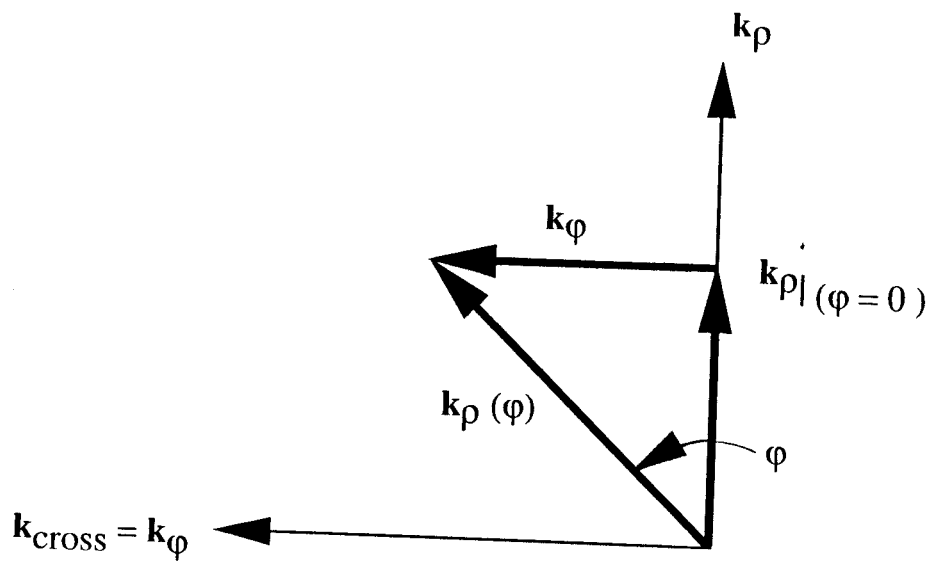


Figure 10. Body-of-revolution volume image k -space transform.

Body-of-revolution sphere geometry

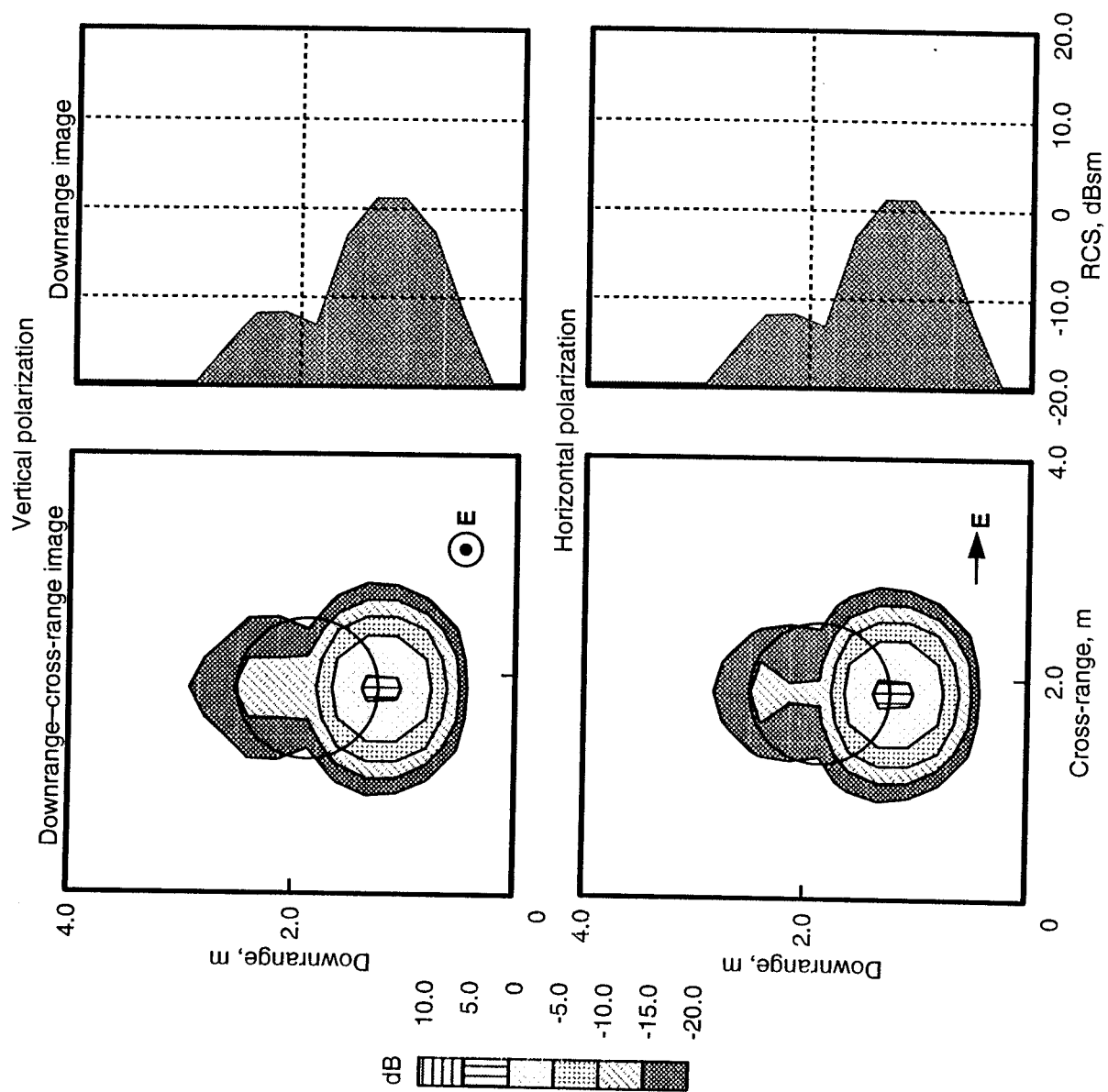
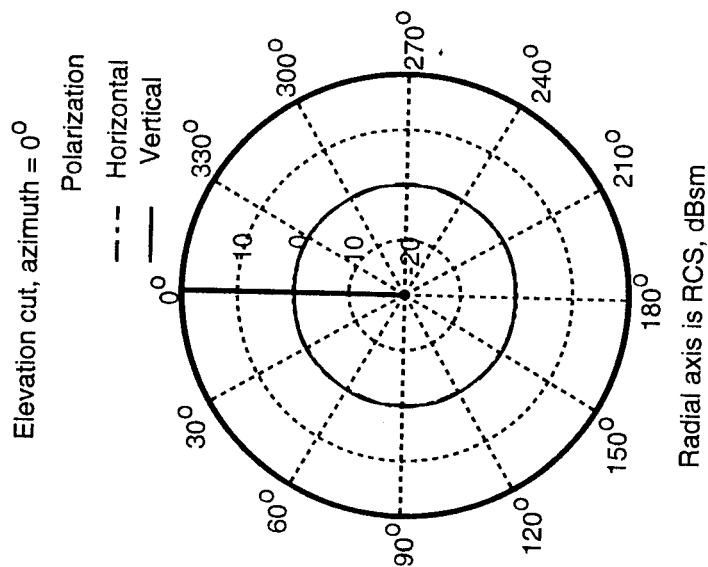
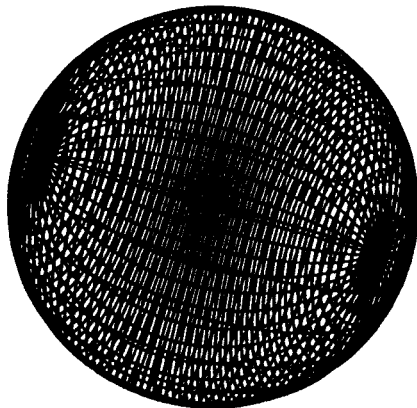


Figure 11. BOR image results of sphere, $ka = 4$. Frequency = 0.3 GHz; 0.5λ resolution; and vertical and horizontal polarizations.

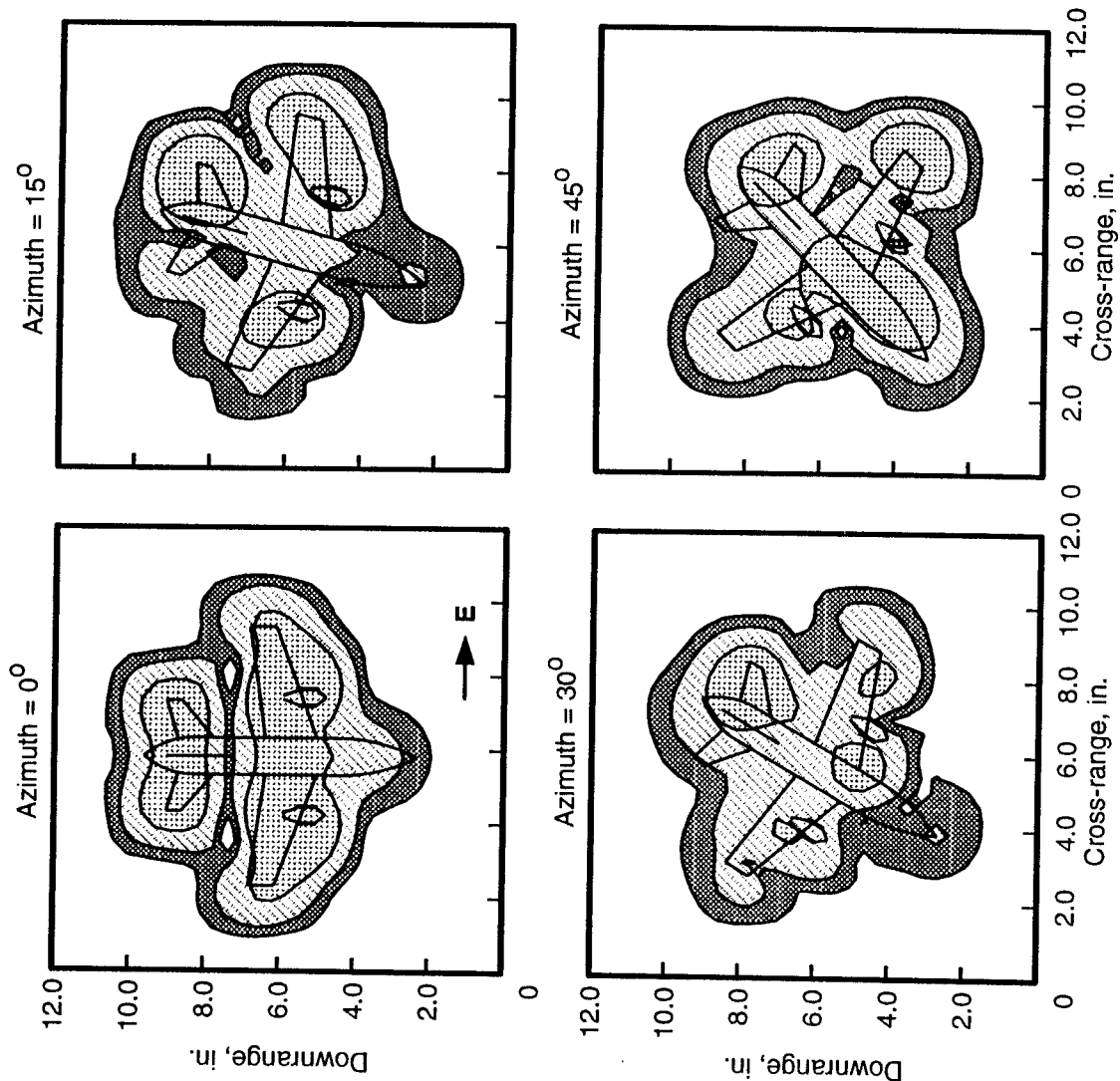
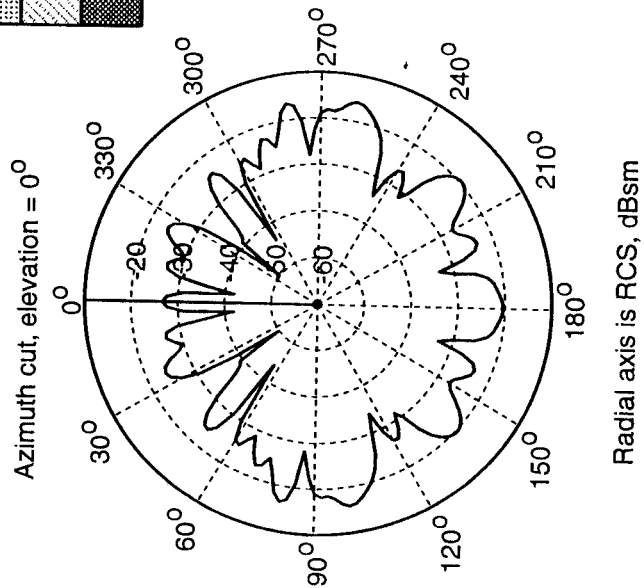
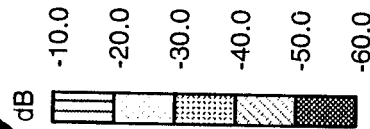


Figure 12. BOR-patch 2-D images for airplane configuration. Frequency = 6 GHz; horizontal polarization; Elevation = 0°; and 0.5λ resolution.

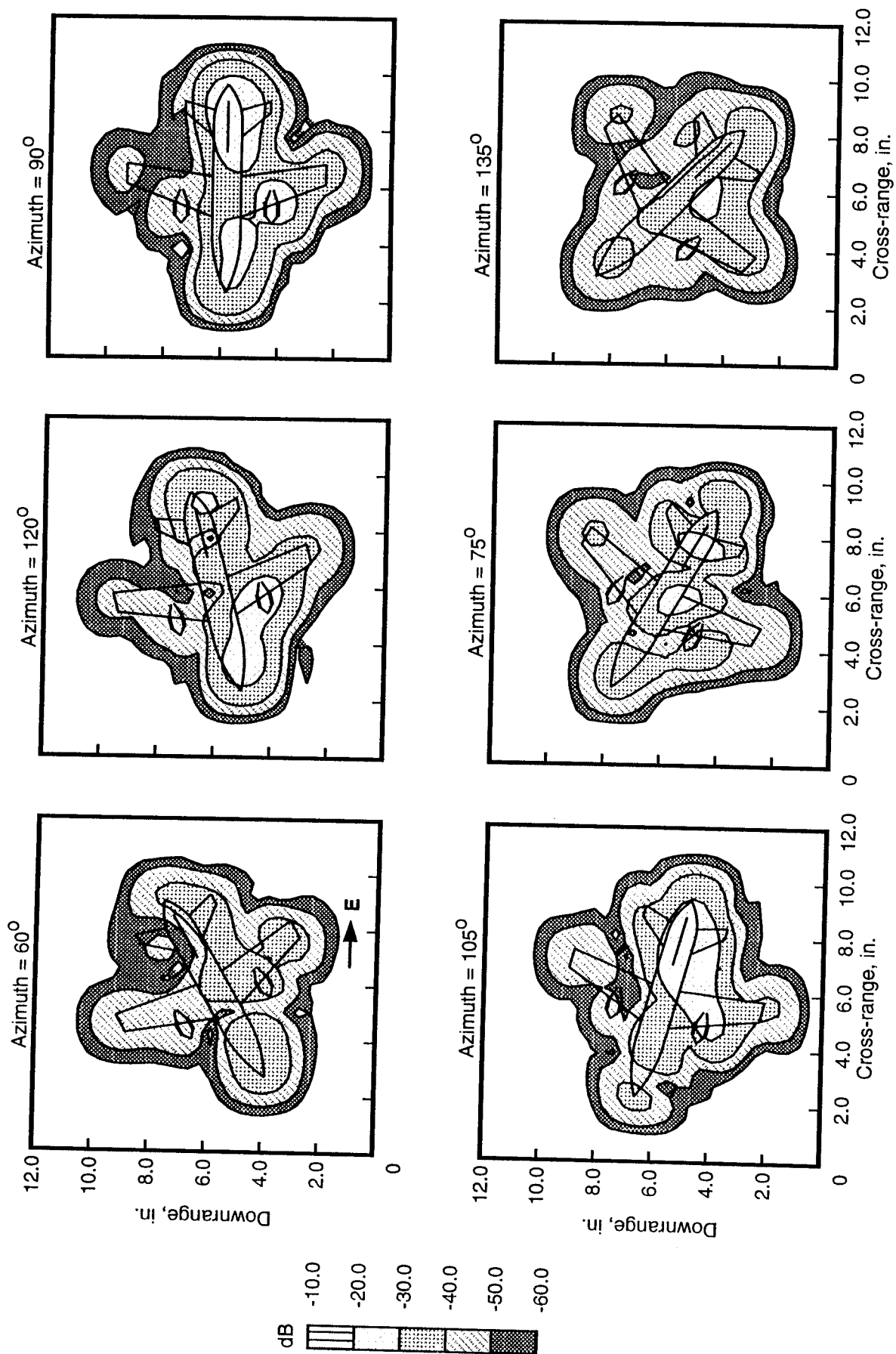


Figure 12. Continued.

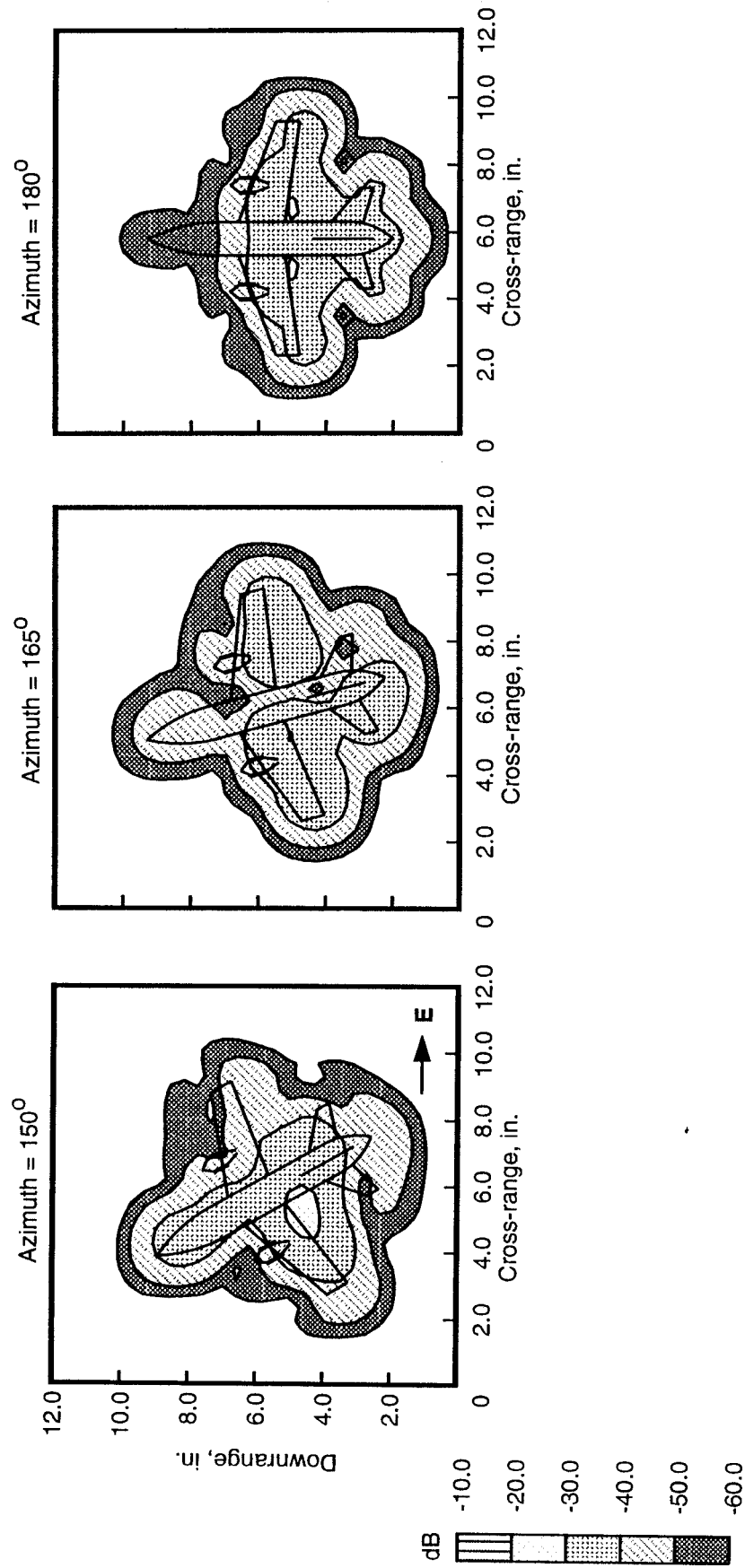


Figure 12. Concluded.

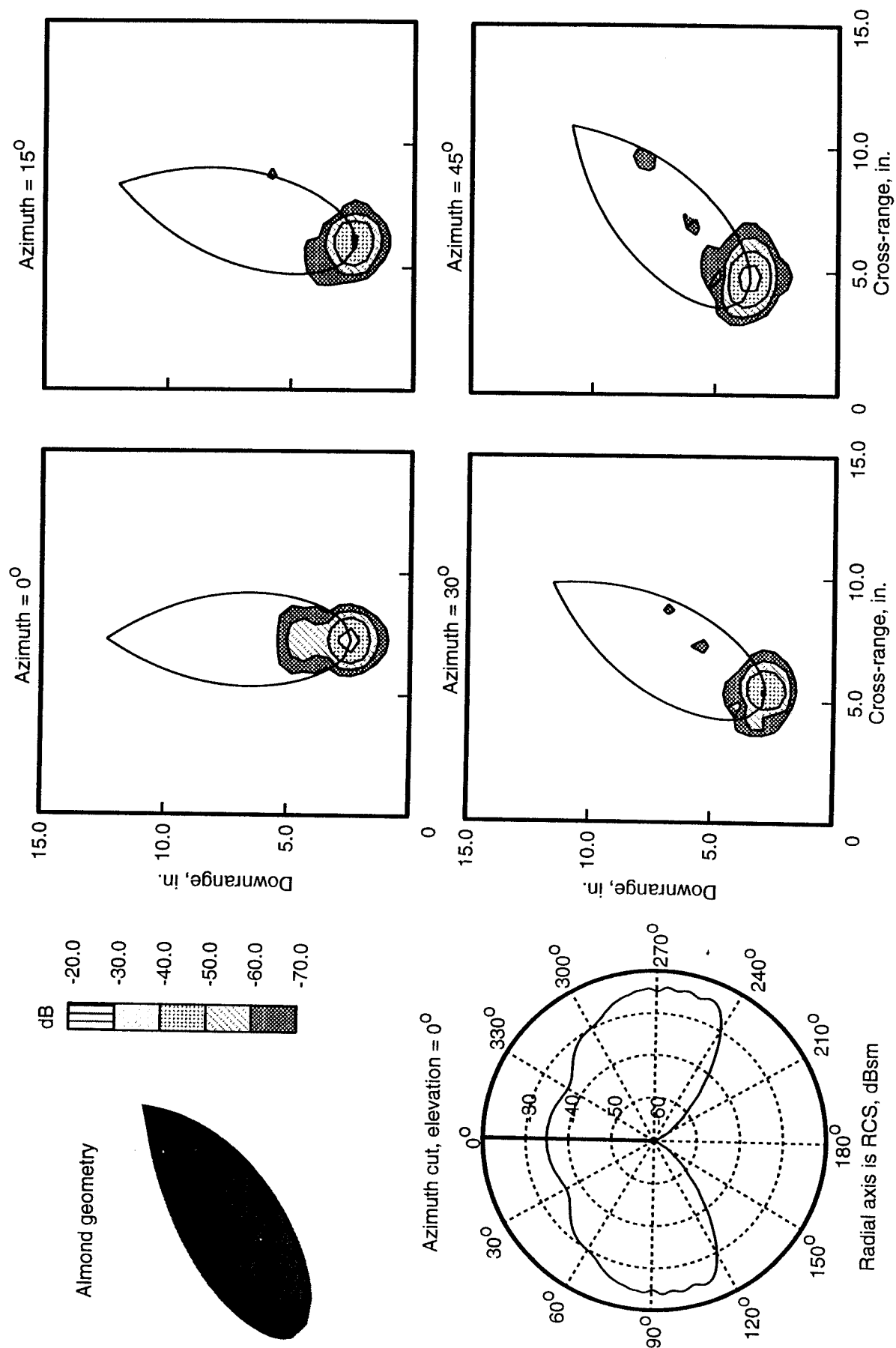


Figure 13. Physical optics 2-D images for 9.936-in. NASA almond. Frequency = 9.92 GHz; polarization independent; and 0.5λ resolution.

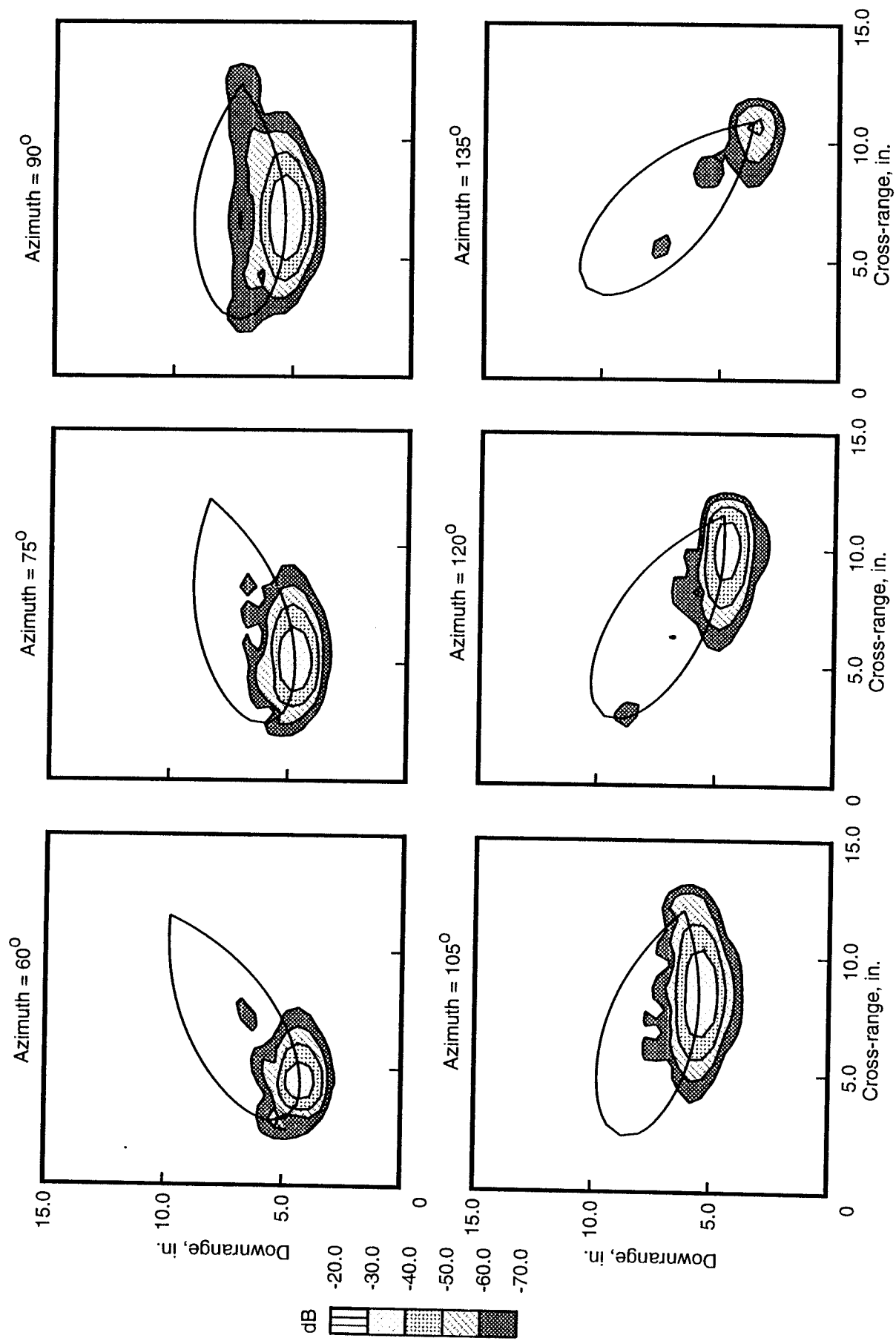


Figure 13. Continued.

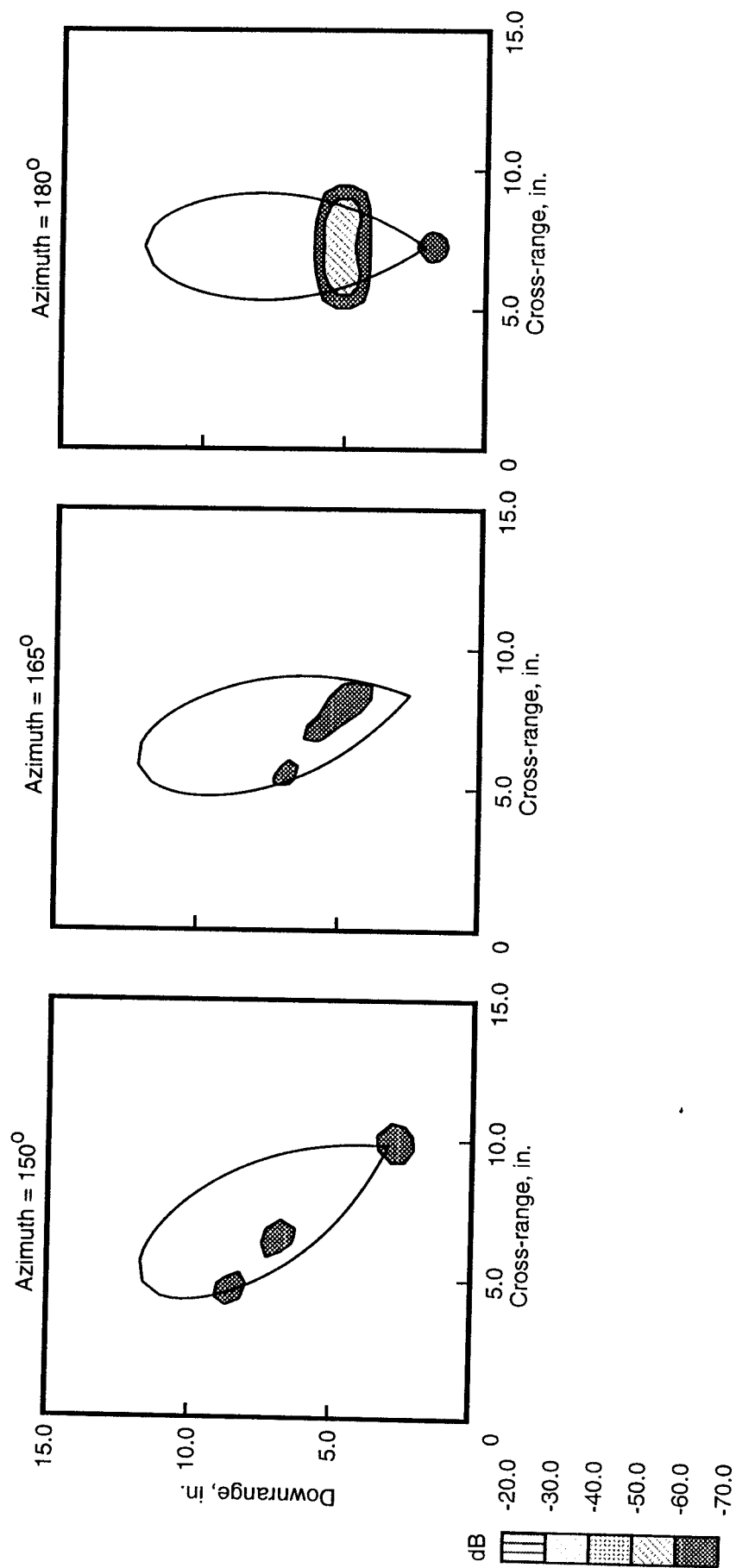


Figure 13. Concluded.

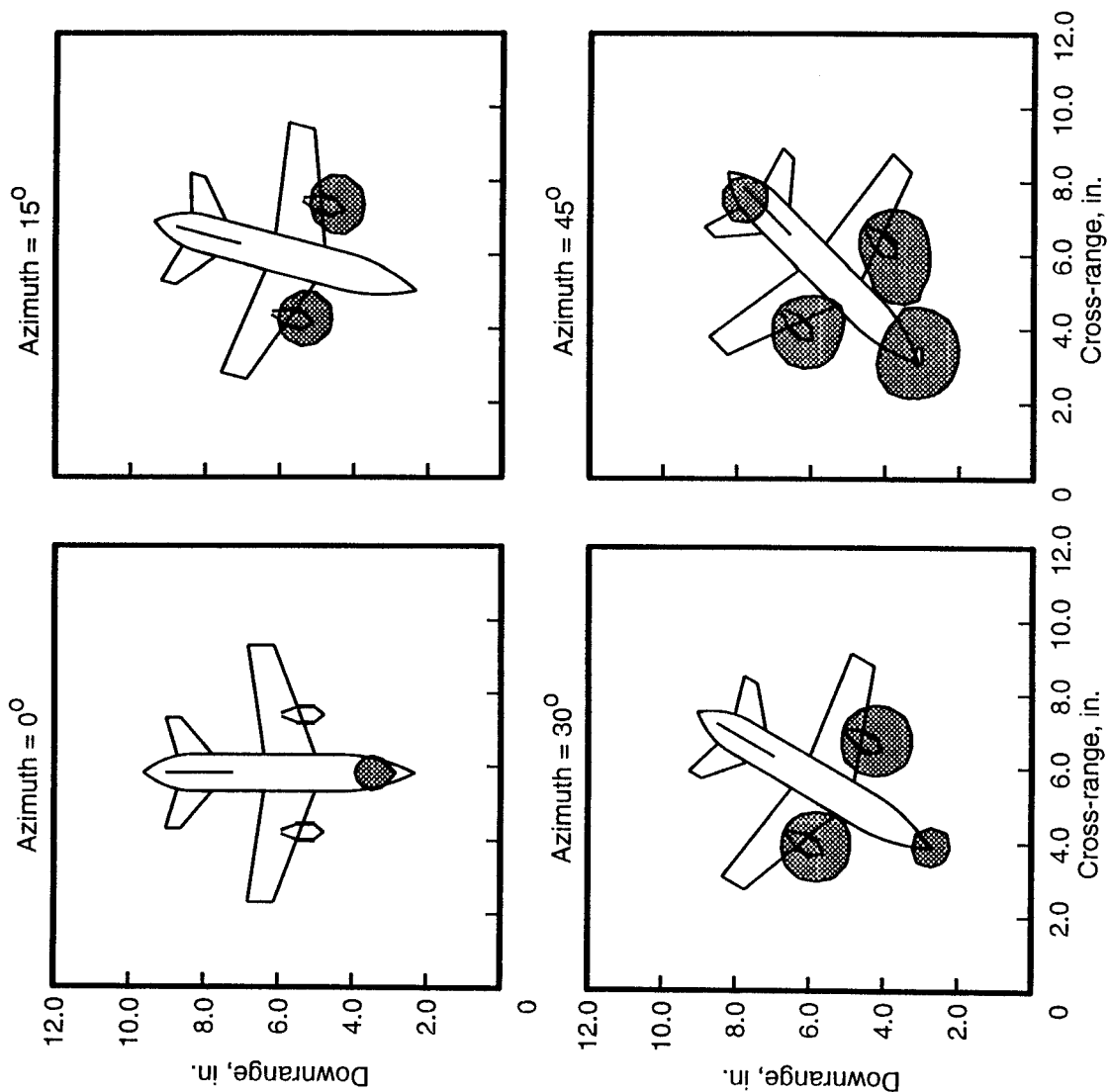
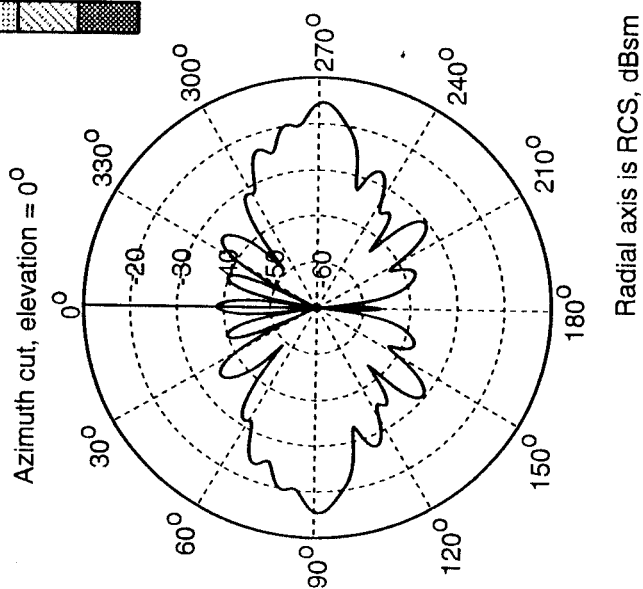
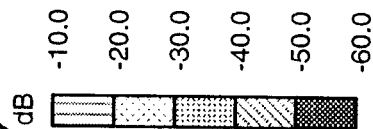
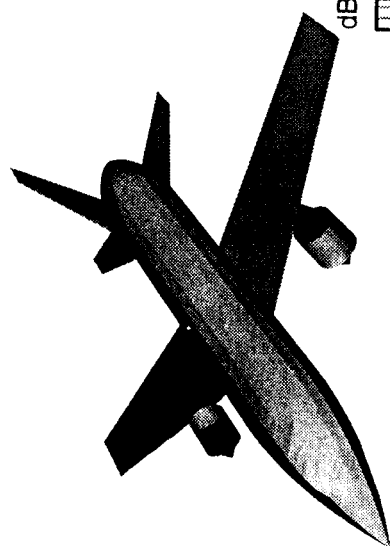


Figure 14. Physical optics 2-D images for airplane configuration. Frequency = 6 GHz; polarization independent; Elevation = 0°; and 0.5λ resolution.

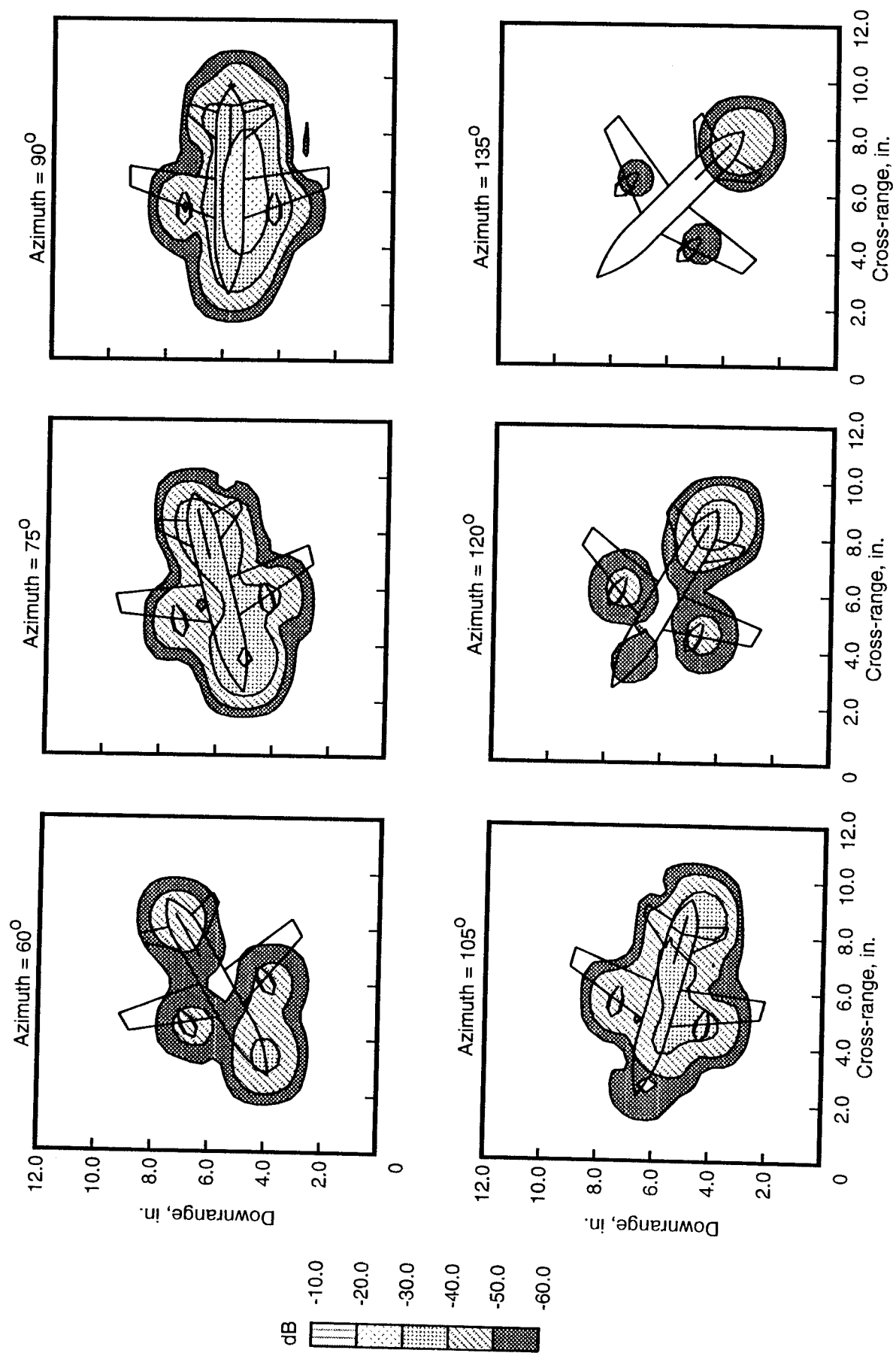


Figure 14. Continued.

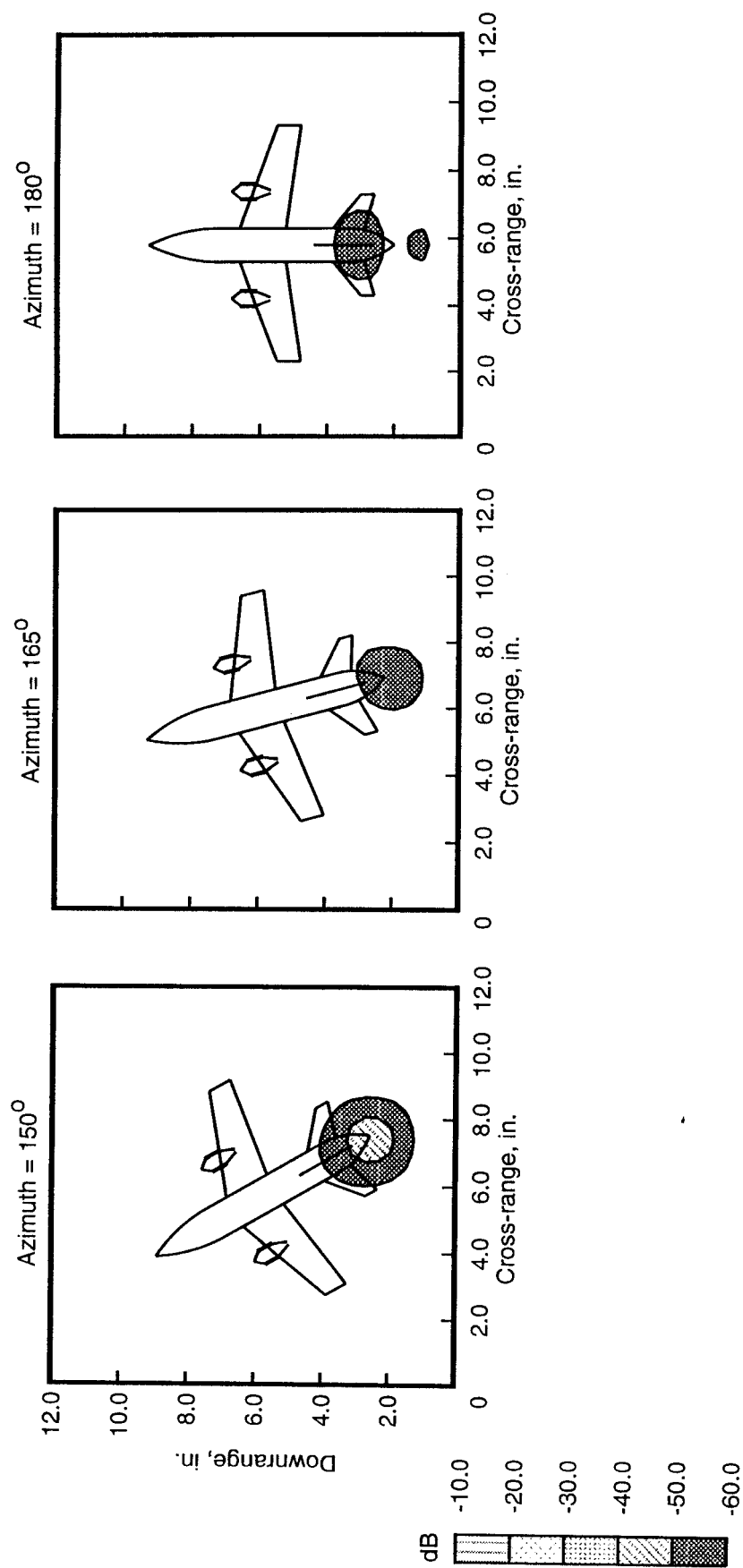
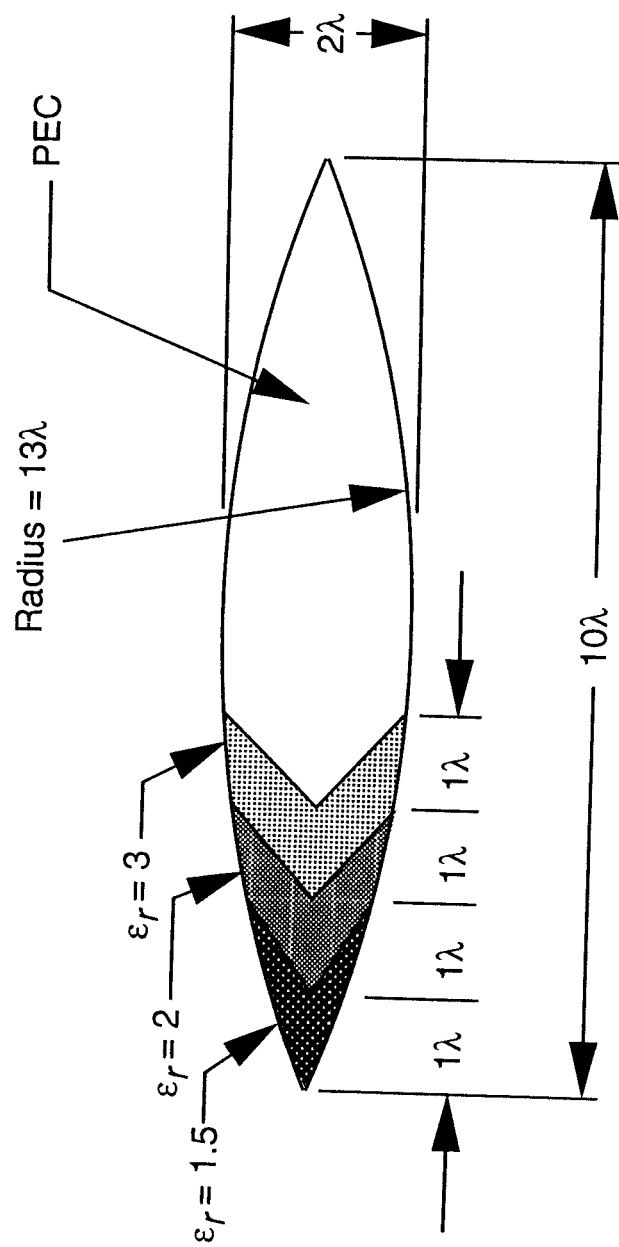
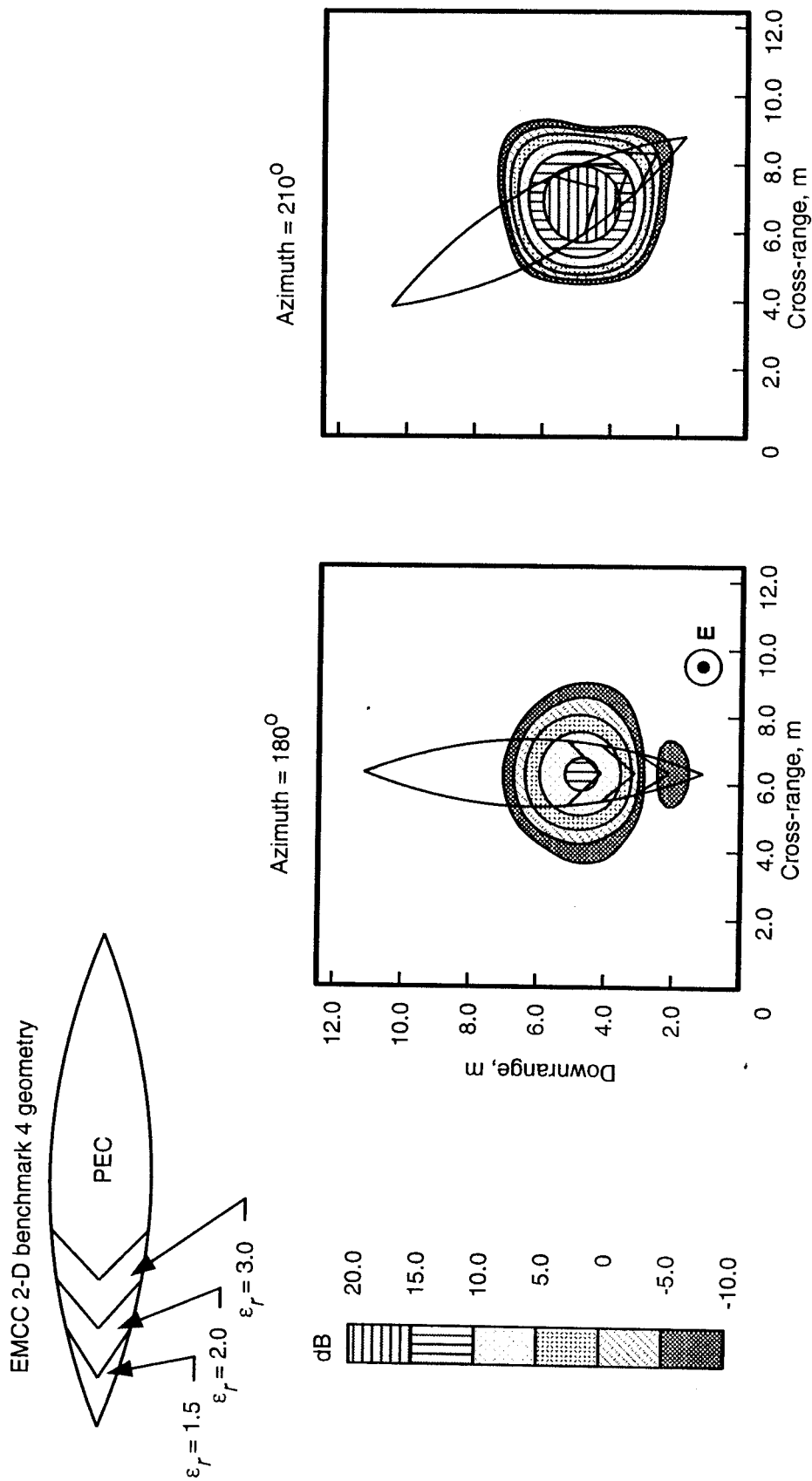


Figure 14. Concluded.



(a) EMCC benchmark 4 geometry description. Linear dimensions are in wavelengths.

Figure 15. Finite element frequency domain EMCC 2-D ogive benchmark 4 geometry and images. Frequency = 0.3 GHz.



(b) Images of EMCC benchmark 4. Vertical polarization and 1.5λ resolution.

Figure 15. Concluded.

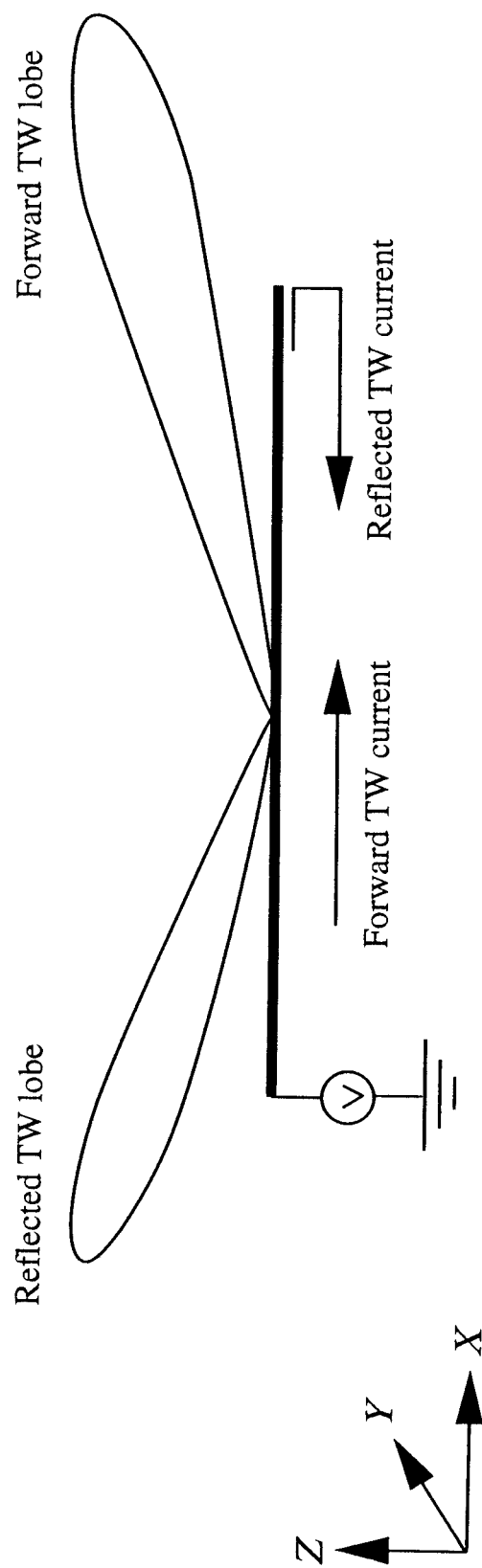


Figure 16. Five-wavelength end-fed traveling-wave antenna.

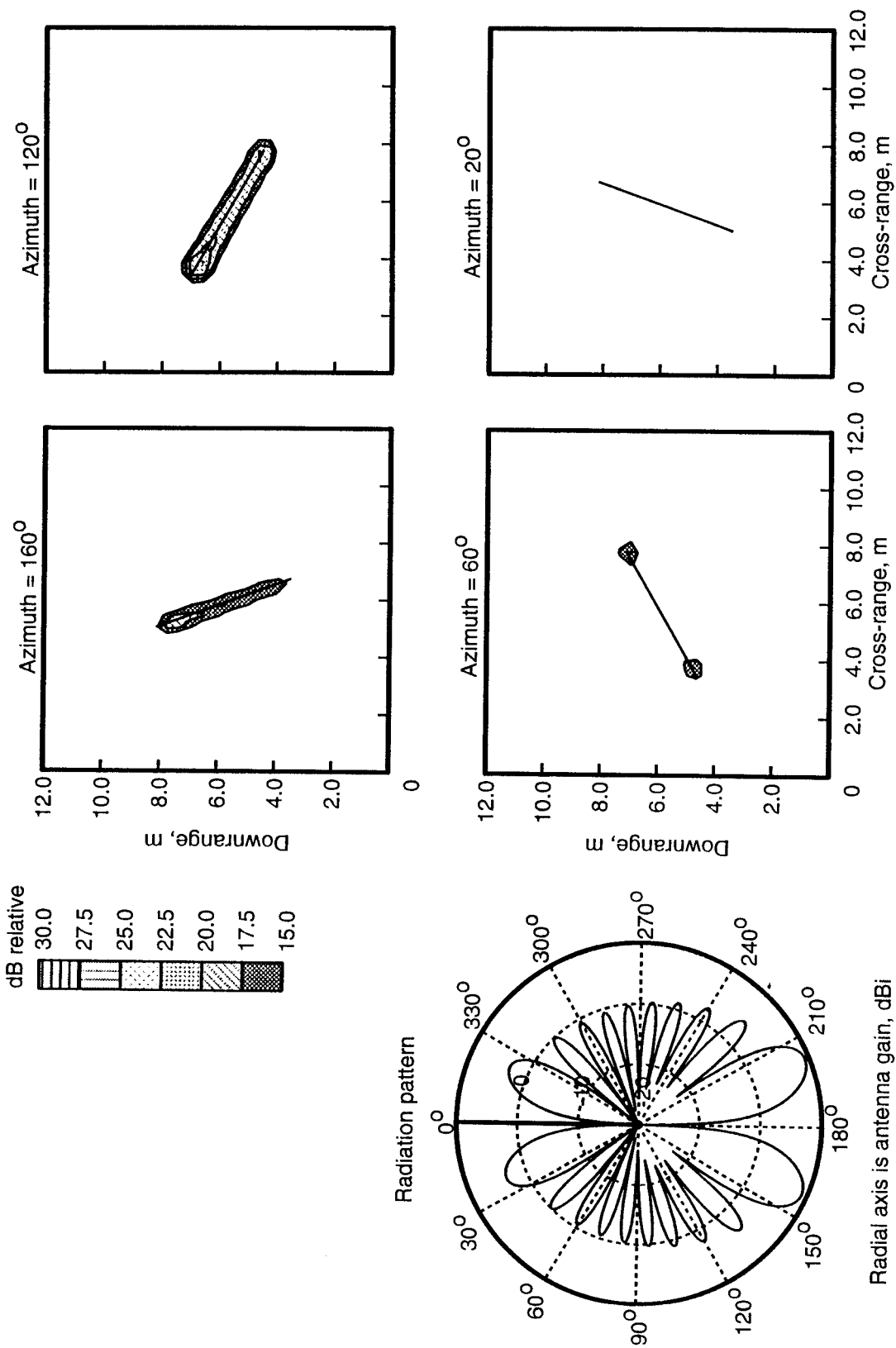
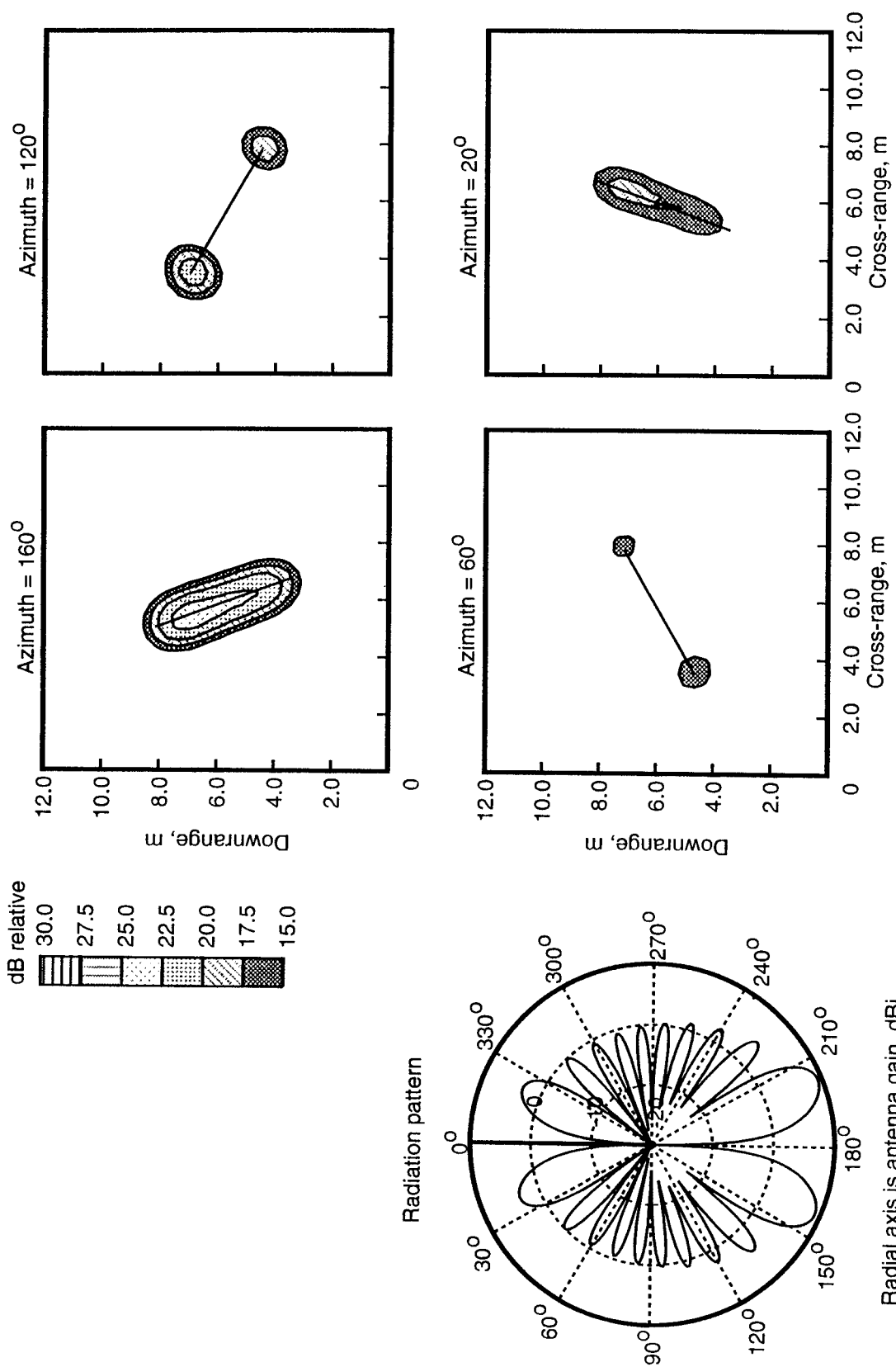
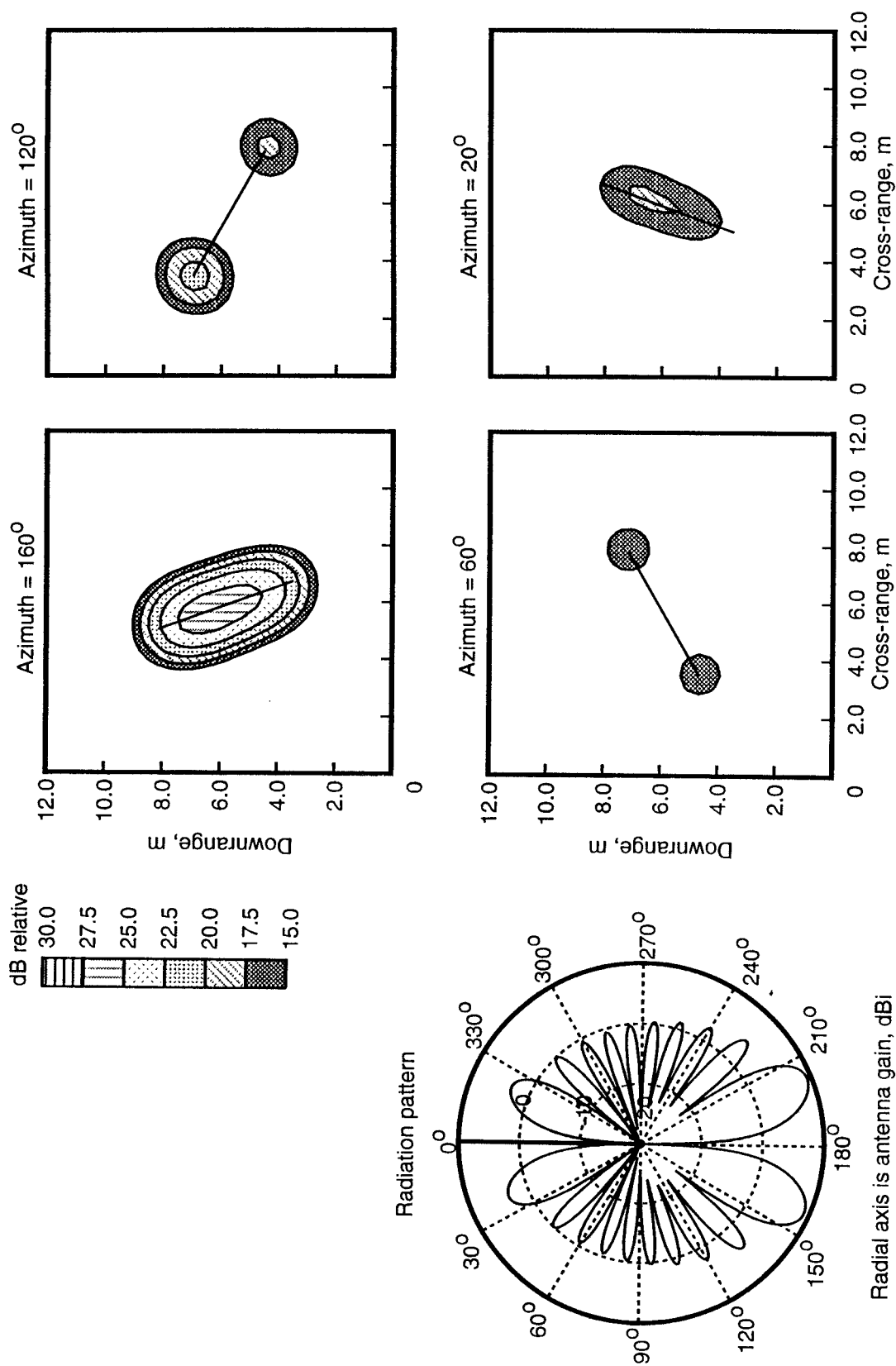
(a) 0.5λ resolution.

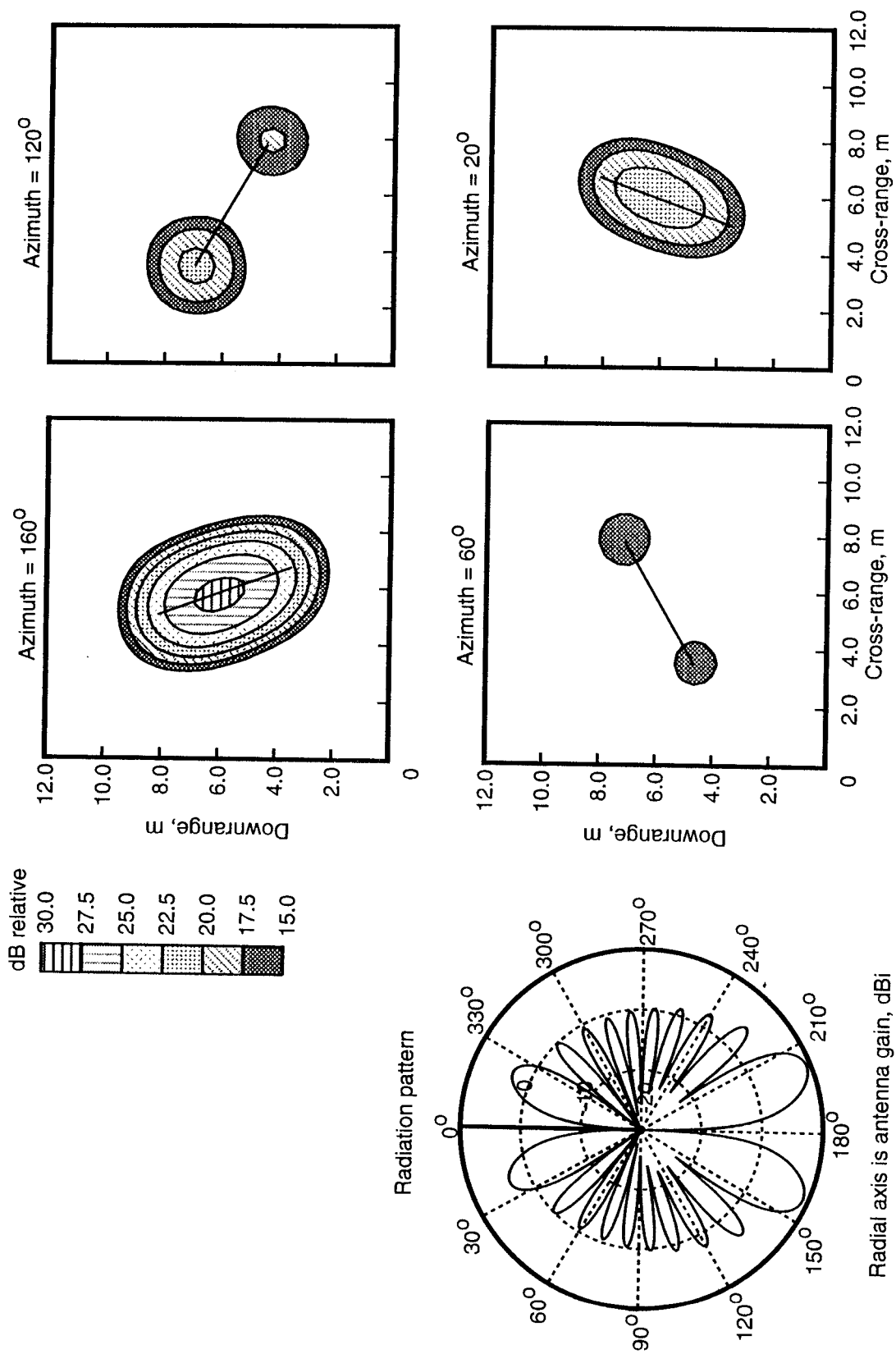
Figure 17. Five-wavelength antenna pattern and image results at various resolutions.



(b) 1.0λ resolution.

Figure 17. Continued.





(d) 2.0λ resolution.

Figure 17. Concluded.

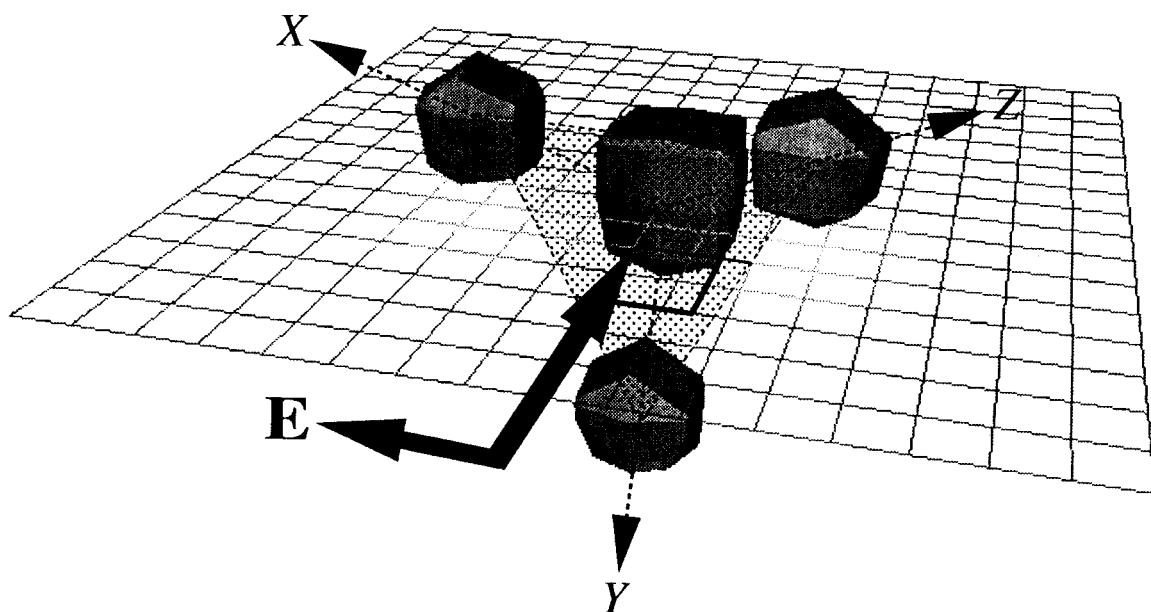


Figure 18. Three-dimensional image of four-point sources in space. Isosurface is -10 dB.

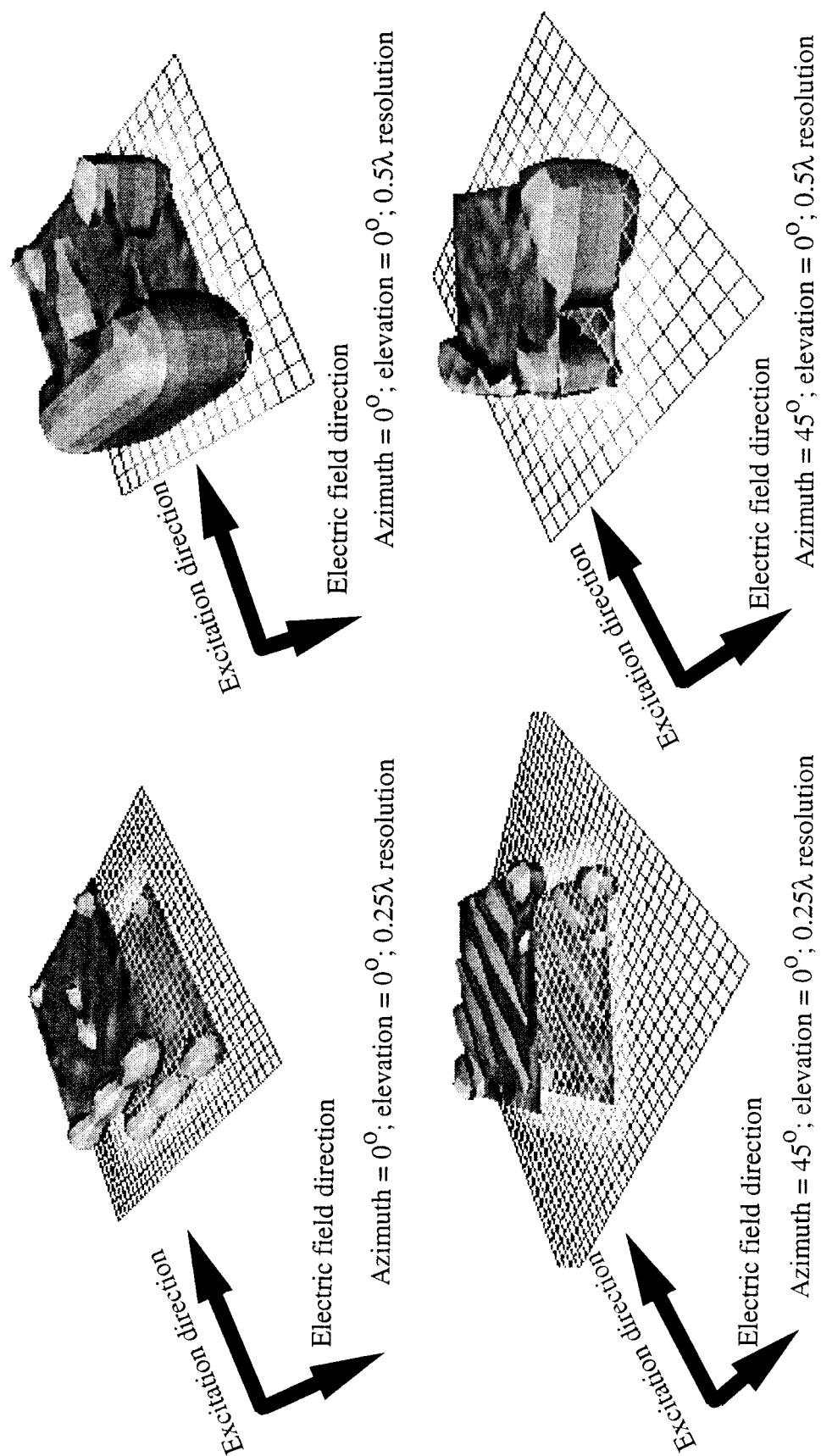


Figure 19. Three-dimensional images of two parallel 3λ -square plates. Horizontal polarization and isosurface of -15 dB.

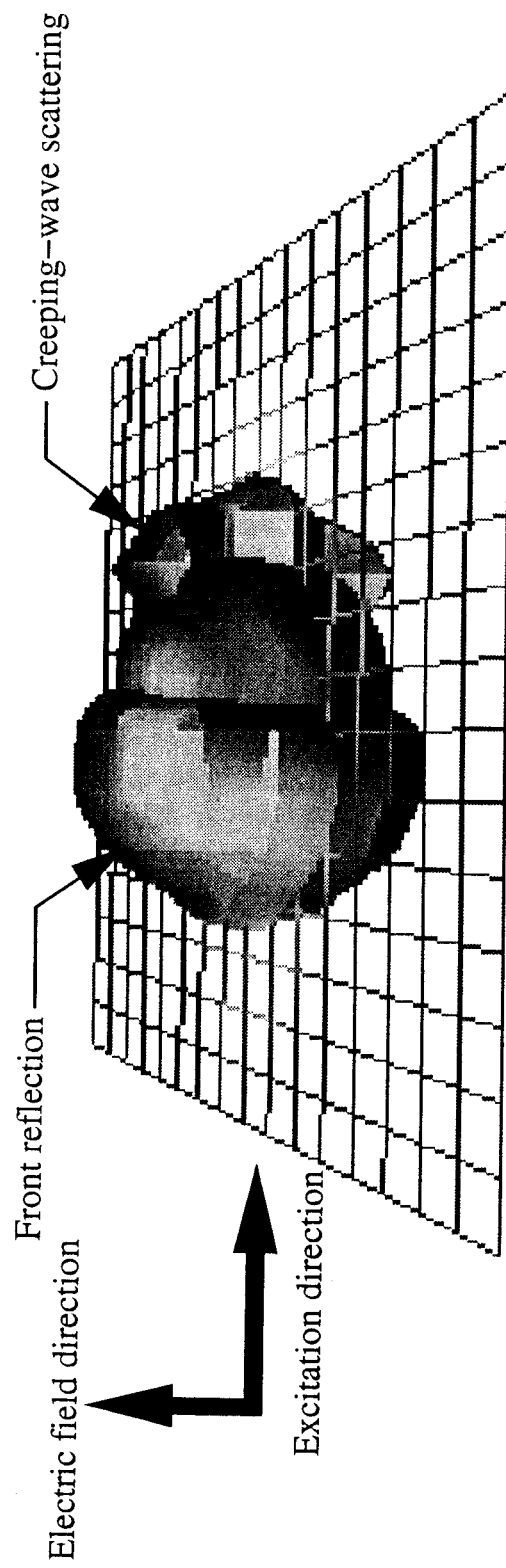


Figure 20. Three-dimensional image of sphere, $ka = 4$. Vertical polarization; 0.25λ resolution; isosurface of -30 dB; Azimuth $= 0^\circ$; and Elevation $= 0^\circ$.

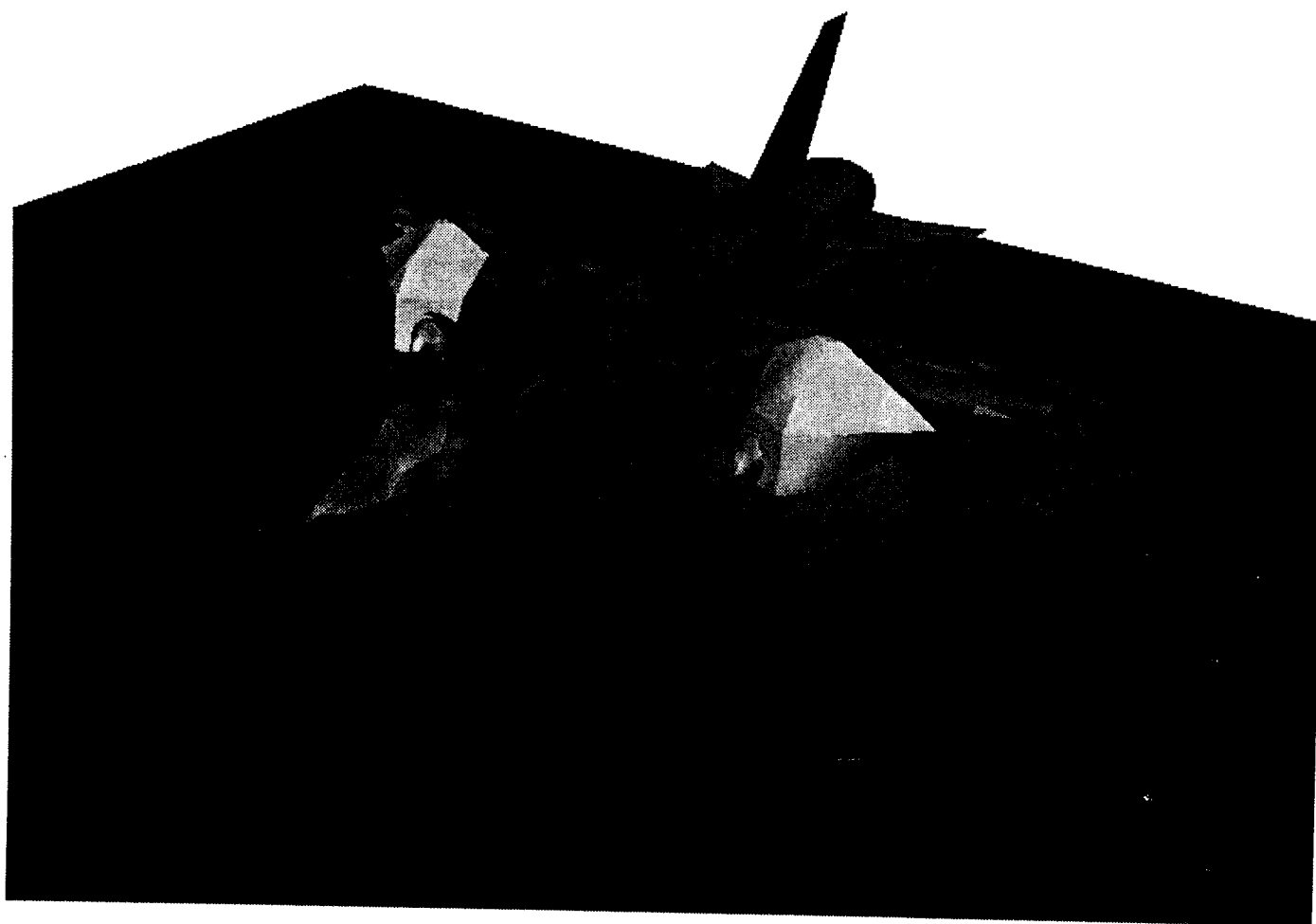


Figure 21. Airplane configuration MOM3D 3-D image. Horizontal polarization; center frequency = 6 GHz; nose-on incidence; 0.25λ image resolution and isosurface of -40 dB.

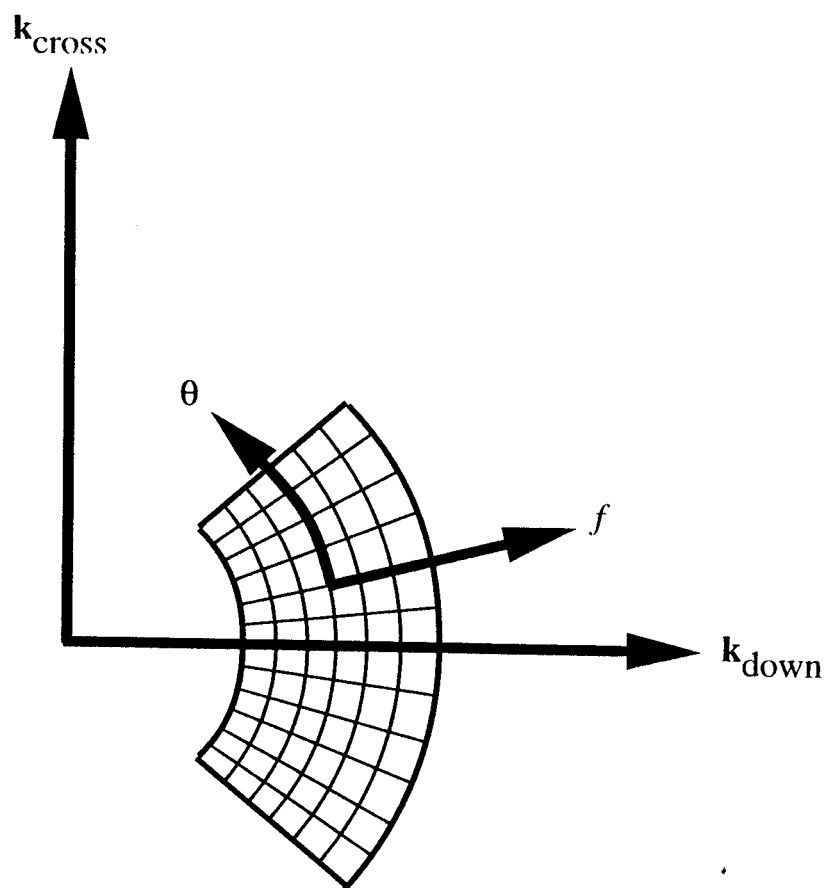
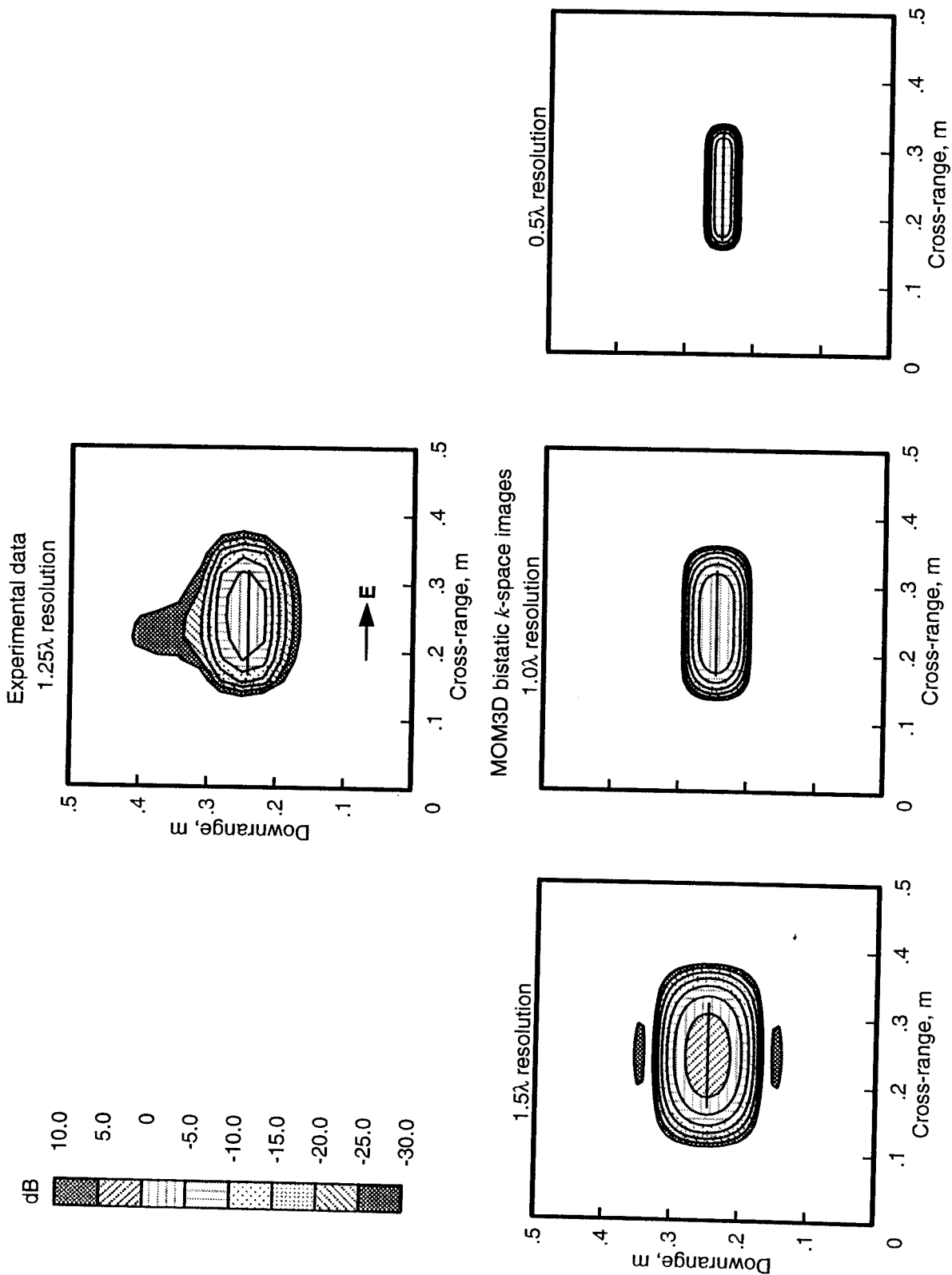
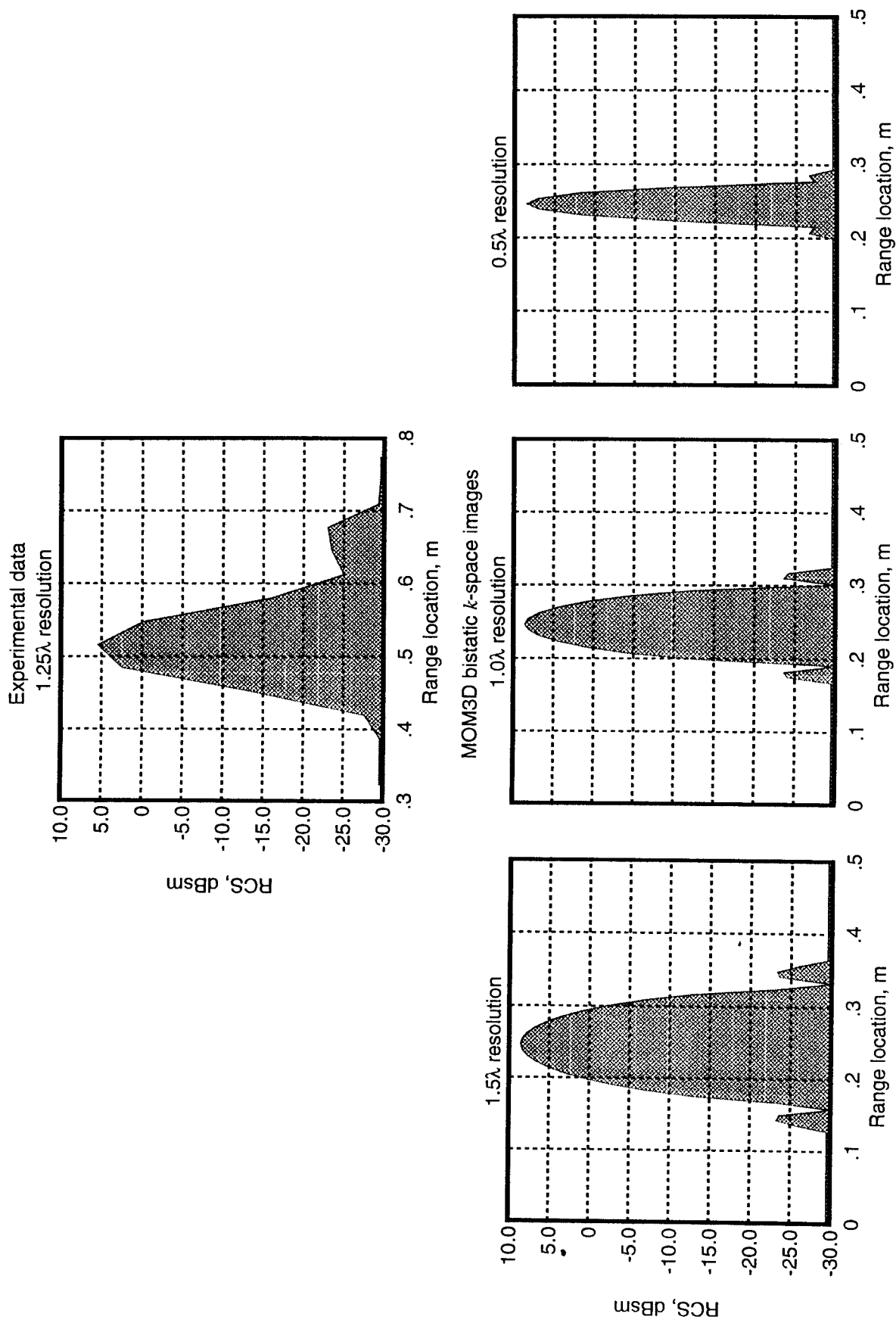


Figure 22. Experimental k -space measurement domain frequency and rotation angle.



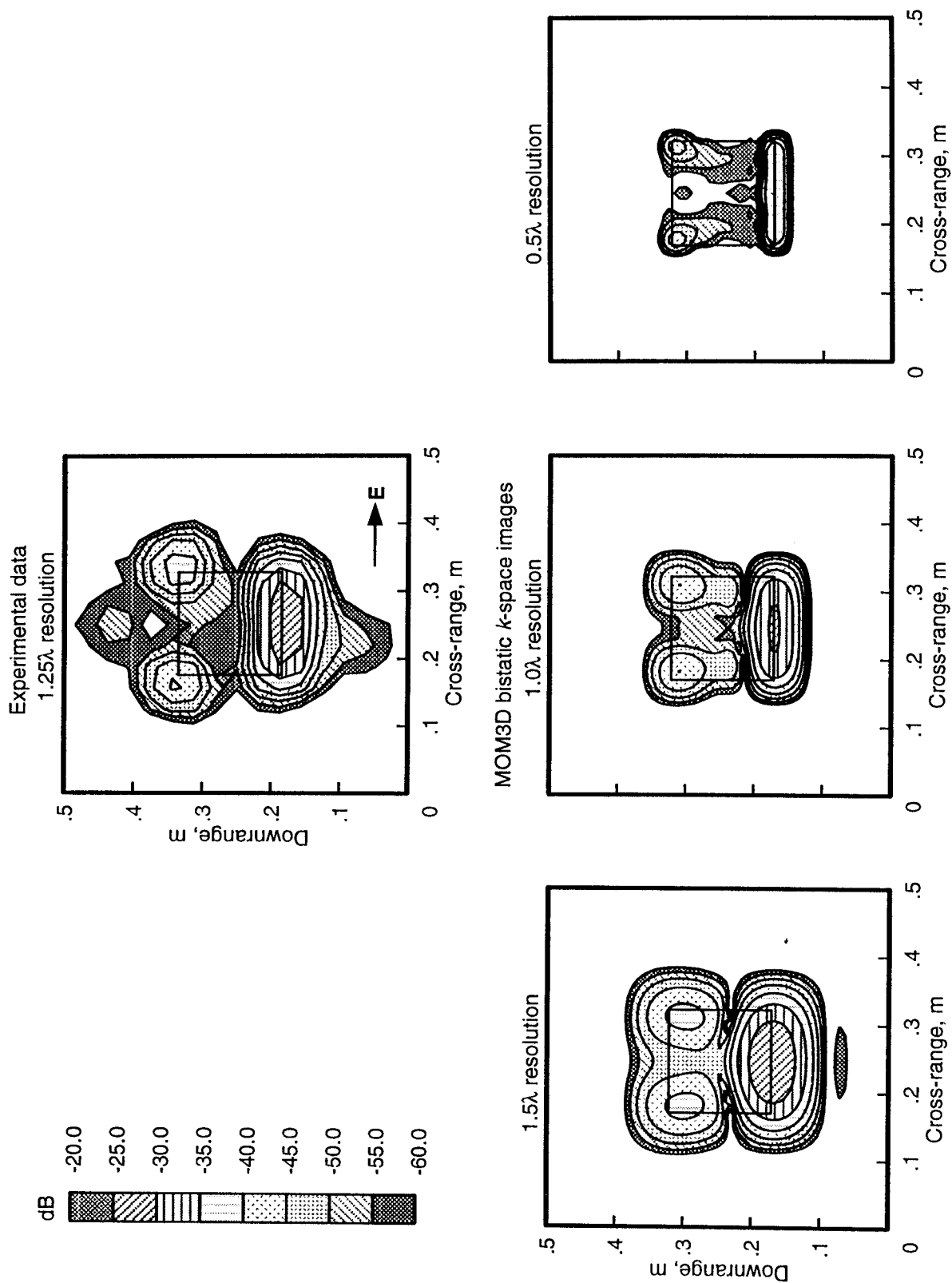
(a) Downrange-cross-range images.

Figure 23. View 1 experimental and bistatic k -space 2-D and 1-D image comparison. Horizontal polarization; Center frequency = 10 GHz; Azimuth = 0°; and Elevation = 90°.



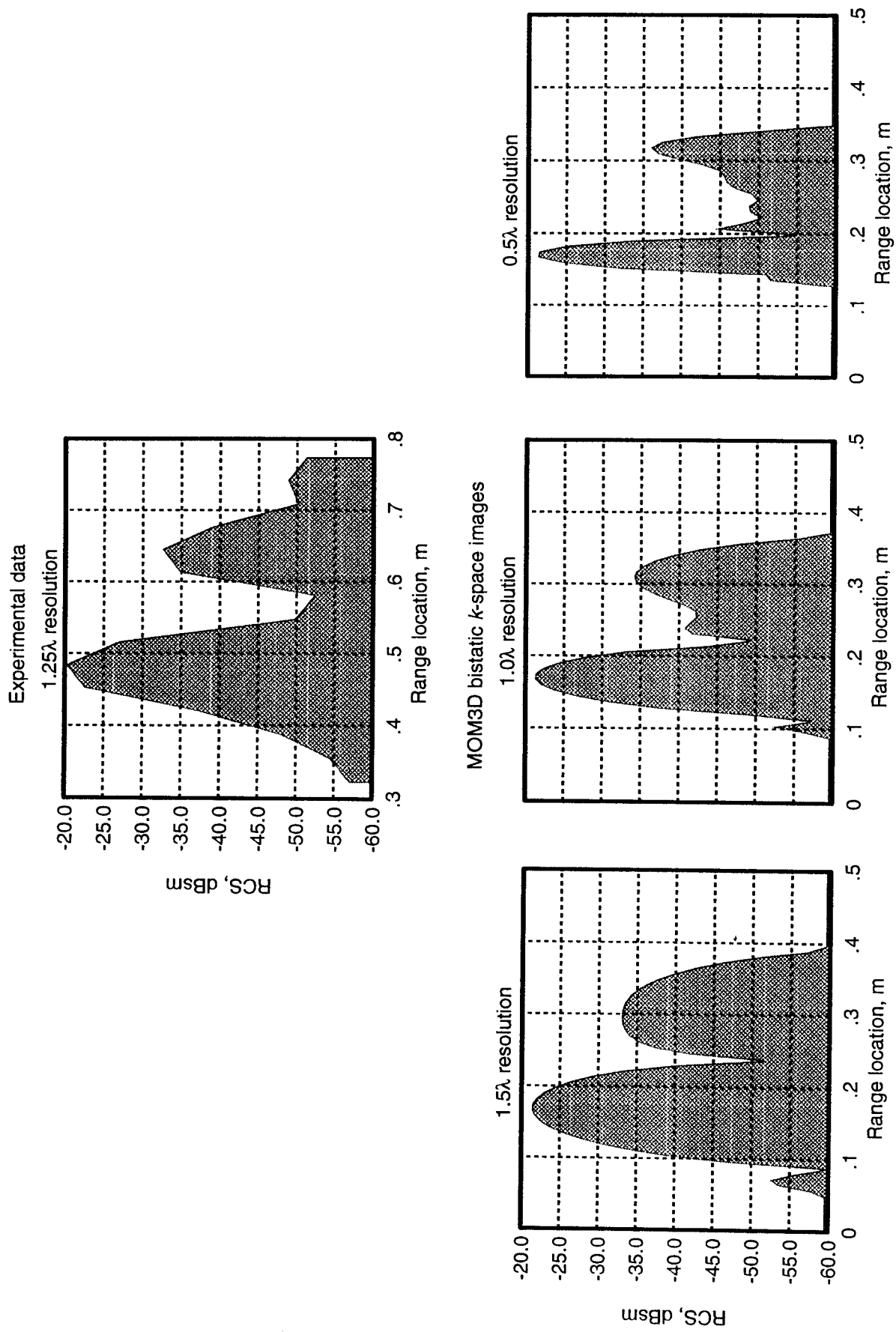
(b) Downrange images.

Figure 23. Concluded.



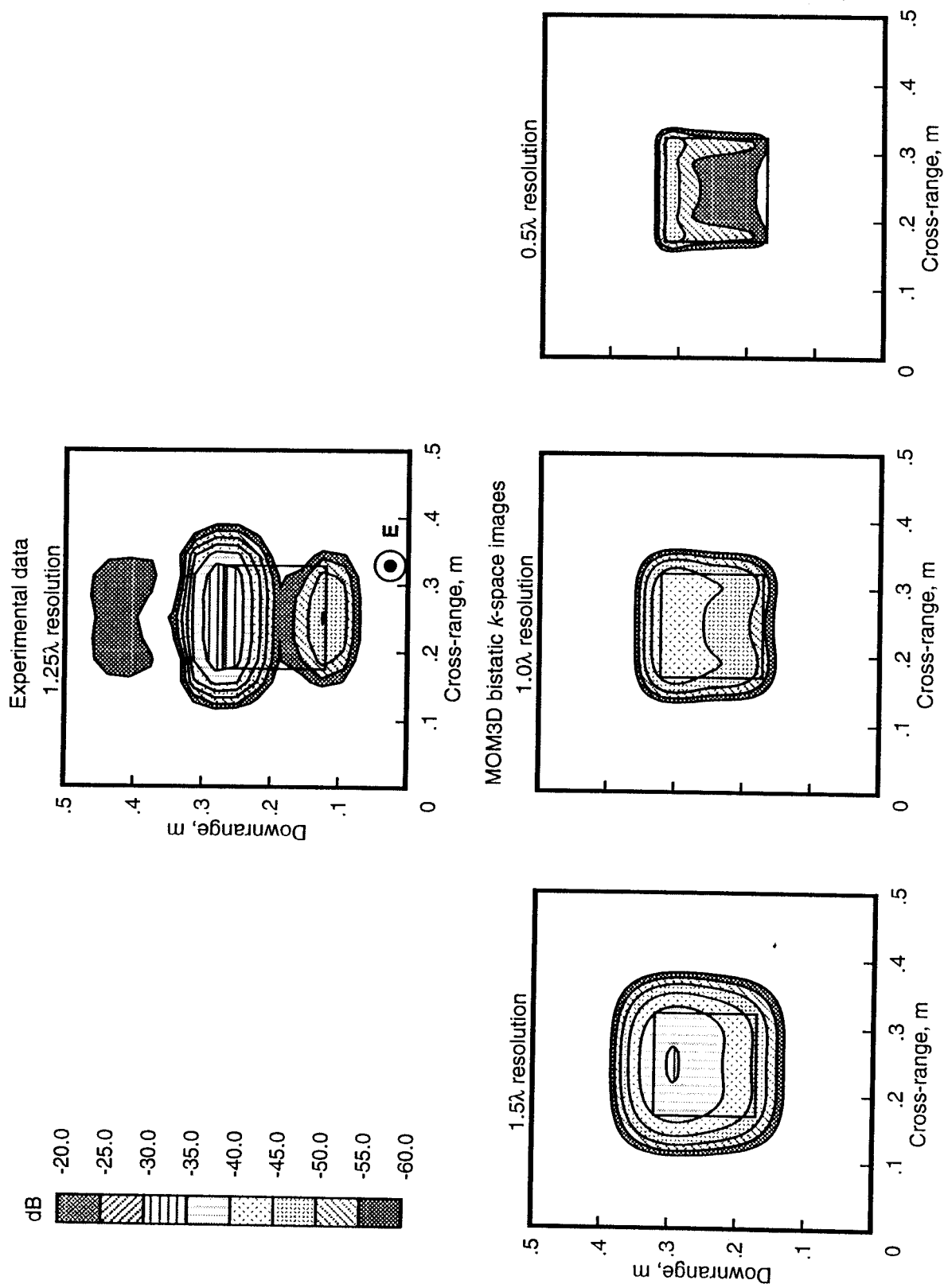
(a) Downrange-cross-range image.

Figure 24. View 2 experimental and bistatic k -space 2-D and 1-D image comparison. Horizontal polarization; Center frequency = 10 GHz; Azimuth = 0° ; and Elevation = 10° .



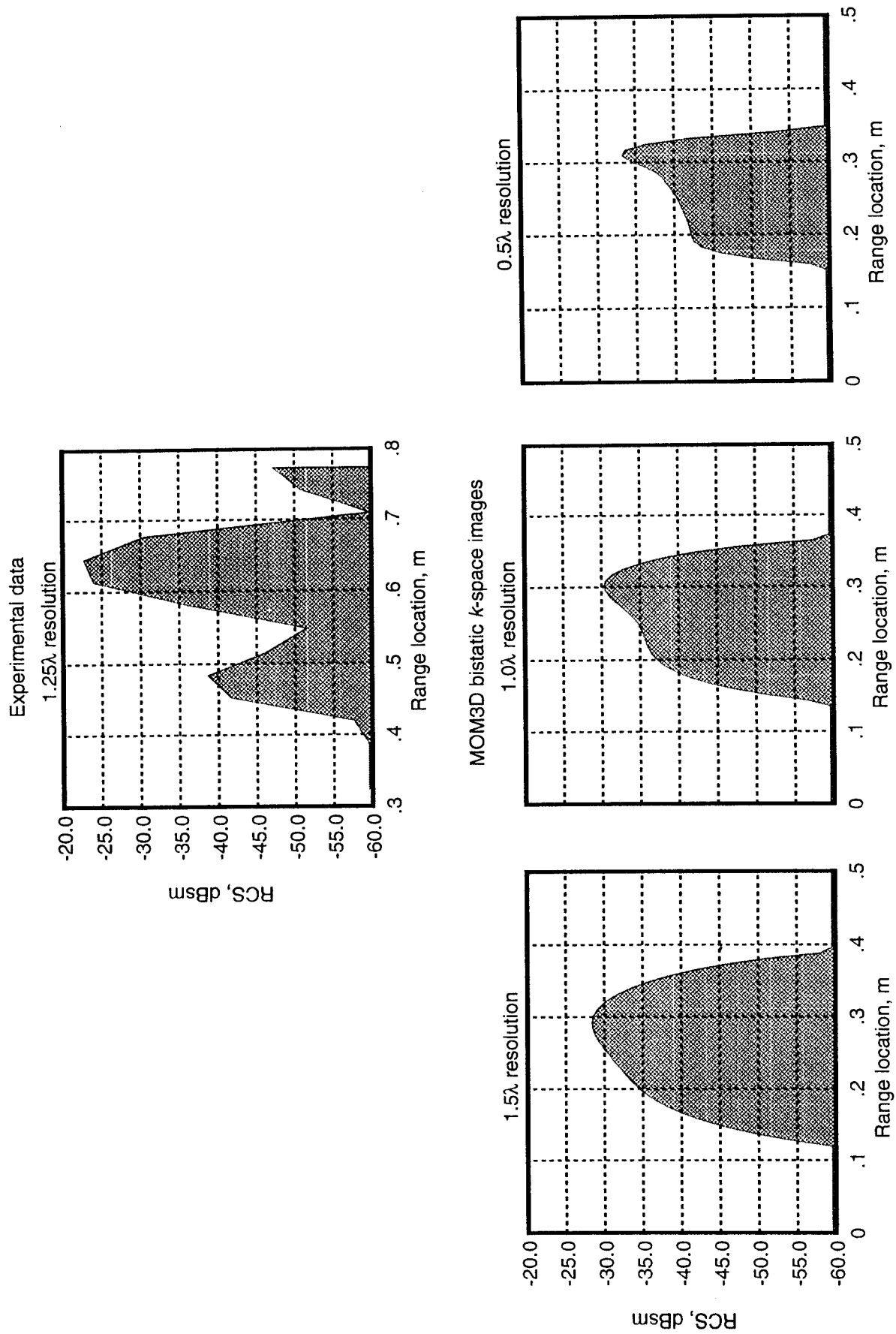
(b) Downrange images.

Figure 24. Concluded.



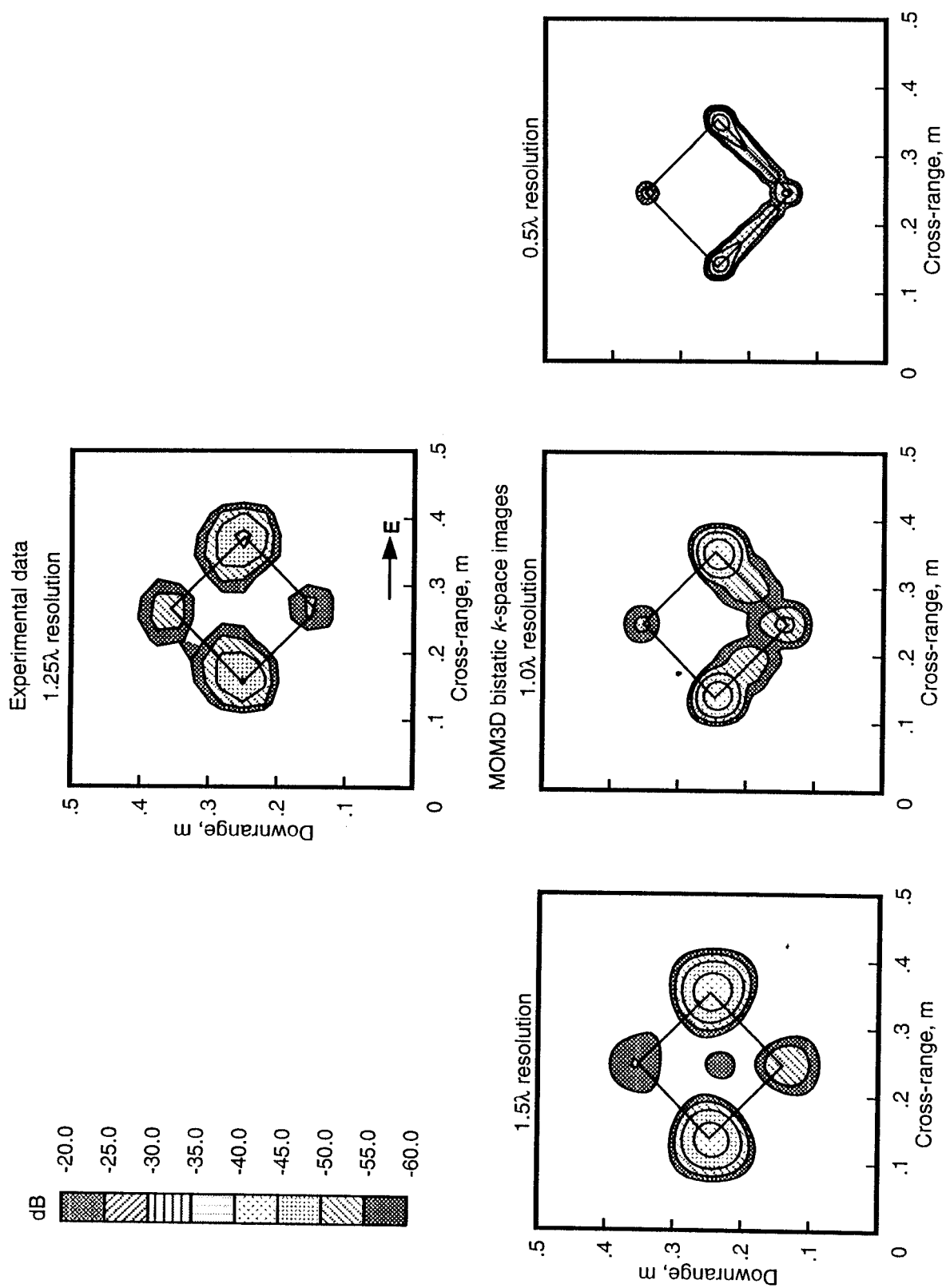
(a) Downrange-cross-range image.

Figure 25. View 2 experimental and bistatic k -space 2-D and 1-D image comparison. Vertical polarization; Center frequency = 10 GHz; Azimuth = 0° ; and Elevation = 10° .



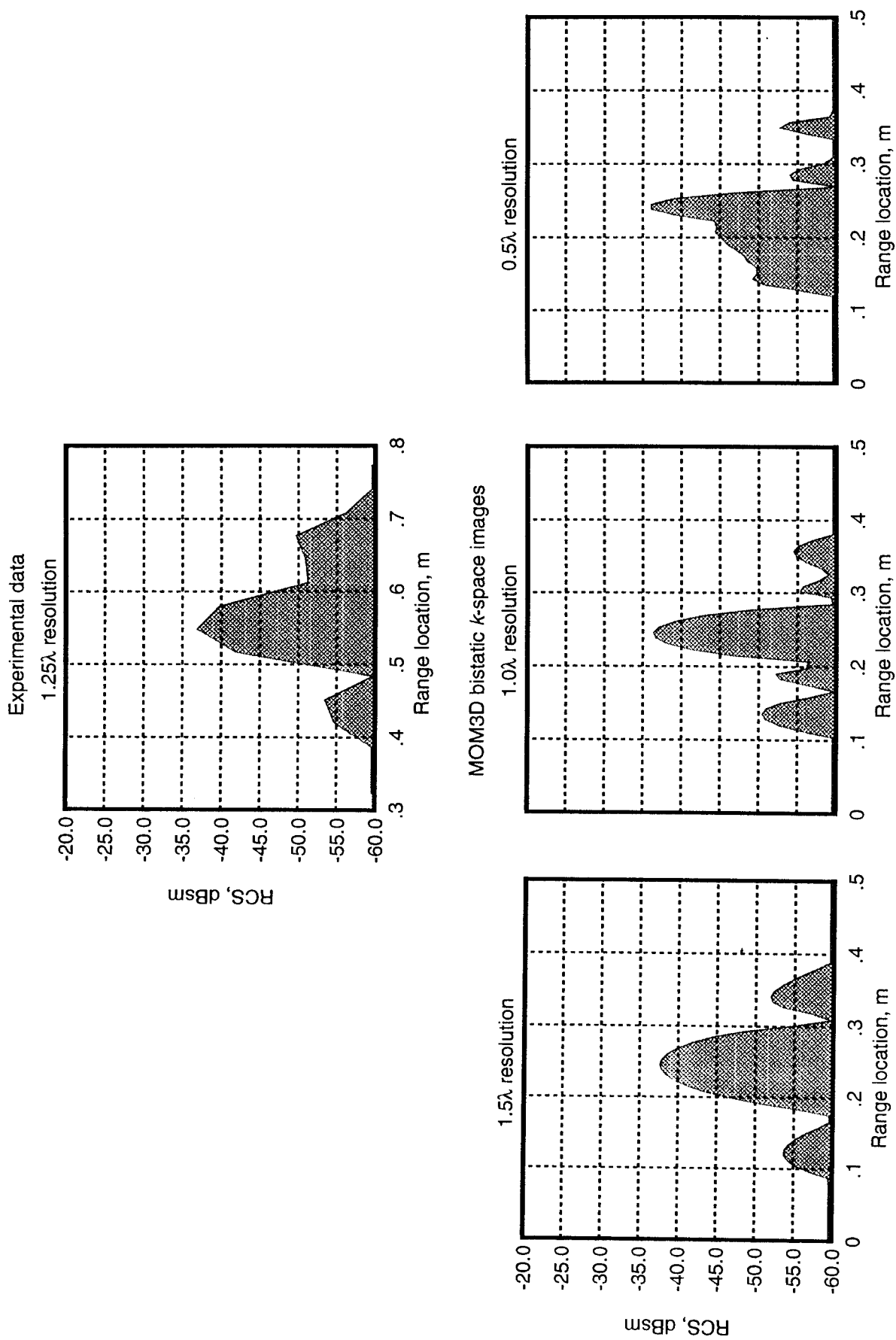
(b) Downrange images.

Figure 25. Concluded.



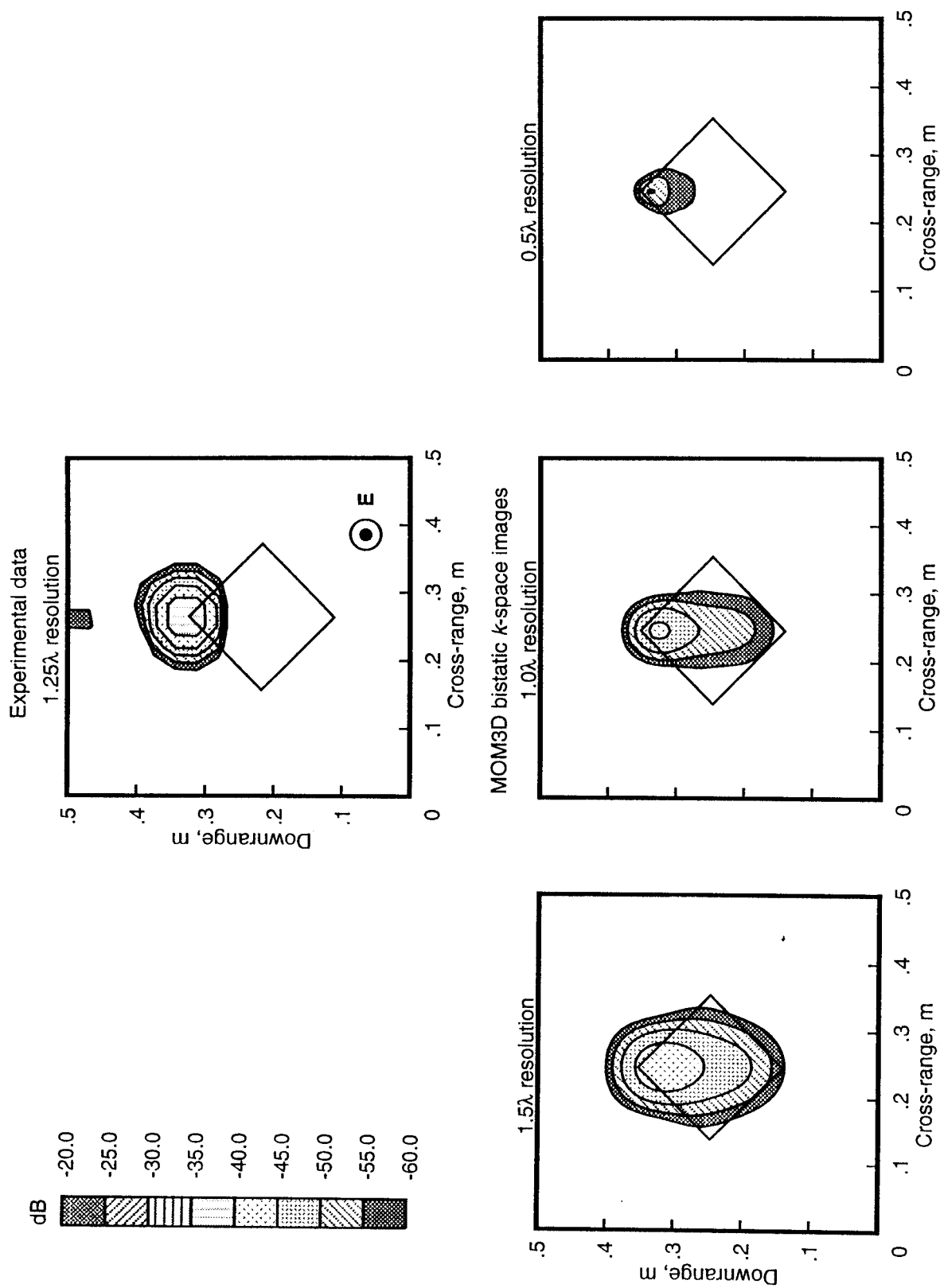
(a) Downrange-cross-range image.

Figure 26. View 3 experimental and bistatic k -space 2-D and 1-D image comparison. Horizontal polarization; Center frequency = 10 GHz; Azimuth = 45° ; and Elevation = 10° .



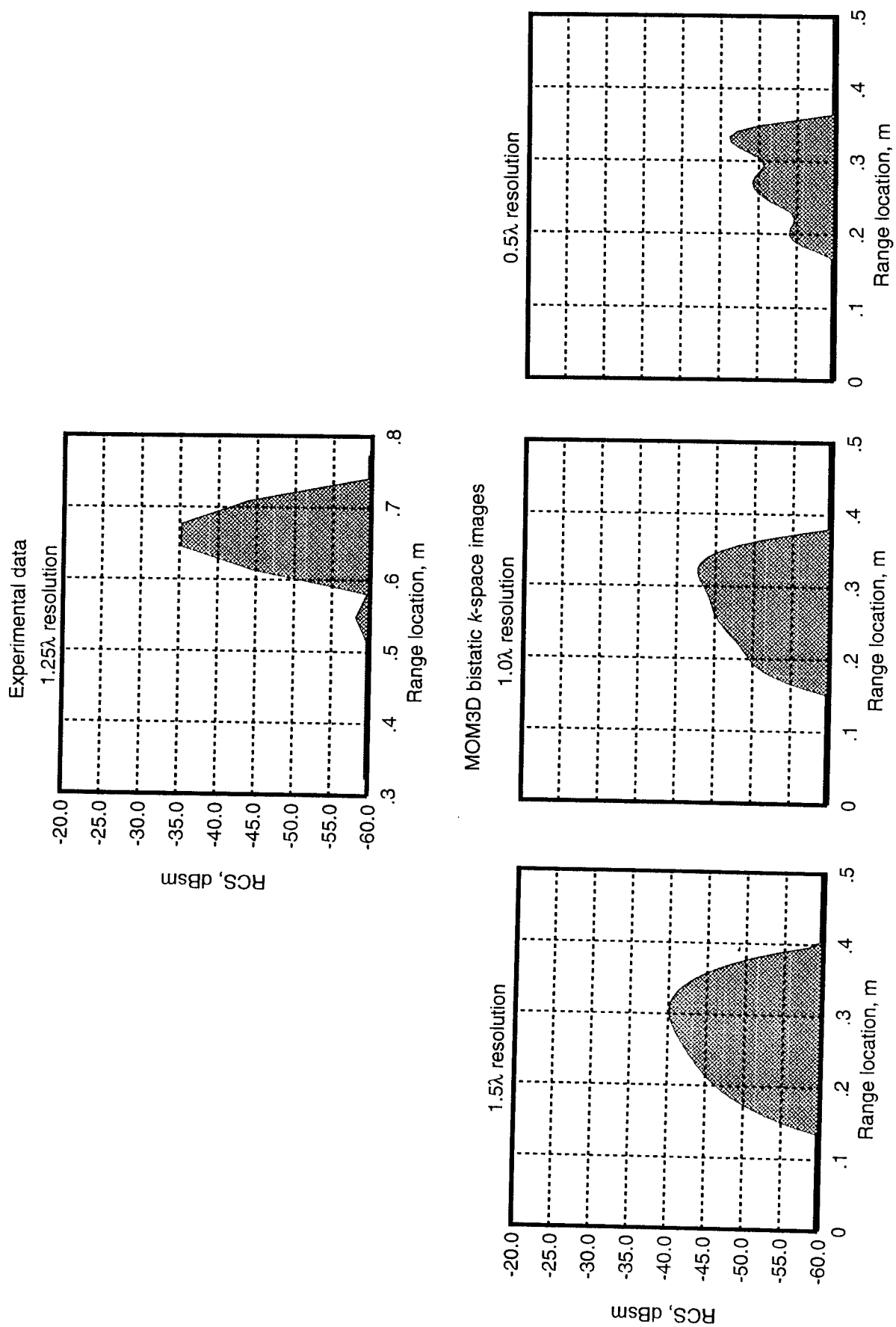
(b) Downrange images.

Figure 26. Concluded.



(a) Downrange-cross-range image.

Figure 27. View 3 experimental and bistatic k -space 2-D and 1-D image comparison. Vertical polarization; Center frequency = 10 GHz; Azimuth = 45°; and Elevation = 10°.



(b) Downrange images.

Figure 27. Concluded.